

Rational design of type-II nano-heterojunctions for nanoscale optoelectronics

Zhi Zheng ^{a,b}, Xiaotao Zu ^{a,**}, Yong Zhang ^c, Weilie Zhou ^{b,*}

^a School of Physics, University of Electronic Science and Technology of China, Sichuan, Chengdu, 610054, China

^b Advanced Materials Research Institute and Department of Physics, University of New Orleans, New Orleans, LA, 70148, United States

^c Department of Electrical and Computer Engineering and Optoelectronics Center, The University of North Carolina at Charlotte, Charlotte, NC, 28223, United States



ARTICLE INFO

Article history:

Received 30 July 2020

Received in revised form

11 August 2020

Accepted 11 August 2020

Available online 15 August 2020

Keywords:

Type-II heterojunction

Nanoscale

Optoelectronics

ABSTRACT

Over the last decades, great advances have been made in the development of nanoscale optoelectronics, such as solar cells, photodetectors, and light-emitting diodes. The design of heterojunctions with highly desirable interface properties and consequently controllable carrier transfer is of vital importance to construct high-performance optoelectronic devices. The type-II nano-heterojunctions, which facilitates the spatial separation of the electrons and holes, hold particular interests in developing high-performance optoelectronics. This review presents an overview of the material and structural design strategies, such as precise tuning of chemical composition and crystal structure, interface strain engineering, structural optimization, and external field stimulates, with the emphasis on the photophysical properties of type-II heterojunctions. Additionally, synthetic strategies for efficient material and structural modulation are also summarized. Lastly, several emergent optoelectronic applications based on the type-II heterojunctions, such as photonic memory, photonic synapses, and optical communication are discussed. We hope this review can provide comprehensive guidance for the future development of designing and realizing high-performance nanoscale optoelectronic devices based on type-II heterojunctions.

© 2020 Elsevier Ltd. All rights reserved.

1. Introduction

"The interface is the device", as Herbert Kroemer said in his Nobel Lecture, the semiconductor interface plays a crucial role in modern electronic and optoelectronic devices [1,2]. With the intensive research in the last few decades, it is now possible to achieve desirable electronic and optical properties of semiconductor materials by precisely tailoring their band structures, thus attain their key functionalities into specific applications. Compared to single-component semiconductors, of which the bandgap tailoring limited by their intrinsic properties, utilizing heterojunction in semiconductor devices allows nearly arbitrary and continuous bandgap variations to be made [3]. The rational design of the band structure of heterojunction allows us to precisely control the transport behavior of the charge carriers,

therefore, achieve unique properties for novel devices. In general, heterojunctions can be classified into type-I, type-II, and type-III heterojunctions, based on their distinct bandgap offsets (Fig. 1a) [1]. For the type-I heterojunctions, since the conduction band minimum (CBM) is higher and the valence band maximum (VBM) is lower than those in the other material, both the electrons and holes are tend to transfer to the right for the arrangement depicted in Fig. 1a. Therefore, type-I heterojunctions have been widely used in light-emitting devices such as LEDs and semiconductor lasers where the charge carrier recombination is required. For a typical type-II heterojunction, the bandgaps from two semiconductors form a staggered alignment, in other words, the energies of the conduction and valence bands of one semiconductor are relatively higher than the other semiconductor. Thus, following the initial generation of charge carriers under the external stimulus, the electrons and/or holes tend to transfer through the interface towards the opposite direction, resulting in the spatial separation of charge carriers and subsequent built-in electric field. Such charge confinement is of great importance in certain optoelectronic devices especially with light absorption or emission involved, such as

* Corresponding author.

** Corresponding author.

E-mail addresses: xtzu@uestc.edu.cn (X. Zu), wzhou@uno.edu (W. Zhou).

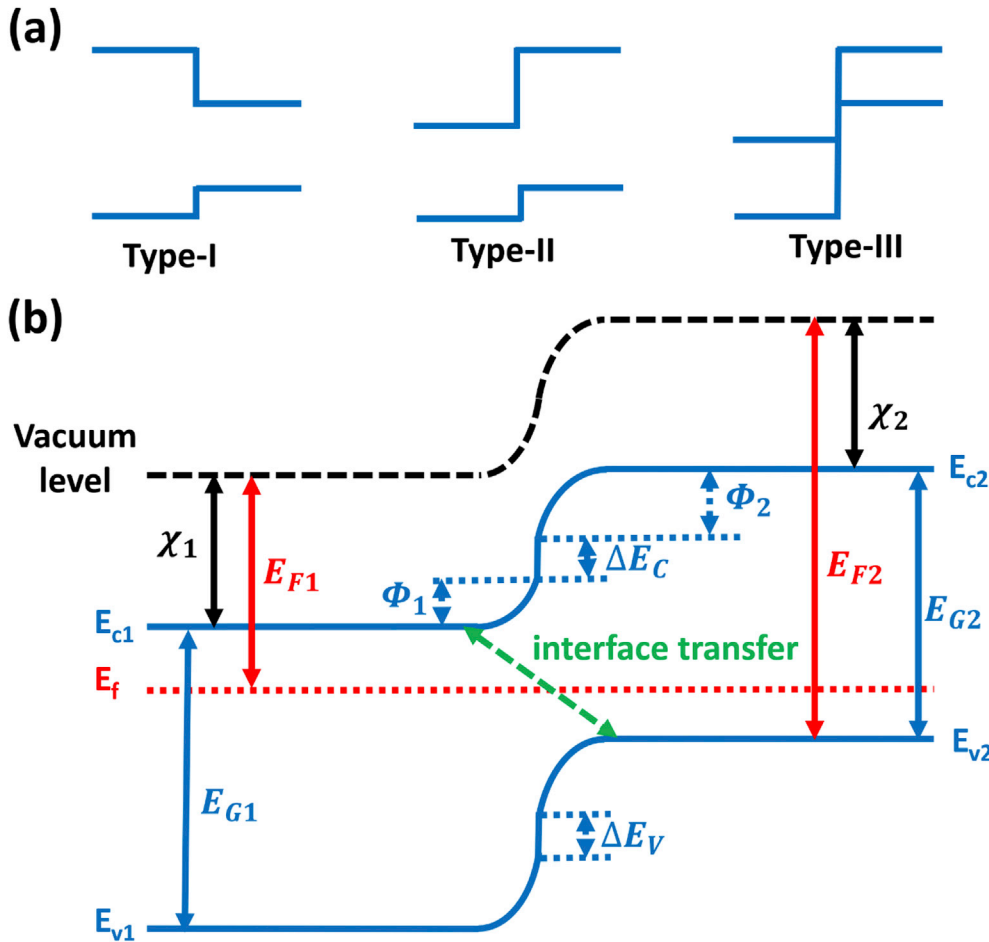


Fig. 1. a) Schematic energy band diagram of three types of semiconductor heterojunctions. b) Energy band diagram of a typical type-II heterojunction.

solar cells and photodetectors, since the efficient regulation of the carrier separation and transportation dominantly determines the performance of such devices [4]. In addition, the interfacial transition may extend the spectral range to a significantly longer wavelength than that defined by the bandgap of any of the components.

From the material's point of view, one major challenge for high-quality type-II heterojunction is the capability to forming an epitaxial interface between the adjacent semiconductor materials, meanwhile tuning the band structure of individual materials by varying the chemical composition in the nanoscale range. Thanks to the development of thin-film deposition technologies in the last century, varieties of growth methods, such as molecular beam epitaxy (MBE) and metal-organic vapor phase epitaxy (MOCVD), have been utilized in demonstrating novel heterojunction devices with intriguing properties, such as quantum wells and superlattices [5–7]. On the other hand, the remarkable advances of nanotechnology have made a profound impact in the areas of physics, chemistry, and materials science [8,9]. One main motivation in the development of nanoscale heterojunctions is to overcome the lattice-mismatch limitation that exists in conventional thin-film materials. The large tolerance to lattice mismatch in nanoscale permits the heterojunction forming from dissimilar materials, which substantially expanding the range of achievable energy bandgaps and provides new opportunities for both materials research and novel device applications [10]. Additionally, the semiconductor nanomaterials, whose physical and chemical

properties are often reliant on their size, morphology, crystal structure, and composition, have demonstrated remarkable advances in tailoring the band structures otherwise difficult or impossible for the bulk materials, thus providing powerful tools to achieve the desired electronic and optical properties for specific applications. Thus, tremendous efforts have been adopted in developing nanoscale type-II heterojunctions [11–13], which helped us to gain an in-depth understanding of the correlation of the structure and the novel properties in semiconductor nanomaterials, and ultimately, to achieve a more controllable synthesis and reliable device performance.

On the basis of type-II heterojunction principles, the novel properties were realized from the staggered alignment of the bandgap of adjacent semiconductors at the heterojunction. The rich variety of available combinations of the semiconductor nanomaterials with distinct intrinsic electric and optical properties, precise tuning of the chemical composition and crystal structure, interface strain engineering, structural optimization, and external field stimulates, have made the rational design of type-II nano-heterojunctions feasible to meet the specific requirements for various applications. In this regard, rational design strategies of the type-II nano-heterojunctions are of vital importance to achieving the desired characteristics for various optoelectronic applications. So far, there have been many reviews focused on the nano-heterojunctions, from their synthesis to the applications but few specified on the type-II heterojunctions [14–19]. In this review, on the other hand, we aim to present a comprehensive review of the

designing principles specifically for type-II nano-heterojunctions. The overview of the material and structural design strategies, such as precise tuning of chemical composition and crystal structure, interface strain engineering, structural optimization, and external field stimulates, with the emphasis on the photophysical properties of type-II heterojunctions are presented. Additionally, synthetic strategies for efficient material and structural modulation are also summarized. Several emergent optoelectronic applications based on the type-II heterojunctions, such as photonic memory, photonic synapses, and optical communication are discussed as well. Finally, we highlight the current issues and opportunities in type-II nano-heterojunctions for optoelectronic applications.

2. Rational design strategies

Similar to that of the homojunction, the band alignment of heterojunction under thermal equilibrium is ultimately determined by the band offsets. Fig. 1b shows the band diagram of a typical type-II heterojunction. After the junction reaches the thermal equilibrium, the build-in potential implies the band structures and results in the band bending. However, it should be keeping in mind that both the conduction band and valence band are in the fixed position related to the vacuum level. For the homojunction, it is a relatively simpler scenario since both sides of the interface are the same materials, therefore, their conduction band and valence band are at the same levels, respectively. In this case, even after band bending, the band levels are still continuous. On the other hand, for the heterojunction, most often the two materials would have different band levels for either conduction band or valence band, thus resulting in the discontinuity of the band levels after the band bending. Given by Anderson's rule, the discontinuity of the conduction band can be given by the difference in electron affinity:

$$\Delta E_C = \chi_1 - \chi_2$$

and the discontinuity of the valence band can be given by:

$$\Delta E_V = (\chi_1 + E_{G1}) - (\chi_2 + E_{G2})$$

where $\chi_{1,2}$ and $E_{G1,2}$ are the electron affinity and bandgap for the semiconductors, respectively.

Another important feature of the band structure in the heterojunction is the build-in potential, which was determined by the interface position of the Fermi levels E_{F1} and E_{F2} . As we mentioned before, the band bending resulted from the build-in potential on both sides of the interface to the extent that the Fermi levels in two semiconductors eventually line up to be constant and flat. Therefore, the barriers due to the build-in potential can be given by:

$$\Phi_{bi} = \Phi_1 + \Phi_2 = E_{F1} - E_{F2}$$

There are several signatures of a type-II heterojunctions, including: (1) a photoluminescence (PL) peak at the expected interfacial transition energy that should be below the lower bandgap of the two components; (2) optical absorption occurring in the spectral region of the anticipated interfacial transition, which is expected to extend into the longer wavelength than the threshold determined by the bandgap of the lower bandgap component; (3) a long carrier time or slow decay of the type II emission; and (4) photo-response (i.e. photo-current) associated with the type II transition. In which signatures (2) and (3) are considered as reliable measures to distinguish the type-II interlayer exciton and defect-related exciton. For signature (2), the defects are less likely to have any measurable absorption strength, unless with a very high density. For signature (3), because a defect state in the bulk part of the material rarely has a long lifetime, the presence of

defects in the bulk part tends to shorten the carrier lifetime. Therefore, the observation of a long carrier lifetime could be viewed as an indication of good quality of the material involved.

The concept of utilizing type-II heterojunction in optoelectronics devices can be traced back to the early 80s in the last century [20]. The basic idea that type-II heterojunction was proposed is that the electrons and holes, after they have been initially generated, tend to be confined in the opposite side of the interface based on their diverse lowest energy states, resulting in the spatial separation of electrons and holes. On the other hand, such configuration provides a "hidden" interface bandgap, which is smaller than that of either the constituent semiconductors forming the heterojunction [4]. Therefore, it reduced the transition energy required for electron/hole generation and recombination, allowing extending the wavelength range that would otherwise not be available, thus has important implications in optoelectronics applications. The performance of the type-II nano-heterojunctions largely relies on intrinsic properties of the semiconductor materials such as chemical composition and crystal structure, interface characteristics such as band alignment and strain, as well as external stimulates. Therefore, many strategies have been developed to precisely tailor the electronic and optoelectronic properties of type-II nano-heterojunctions oriented by the specific requirement for various devices.

2.1. Band alignment

The band alignment at the interface plays a vital role in determining the charge carrier transfer properties of the type-II heterojunctions and thus their optoelectronic performance. Designing the favorable band alignment is of great importance to facilitate the charge carrier separation extraction for solar cells and photodetectors [21]. The engineering of band alignment is usually relying on the intrinsic tuning of the composition of one or both of the semiconductor materials forming the interface. For example, Siol et al. systematically investigated the large variety of energy band alignment of $\text{Cu}_2\text{O}/\text{ZnO}$ heterojunctions prepared by various deposition techniques and parameters [22]. The variation is directly related to the concentrations of metallic precipitates of Cu_2O or oxygen vacancies for ZnO resulted from different chemical compositions. As a result, the valence band offsets in the range 1.45–2.7 eV can be controlled. Pan and co-workers reported the successful synthesis of a series of $\text{WS}_2/\text{WS}_{2(1-x)}\text{Se}_{2x}$ ($0 < x \leq 1$) monolayer lateral heterojunctions by a one-step chemical vapor deposition method [23]. The well-controlled chemical composition from WS_2 to WSe_2 gave rise to a tunable band structure of the shell while keeping it constant of the core, and thus a tunable band alignment of the heterojunction. As shown in Fig. 2a, the PL peak corresponding to $\text{WS}_{2(1-x)}\text{Se}_{2x}$ shifts towards lower energy as the x increases, indicating a decrease of the bandgap. On the other hand, the PL peaks and the bandgaps of the WS_2 remain constant. In addition, the Fermi-level variation in the $\text{WS}_2/\text{WS}_{2(1-x)}\text{Se}_{2x}$ and the band alignment engineering were confirmed by the gradual increase of the surface potential difference confirmed using Kelvin Force Probe Microscopy. Later, the same group studied the wavelength-tunable interlayer exciton emission in $\text{WS}_2/\text{WS}_{2(1-x)}\text{Se}_{2x}$ lateral heterojunctions [24]. Similarly, a serial of $\text{WS}_{2(1-x)}\text{Se}_{2x}$ with continuously changed composition were synthesized and used to form the van der Waals heterojunctions with a fixed composition WS_2 layer. In turn, a very wide tunable bandgap range of 1.97–1.40 eV with a wavelength-tunable interlayer exciton emission range of 1.52–1.40 eV in the near-infrared region was achieved.

Other strategies have been developed to optimize the band alignment as well. For instance, Wick-Joliat et al. developed a dipole

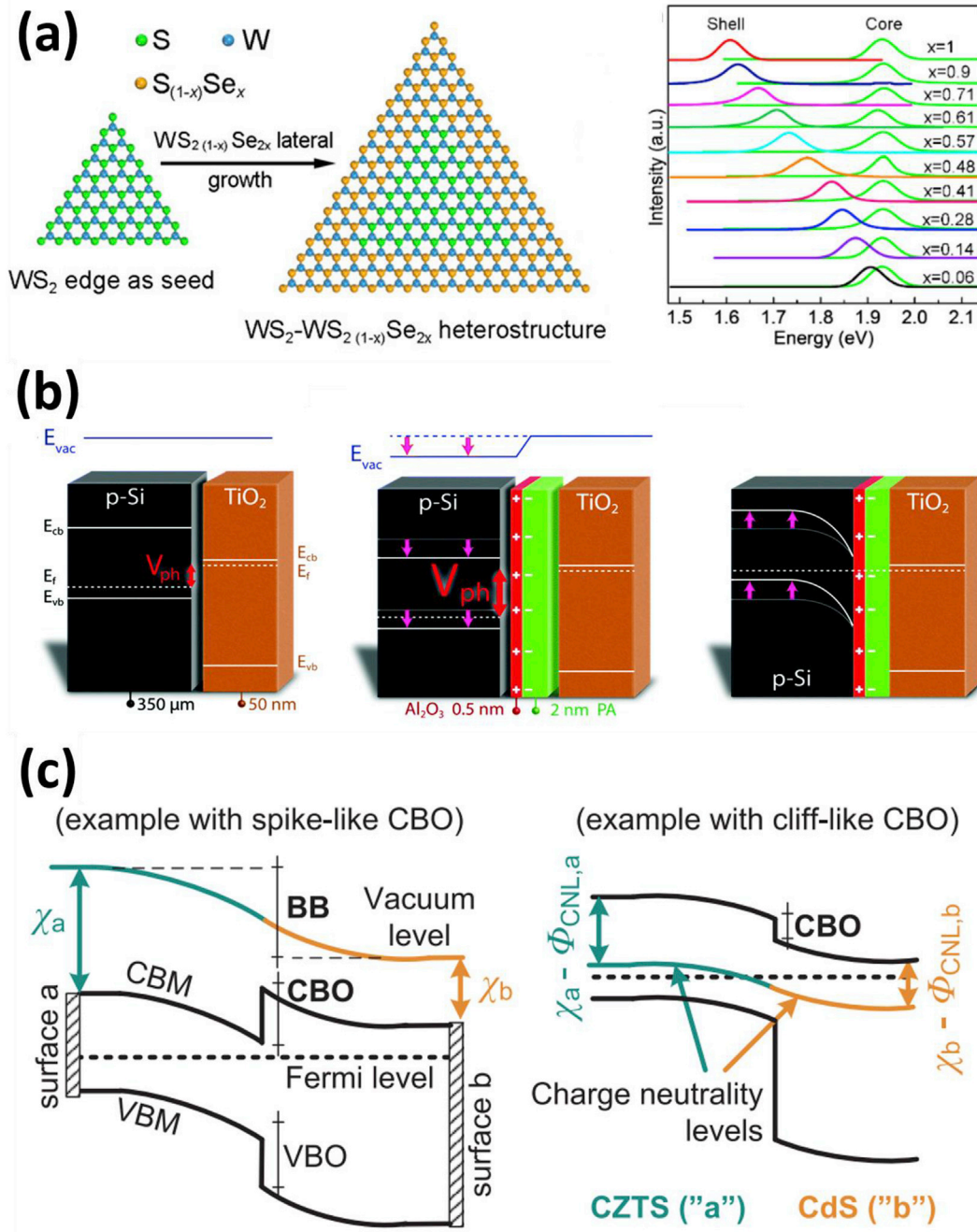


Fig. 2. a) Schematic illustration and PL spectra of $\text{WS}_2/\text{WS}_{2(1-x)}\text{Se}_{2x}$ heterojunctions. Reproduced with permission [23]. Copyright © 2018 American Chemical Society. b) From left to right, band diagrams of p-Si/n-TiO₂, p-Si/anchor layer/PA/n-TiO₂ in flat band condition, and in equilibrium, indicating an increased band bending represented by a step in the vacuum energy level. Reproduced with permission [25]. Copyright © 2019 The Royal Society of Chemistry. c) Band diagrams of spike-like and cliff-like CBO. Reproduced with permission [27]. Copyright © 2017 Elsevier B.V.

strategy in aim to control the band bending at the interface [25]. In their study, the phosphonic acid (PA) inserted between p-Si and n-TiO₂ heterojunction creates a dipole layer, which can be represented by a step in the vacuum energy level, leading to the shift of the band edge and increased band bending (Fig. 2b). As a result, the optimized band alignment demonstrated great improvement for both photovoltaic device and photoelectrochemical cell, as the J-V curves shifted to higher potential by 200 mV, indicating increased open-circuit voltage, higher fill factor, and enhanced power conversion efficiency by more than 100%. The dipole effect is formed at

the anchor layer metal oxide/PA interface by replacing the natural hydroxyl groups surface termination by phosphonate groups with different electron donating/withdrawing behavior and the band shift in a range of 0–400 mV can be fine-tuned by controlling the thickness of the PA layer.

The discontinuity of the band levels together with the barriers due to the build-in potential, define the fine structures of the heterojunction band diagram and determine the carrier transportation in the heterojunction devices. In contrary to that of homojunction, the band alignment of heterojunction may cause some spikes and/

or notches at the interface and acting as barriers or trapping sites for carrier transfer. Those unique features may possess great influence in the performance of optoelectronic devices. Taking solar cells as the example, $\text{Cu}_2\text{ZnSnS}_4$ (CZTS) was considered as a p-type semiconductor with suitable properties for solar cell applications owing to its ideal direct bandgap, high absorption coefficient, and earth-abundance [26]. CZTS is usually paired with an n-type window layer to form a heterojunction solar cell. The major issue for CZTS-based solar cells lies on the low open-circuit voltage (V_{oc}). One possible reason is the undesirable band alignment, mainly the conduction band offset (CBO) [27]. Different values of CBO have been reported and can be classified as spike-like or cliff-like, as shown in Fig. 2c. The cliff acts as a barrier for the electrons flowing from the window layer to the absorber layer under the forward bias and increases the interface recombination. On the other hand, if the spike is too large, the photogenerated electrons will be blocked by the interface barrier. Therefore, the optimal band alignment was reported to be spike-like with the CBO of 0–0.4 eV [28]. To construct the favorable band alignment, Sun et al. reported a novel $\text{Zn}_{1-x}\text{Cd}_x\text{S}$ buffer material with tunable band gaps for CZTS solar cells. A series of $\text{Zn}_{1-x}\text{Cd}_x\text{S}$ with variable composition and bandgap were obtained. It is found that $\text{Zn}_{0.35}\text{Cd}_{0.65}\text{S}$ with a bandgap of 2.7 eV creates the desired band alignment of the CBO of 0.37 eV with CZTS, and thus exhibits excellent performance with the efficiency of over 9% and the V_{oc} of 762 mV. The same strategy was also applied to improve the performance of photodetectors. Liu et al. studied the photodetection performance of $\text{CuI}/\text{n-Si}$ and $\text{Cu}_{2-x}\text{O}/\text{n-Si}$ heterojunctions [29]. It is found that the $\text{Cu}_{2-x}\text{O}/\text{n-Si}$ heterojunction present much higher performance over $\text{CuI}/\text{n-Si}$ with a high responsivity of 417 mA W^{-1} . It could be explained by the favorable band alignment of $\text{Cu}_{2-x}\text{O}/\text{n-Si}$ heterojunction, where the upward band bending of silicon and downward band bending of Cu_{2-x}O forming a cliff-like configuration, thus facilitate the electron–hole transfer. In contrast, the spike-like band alignment in $\text{CuI}/\text{n-Si}$ interface results in the trapping of electrons and barrier for holes.

2.2. Isotype or anisotype

Based on the conductivity, heterojunctions can be classified into two types: isotype, where two semiconductors are both n-type or p-type, or anisotype, where two semiconductors form a p–n heterojunction. For the anisotype type-II heterojunction, similar to that of the p–n homojunction, the band alignment under thermal equilibrium is due to the process of electron/hole diffusion in the interface. When a heterojunction is formed, the excess number of electrons in the n-type semiconductor would diffuse into the p-type semiconductor, and vice versa. As the electrons and holes diffuse, there will be positively charged donor atoms and negatively charged acceptor atoms left in the n-type and p-type semiconductors, respectively. As a result, the depletion regions generated in both n-type and p-type semiconductors, with a net positive and a negative charge, respectively. Such net charges generate an electric field with the direction from the n-type semiconductor to the p-type semiconductor, which provides an opposite force to the charge diffusion. As the electric field increase to the exact value of the diffusion, the junction reaches thermal equilibrium.

A thorough investigation of anisotype (p-Si/n-ZnO) and isotype (n-Si/n-ZnO) heterojunction photodiodes gave a good example of the influence of conductivity on the performance of the type-II heterojunctions [30]. The p-Si/n-ZnO and n-Si/n-ZnO exhibit opposite rectification behaviors, due to the dissimilar energy band structures. For the anisotype heterojunction, it behaves as a typical p–n junction diode as the barrier, which is the difference between the valence bands of Si and ZnO, and only exists when a positive

voltage is applied (Fig. 3c). For the isotype heterojunction, the majority carrier electrons have to pass through ΔE_C or $\Delta B_{\text{He-Si}}$, when a positive or negative voltage is applied, respectively (Fig. 3d). The bias-independent ΔE_C leads to the low leakage current at positive voltage. On the other hand, the bias-dependent barrier $\Delta B_{\text{He-Si}}$ decreases as negative voltage increases, thus, a large current at negative voltage can be collected. More importantly, the p-Si/n-ZnO and n-Si/n-ZnO heterojunctions present different photoresponse under bias conditions. As we know, photodiodes are preferably operated under the reverse bias condition. For p-Si/n-ZnO heterojunction, when a negative voltage is applied, the reverse-biased condition leads to more electrons and holes generation and more effectively separation due to the expanded depletion width and enhanced electric field. Thus, the p-Si/n-ZnO heterojunction PD presents a distinct photoresponse at a negative voltage (Fig. 3a). On the contrary, the n-Si/n-ZnO heterojunction operated on the reverse-biased condition and presents a notable photoresponse when a positive voltage is applied (Fig. 3b). Furthermore, both p-Si/n-ZnO and n-Si/n-ZnO heterojunctions exhibit an even more profound distinct photoresponse under external compressive strain, owing to the well-known piezotronic and piezo-photronics effect.

Interestingly, the distinct photoresponse was not observed in a similar study conducted on n-Si/n-CdS and p-Si/n-CdS heterojunctions [31]. As shown in Fig. 3e and f, the n-Si/n-CdS heterojunction exhibit a similar yet much better photoresponse performance compared to the p-Si/n-CdS heterojunction. It is believed that the width of the depletion region plays a crucial role in the latter research, as shown in Fig. 3g and h. The depletion region is only formed at the Si side for the n-Si/n-CdS but both sides for the p-Si/n-CdS heterojunction. The applied positive bias leads to a hole accumulation region or an expanded depletion region at the p-Si side, for the p-Si/n-CdS and n-Si/n-CdS heterojunctions, respectively. Since the photo-generated carriers are mainly produced at the Si side, the expanded depletion region of n-Si/n-CdS results in a much better photoresponse.

For n–n heterojunctions, the band alignment is realized by the electrons flow from the material with the higher Fermi level to the lower Fermi level, resulting in the forming of a depletion region and an accumulation region on each side of the junction. Since no minority carrier injection is involved, it is believed that the devices should be fast in switching response [32]. Using a solution-processed precursor deposition, Lee et al. reported the synthesis of large-scale and highly crystalline MoS_2 and WS_2 monolayers [33]. The n-MoS₂/n-WS₂ heterojunction exhibit a typical rectifying behavior due to the type-II band alignment, as shown in the I–V curves in Fig. 3i. Importantly, the MoS₂/WS₂ heterojunction exhibits a great improvement in the response time under the reverse bias compared to the forward bias (Fig. 3j and k). As shown in Fig. 3l, under the forward bias, both the electron depletion region and the electron accumulation region decrease, resulting in the built-in potential across the junction region also decreases. Thus, the heterojunction device exhibits a long response time since the small potential barrier almost vanishes, resulting in the carriers releasing from the trap sites and flowing through the channel even after the incident light is turned off. On the contract, under the reverse bias, the n-n type-II MoS₂/WS₂ heterojunction device shows a significantly improved response time of 45 ms compared to its p–n counterpart, as well as a high photoresponsivity of $\approx 40 \text{ A W}^{-1}$. The increased built-in potential under the reverse bias hinders the electrons to overcome the barrier (Fig. 3m). As a result, the dominating transport of the electrons as the majority-carrier in the n–n heterojunction presents a relatively long carrier lifetime compared to that of a conventional p–n junction.

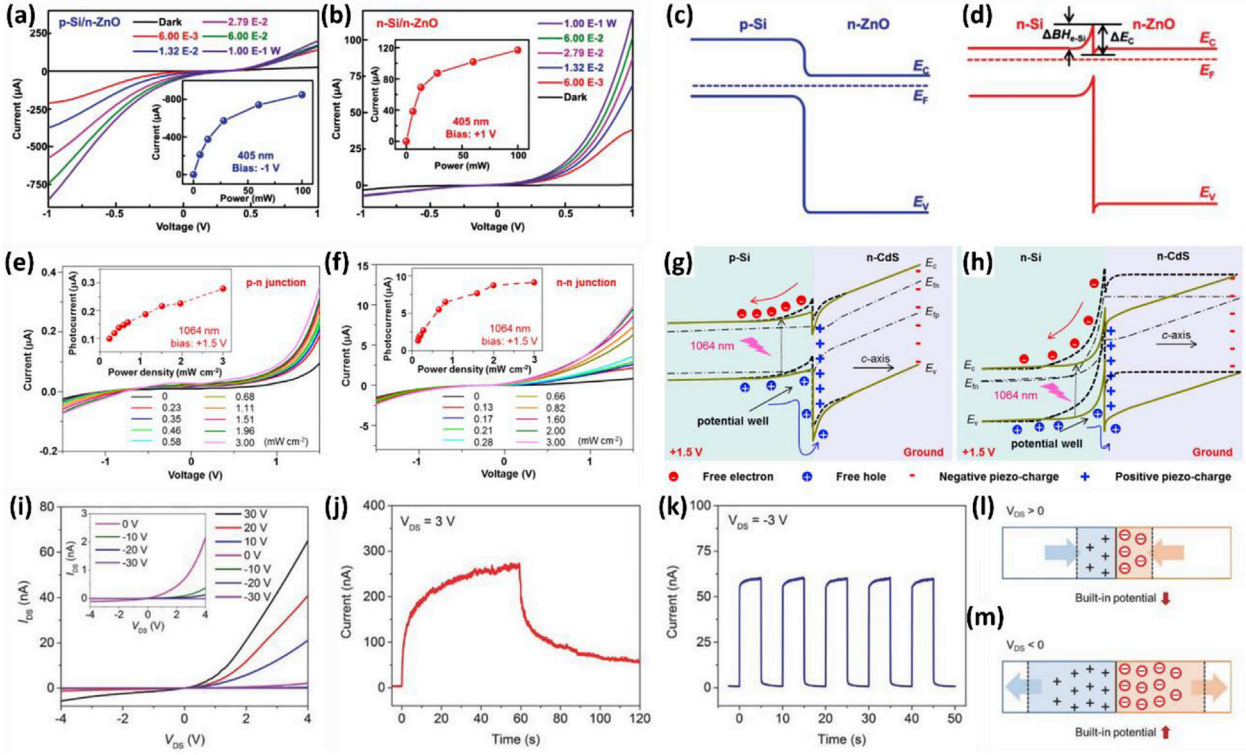


Fig. 3. a,b) I–V characteristics of the p-Si/n-ZnO and the n-Si/n-ZnO heterojunctions different optical powers. c,d) Energy band diagrams of the p-Si/n-ZnO and the n-Si/n-ZnO heterojunction PDs under 0 V bias and dark condition. Reproduced with permission [30]. Copyright © 2018 WILEY-VCH Verlag GmbH & Co. KGaA, Weinheim. e,f) I–V characteristics under different 1,064 nm illumination power densities when a 1.5 V bias is applied for the p–n and n–n Si/CdS heterojunctions, respectively. g,h) Schematic band diagrams of p-Si/n-CdS and n-Si/n-CdS heterojunctions under 1.5 V forward bias. Note the dark yellow line are the band diagrams under compressive strain. Reproduced with permission [31]. Copyright © 2017 Elsevier Ltd. i) I–V curves of the n-MoS₂/n-WS₂ heterojunction. g,k) Photoresponse of the n-MoS₂/n-WS₂ heterojunction device at forward bias and reverse bias, respectively. l,m) Schematic of the size of the built-in potential of the n-MoS₂/n-WS₂ heterojunction forward bias and reverse bias, respectively. Reproduced with permission [33]. Copyright © 2017 WILEY-VCH Verlag GmbH & Co. KGaA, Weinheim.

2.3. Crystal structure

It is well known that the crystal structure plays a vitally important role in determining the optical and electronic properties of the semiconductors. Such influence becomes even more complex in the case of heterojunctions when a large number of factors have to be taken into account, such as band offset, direct or indirect bandgap, lattice mismatch, crystal orientation, thermal stability and so on. Therefore, tailoring the crystal structure as desired has always been the key to the construction of high-quality heterojunctions [34]. Fu et al. investigated the crystal phase-modified band alignment in CdS/SnS_x [35]. By varying the reaction parameters such as precursor concentrations and reaction time, 2D SnS_x nanosheets with controlled crystal phases are deposited on the 1D CdS, resulting in three different band alignments. As shown in Fig. 4a–c, the orthorhombic SnS and CdS form a type-I heterojunction, whilst the heterojunction formed by CdS and hexagonal SnS₂, as well as mixed-phase of orthorhombic and zinc blende SnS are type-II. Among them, the heterojunction of hexagonal-SnS/CdS exhibits the best performance for water splitting because of its type-II alignment and larger conduction band offset.

In most cases, the heterojunctions are formed by two distinct materials. There is one particular case in which two different polymorphs of the same material forming a heterojunction, often being referred to as the phase junction [36,37]. As one of the most promising candidates for photocatalytic applications, TiO₂ has four main polymorph phases: rutile, anatase, brookite, and TiO₂ (B). Owing to the type-II band alignment in the mixed-phase rutile and anatase TiO₂, which significantly lowers the effective bandgap and facilitating

efficient electron/hole separation, it exhibits a significant higher photocatalytic activity than their pristine compositions [38–43]. Similarly, the type-II phase junction can also be realized in other mixed-phase of TiO₂, such as anatase/TiO₂ (B) and anatase/brookite [44–46]. Besides TiO₂, the phase junctions based on other materials with different polymorphs have also been demonstrated, including Ga₂O₃ (α , β , and γ phases) [47,48], Bi₂O₃ (α and β phases) [49,50], CaTa₂O₆ (α and β phases) [51], BiVO₄ (monoclinic and tetragonal) [52,53], CdS (hexagonal and cubic) [54–56], etc. Though the majority of efforts have been dedicated to the photocatalytic and photoelectrocatalytic applications, the remarkable progress has been made in the utilization of the phase junction in other optoelectronics as well, such as solar cells, photodetectors, and light emitters [57–65].

Apart from the crystal phase, the charge transfer/separation process is largely affected by the selective exposure of facets, which exhibit distinctive electronic and optical properties due to the different atomic coordination and configurations [66]. Given this, a novel facet heterojunction (surface heterojunction) concept was introduced, providing a possibility of construction of heterojunction within the same material, which is similar to orientational heterostructure [67,68]. For example, a type-II surface junction formed in the single-phase anatase TiO₂ due to the synergy of the favored band structures and the epitaxial interface between the co-exposed {101} and {001} facets, resulting in the efficient separation of photogenerated electron/hole pairs and enhanced photocatalytic activity [69,70]. After that, the facet heterojunction have been observed in other semiconductors, such as CeO₂ ({100} and {111} facets) [71], BiVO₄ ({010} and {110} facets) [72], and Bi₂O₃ ({010} and {100} facets) [73]. Such principles have shown great promise in

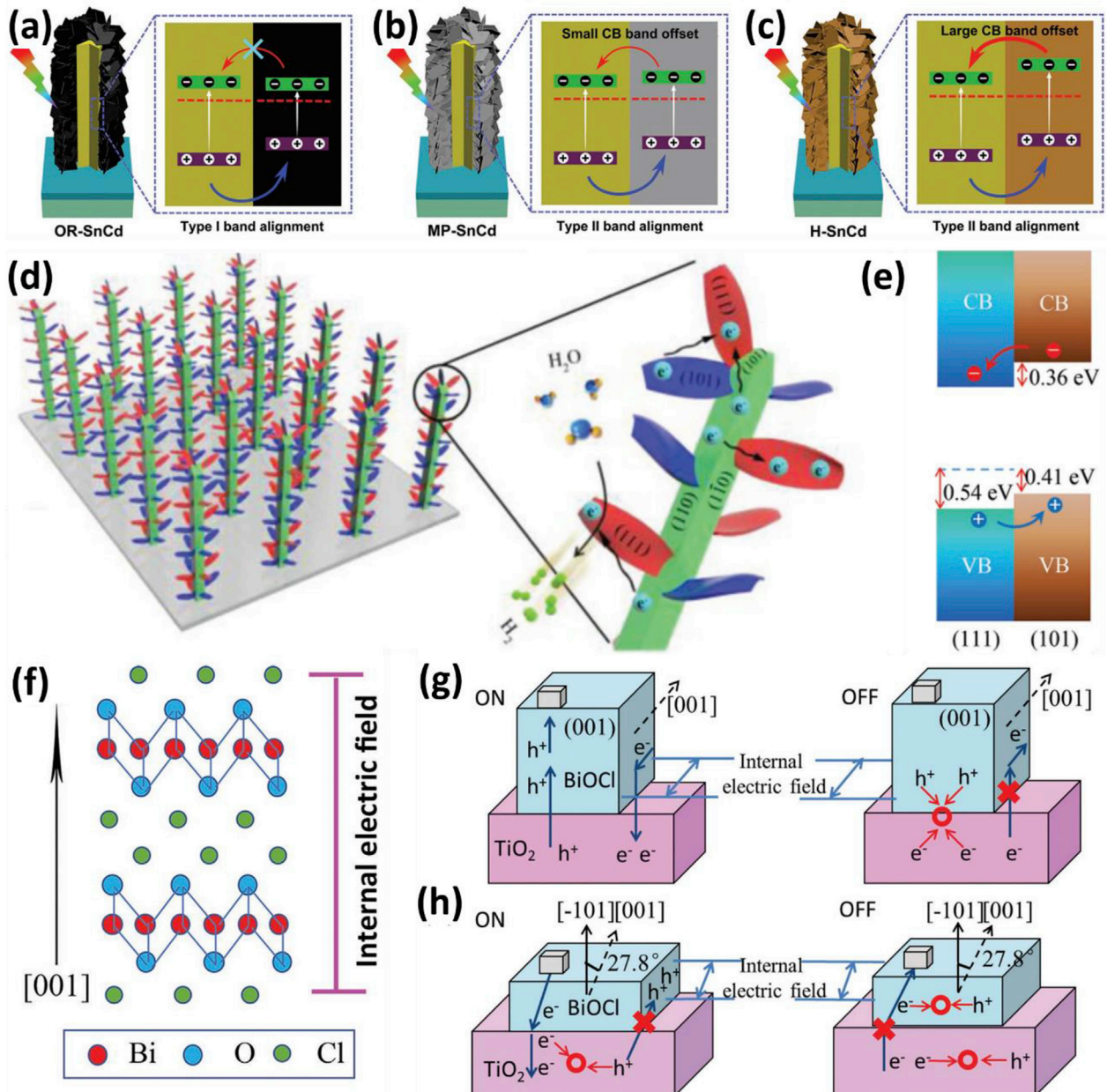


Fig. 4. a–c) Schematics and band diagrams of orthorhombic SnS/CdS, hexagonal SnS₂/CdS, and mixed-phase of orthorhombic and zinc blende SnS/CdS heterojunctions. Reproduced with permission [35]. Copyright © 2018 WILEY-VCH Verlag GmbH & Co. KGaA, Weinheim. d) Schematic diagrams for the facet heterojunction TiO₂ arrays. e) Band diagram of the (111)/(101) rutile TiO₂ heterojunction. Reproduced with permission [74]. Copyright © 2019 WILEY-VCH Verlag GmbH & Co. KGaA, Weinheim. f) The crystal structure and the internal electric field of the BiOCl nanosheets. g,h) Schematic illustrations of the transfer behaviors of carriers in BiOCl nanosheets with different growth orientations on the TiO₂ nanotube arrays under dark and light illumination, respectively. Reproduced with permission [75]. Copyright © 2018 WILEY-VCH Verlag GmbH & Co. KGaA, Weinheim.

guiding the material design for more complex structures. By designing a type-II band alignment in the (111)/(101) facets, Gao et al. have constructed a 3D hierarchical nanostructure based on rutile TiO₂ nanosheets and nanorods [74]. In their design, ultrathin rutile TiO₂ nanosheets with different facets are coated onto rutile TiO₂ nanorod, thus the facet heterojunctions are formed among the nanosheets and between the nanosheets and nanorod (Fig. 4d). The first-principles calculations confirm the type-II band alignment of the (111)/(101) heterojunction (Fig. 4e). As a result, the facet heterojunction structure exhibits a remarkable 45-fold increase in the photocurrent compared to bare TiO₂ nanorods.

Modulation of the heterojunction property can be also realized by the self-induced internal electric fields of the material, known as

the built-in polarization. One example is the BiOCl nanosheets/TiO₂ nanotube heterojunction [75]. As shown in Fig. 4f–h, BiOCl has a unique crystal structure that consists of tetragonal $[Bi_2O_2]^{2+}$ positive slabs interleaved by double negative slabs of Cl atoms. Such structure creates an internal electrical field along the [001] direction, making the photogenerated electrons and holes trend to transfer along the [001] direction, and in the direction parallel with the layered slabs, respectively. With the proper loading amount and growth orientation, the synergistic effect of the heterojunction and the self-induced internal electric field facilitates carrier separation and transportation regulation, leading to a significant improvement in photodetector performance, such as a dramatically decreased dark current (≈ 1 nA) and an ultrahigh on/off ratio (up to 2.2×10^5).

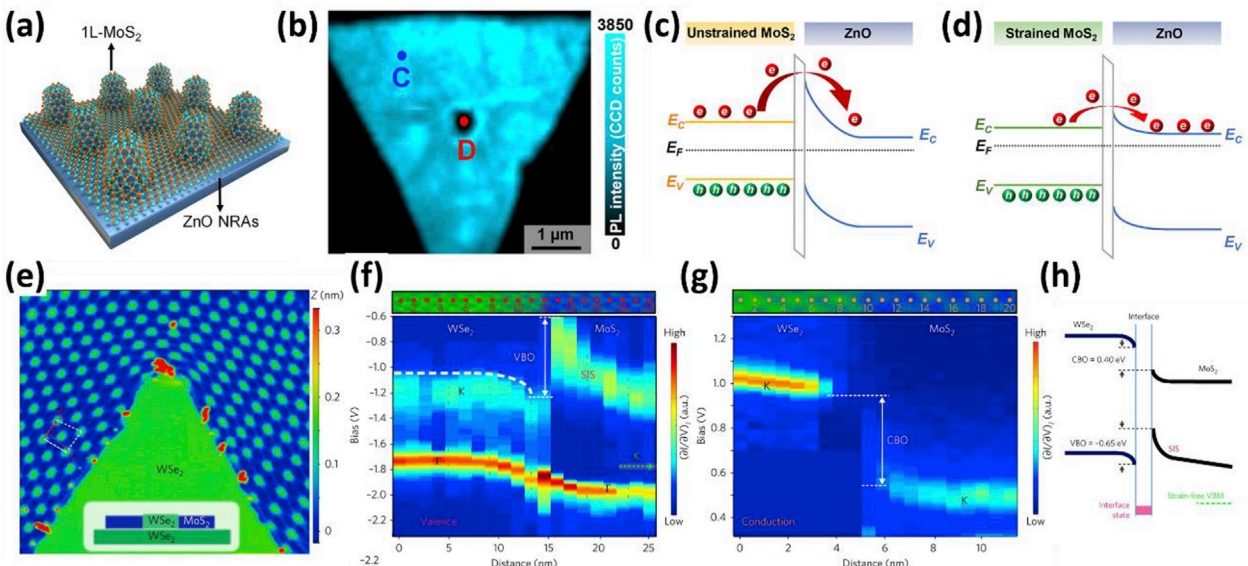


Fig. 5. a) The schematic of the MoS₂/ZnO heterojunction arrays. b) Scanning PL maps with integrated peak intensity (1.75–1.85 eV) of the MoS₂ on the ZnO nanorods substrate. c,d) The schematic illustration of the interfacial charge transfer based on the band diagram of pristine MoS₂/ZnO and strained MoS₂/ZnO, respectively. Reproduced with permission [77]. Copyright © 2018 American Chemical Society. e) STM image of a lateral WSe₂/MoS₂ heterojunction stacked on top of a monolayer WSe₂. A moiré pattern with serious distortion is observed. f,g) Color-coded mappings for the valence band and conduction band, respectively. h) The band diagram of WSe₂/MoS₂ heterojunction with strain. Reproduced with permission [78]. Copyright © 2018 Macmillan Publishers Limited.

2.4. Strain engineering

It is widely known that strained materials show modified properties compared to the pristine bulk ones. On one hand, the strain caused by the lattice mismatch usually associated with the undesired interface defects, which trap the photogenerated carriers and thus prevent the diffusion of electrons and holes. In a recent study, Rashmi et al. screened some of the most commonly studied semiconductor material, such as TiO₂, ZnO, BiVO₄, CdSe, and ZnS, in their possibility to form type-II heterojunctions [76]. According to the authors, despite that majority of materials combinations, 221 out of 297, meet the criteria in terms of the band edge and band offset, the lattice misfit seems more critical. After the coherency and lattice misfit strain being considered, the possible type-II heterostructure combinations have been significantly restricted to 19 [76]. The rest incoherent interfaces are expected to generate a large density of defect states and limit the efficient carrier transfer at the interface. Nevertheless, owing to the large tolerance to lattice mismatch, nanoscale heterojunctions demonstrated advantages in overcoming the undesired lattice relation. As an example, a type-II core/shell ZnO/ZnSe nanowires heterojunction with a huge lattice mismatch of more than 20% was shown possible [13].

On the other hand, as elastic strain tunes the materials lattice constants, its presence in semiconductor heterojunctions will change their electronic band alignments, paving alternative routes in bandgap engineering. Liu et al. reported an effective strain engineering strategy on van der Waals interfaces by constructing a mixed-dimensional heterostructure array based on monolayer MoS₂ and ZnO nanorod arrays, as shown in Fig. 5a [77]. As a result, a periodically gradient biaxial-strain was applied on the monolayer MoS₂ by the patterned one-dimensional ZnO-induced nano-indentation, resulting in a strain-optimized interfacial carrier behavior evidenced by the decreased PL signal at strain-concentrated regimes (Fig. 5b). Such an effect can be attributed to the modulation of the band alignment, particularly the shift of the Fermi level in MoS₂. As the Fermi level of MoS₂ shifts up under the tensile strain, the band bending of ZnO reduces as a result of the

lowed built-in field, leading to the decreased barrier height and facilitated carrier transfer from MoS₂ to ZnO (Fig. 5c and d). Using scanning tunneling microscopy and scanning tunneling spectroscopy, the strain tensor and the corresponding band alignment of the WSe₂/MoS₂ lateral heterojunction were measured directly [78]. As shown in Fig. 5e,a moiré pattern with serious distortion is observed in the MoS₂ region, indicating the local 2D strain tensor in the MoS₂ atomic lattice. Remarkably, the strain field causes an unexpected spatial variation of the electronic MoS₂ valence band structure, leading to a conversion of the otherwise type-II to type-I band alignment (Fig. 5f–h).

2.5. Structure optimization

Based on the confined dimensionality, nanomaterials can be classified as zero-dimensional (0D), one-dimensional (1D), and two-dimensional (2D) nanomaterials. Importantly, discrete energy levels may arise in different dimensional heterojunctions owing to their distinct quantum confinement effects, thus causing the energy band structures to deviate from each other. Therefore, structure optimization makes a great difference to the optoelectronic properties of the heterojunctions.

2.5.1. 0D structure

Heterojunctions based on 0D nanomaterials, such as quantum dots, have been used as the building blocks for various optoelectronic applications. The core/shell configuration is among the most commonly studied 0D heterostructure. Compared to the bare QDs, core/shell QDs offer further degrees of tuning of the optoelectronic properties by band alignment engineering. In addition, the core/shell QDs can greatly improve long-term stability by passivating the unsaturated surface defects and trap sites to reduce the recombination loss; as well as preventing environmental effects such as oxidation [79]. Since core/shell quantum dots with the size that similar to or less than that of the de Broglie wavelength exhibit pronounced quantum size effects, tailoring the core size and shell thickness has been proven a powerful tool to modify its band

structures. For example, Kim et al. have reported the efficient band offset tailing in type-II CdTe/CdSe core/shell quantum dots by controlling the shell thickness as well as the core size, resulting in the modification of emission spectra from 700 nm to over 1,000 nm [80].

In photovoltaics, the electron/hole pair will be produced when an incoming photon with energy in excess of the bandgap being absorbed by the semiconductor. In most cases, one photon can only generate one electron/hole pair, called the hot carriers, as they tend to thermally relax to the conduction band edge and valence band edge rapidly, resulting in the Shockley–Quiesser limit of 31% solar to electrical energy conversion efficiency. Several approaches have been developed to overcome such limitations, such as multi-junction or tandem solar cells. Another promising direction is to generate more than one pair of electron/hole upon single-photon absorption through the multiple exciton generation (MEG). However, the MEG effect is inefficient in bulk semiconductors due to the rapid thermalization process. On the other hand, quantum dots offer improved MEG efficiencies because of the carrier confinement in all three spatial dimensions [81]. In particular, the type-II heterojunctions have been considered as a promising candidate due to the spatial separation of the photo-generated hole–electron pair [82]. For example, Klimov and co-workers demonstrated an almost fourfold enhancement of multiexciton yield as well as the considerable reduction of the MEG threshold by constructing the PbSe/CdSe core/shell quantum dots [83]. The enhanced MEG is mainly attributed to the slower hot carrier relaxation rate due to the quasi-type-II band structure, which confining the hole wave functions around the core, while the electron wave functions are spread over the whole structure (Fig. 6a). The strongly confined wavefunction of the hole results in an increase in the core valence level energetic gap (ΔE_{cool}), and thus slows down the hole relaxation. The reduced wavefunction overlap between the lower energy core and higher energy shell valence levels further reduced the hole relaxation. Furthermore, the increased Coulomb coupling between core-localized valence band carriers leads to the decreased spatial separation between them (d_{ee}). The core/shell PbSe/CdSe QDs also exhibits a reduced carrier multiplication threshold compared with PbSe QDs. Since the absorption at high energies is dominated by the

CdSe shell, the excitation near the shell band edge leads to a strongly asymmetric state. As a result, a fourfold increase in carrier multiplication efficiency, and a reduction in threshold energy to close to 2 E_g were achieved. Using pseudopotential atomistic calculation on a type-II nanorod model, Eshet et al. predicted the improved threshold close to two times the bandgap can be achieved by two combined effects: a sharp interface with increased band offsets and slow exciton cooling rate by reducing the electron–phonon couplings [84].

The light-emitting diode relies on the recombination of electrons and holes and the emitting of photons. At first glance, type-II alignment does not appear to be the perfect choice for the application in LEDs, since the holes and electrons are spatially separated [85]. As a matter of fact, modern inorganic LED designs are based on the concept of type-I double heterojunction [86]. Compared to conventional p–n junction LEDs, double heterojunction LEDs possess major advantages due to the efficient carrier confinement, allowing the significant increase of carrier density. If we consider the core/shell quantum dots, the double heterojunction configuration is analogous to the type-I band alignment. However, the presence of electrons and holes in the same regime may cause unfavorable nonradiative recombination. One of the major obstacles that limiting the performance of LEDs is Auger recombination, which transfers the energy of excitons to a third carrier and dissipates it as heat, causing significant luminescence efficiency reduction, known as efficiency roll-off or droop [87]. Therefore, suppressing the Auger recombination is of great importance in designing high-performance LEDs. Reducing the overlap of electron/hole wave functions using type-II or quasi-type-II alignments is an effective method to suppress the Auger recombination. For example, a significantly elongated Auger recombination lifetimes was observed in the case of CdTe/CdSe type-II QDs up to a nanosecond time scale [88]. Bae et al. reported a quasi-type-II CdSe/CdS core/shell QDs by constructing CdSe_xS_{1-x} alloy layer between the CdSe core and the CdS shell (Fig. 6b) [89]. The reduced valence-band offset resulted from the CdSe_xS_{1-x} alloy layer creates an energy gradient that facilitates hole migration from the CdS shell to the CdSe core, thus confining the hole in the CdSe core, while the electron is largely delocalized over the entire QD. As a result, the

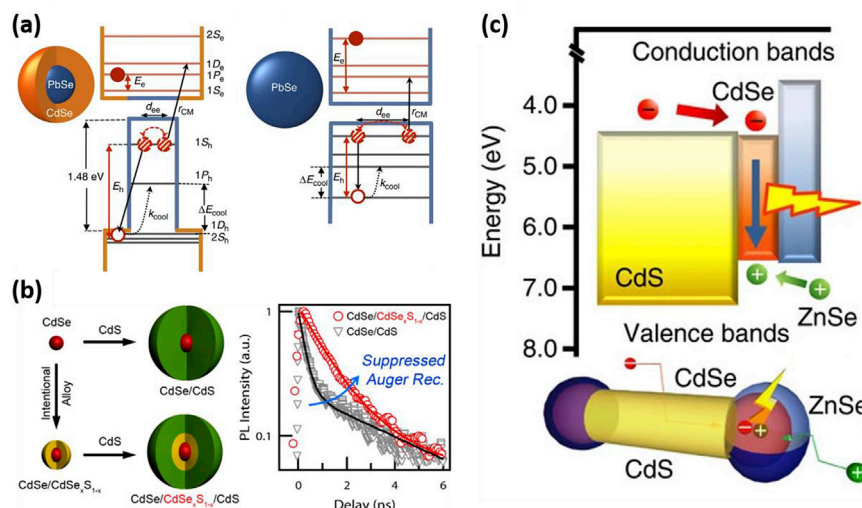


Fig. 6. a) Schematic, band structure, and relaxation processes of a PbSe/CdSe core/shell QD and a core-only PbSe QD, respectively. Reproduced with permission [83]. Copyright © 2014 Macmillan Publishers Limited. b) Schematic and PL lifetimes of abrupt interface CdSe/CdS core/shell and alloyed interface CdSe/CdSe_xS_{1-x}/CdS core/alloy/shell QDs. Reproduced with permission [89]. Copyright © 2013 American Chemical Society. c) Energy band diagram and schematic of the geometric structure of double-heterojunction nanorod consisting of type-II band offset CdS and ZnSe both in contact with the emitting smaller bandgap CdSe quantum dot. Reproduced with permission [94]. Copyright © 2014 Macmillan Publishers Limited.

quasi-type-II CdSe/CdS core/shell QDs exhibit a significant improvement of the multiexciton decay, indicating suppression of Auger recombination. In addition, the local electric field of spatially separated electrons/holes in type-II heterojunctions leads to a strong exciton–exciton repulsion and therefore a Stark shift of the absorption spectrum. As a result, the single-exciton gain with no multiexciton Auger recombination demonstrated great potential in optical amplification and lasing [90,91].

However, low photoluminescence quantum yield remains a major challenge for type-II heterojunction to be utilized in LED applications since the decreased overlap of electron/hole also contributes to the reduced radiative recombination [92]. Several approaches have been developed to improve the light-emitting performance of type-II heterojunctions. For example, Tyrakowski et al. reported the enhancement of the radiative lifetime via surface passivation [93]. In their study, a ZnS layer was coated on the surface of the ZnSe/CdS core/shell type-II QDs and results in an improvement of quantum yield as high as 61%. Interestingly, the enhancement of the quantum yields was attributed to the increase of radiative rate, rather than the suppression of surface trap-related nonradiative processes. Oh et al. developed a double-heterojunction strategy, in which two distinct semiconductor materials (CdS and ZnSe) that would form a type-II band alignment are in contact with the opposite end of one material with smaller bandgap (CdSe), which allows control over the electron and hole injection/extraction processes independently (Fig. 6c) [94].

2.5.2. 1D structure

Nano-heterojunctions based on 1D semiconductor nanostructures such as nanowires, nanobelts, nanorods, and nanotubes have drawn tremendous interests as the promising platform for electronics and optoelectronics applications owing to their unique properties. For solar cells and photodetectors, the large aspect ratio of 1D structures provide more efficient light absorption. In addition, the large geometrical anisotropy along different dimensions shortens the carrier transit time while prolongs the photon absorption path length [95,96]. For LEDs, significant improvement of internal quantum efficiency has been demonstrated using 1D structures via the modification of spontaneous emission as well as the light extraction efficiency via the light flow molding [96]. Furthermore, the 1D structure can act as waveguides and provide sufficient resonant feedback for semiconductor lasers [97].

In general, 1D heterojunctions can be classified into axial or radial heterojunctions. For the axial heterojunctions, the elastic relaxation is much more efficient, thus leading to a wider choice of the material combination compared to the thin-film structures. Ideally, a dislocation-free layer with arbitrary thickness can be obtained, as the critical thickness beyond which interfacial dislocations appear, is depended on the radius of the nanowire and becomes infinite for radii less than some critical value [98]. In comparison with radial heterojunctions, axial heterojunctions have a particular advantage in construction multi-junction for tandem architectures [99]. However, it is more challenging to synthesize the axial heterojunction in practical due to the stringent requirements of crystallographic relationships [100]. Lu et al. reported the synthesis of vertically aligned ZnO/ZnS axial heterojunctions using a one-step thermal evaporation process and demonstrated their piezotronics property [101]. With a junction formed along the axial direction, the electronic or photonic properties of axial heterojunctions exhibit unique interface polarity dependence, especially for III–V and II–VI semiconductors [102]. Schuster et al. studied the emission dependence on the polarity of GaN/ZnO heterojunction [103]. Their simulations based on different polarity configurations reveal the strong dependence of band structure and electric field on the polarity. Furthermore, a polarity

inversion from N-polar for GaN to Zn-polar for ZnO is observed experimentally.

For radial heterojunctions, the core/shell configuration is the most commonly studied case. One particular advantage of the core/shell configuration is to decouple the directions of light absorption and charge carrier transfer, allowing the carriers to be separated efficiently across the radial heterojunction with a short transfer path while maintaining the strong absorption length of the nanowire [104]. Therefore, core/shell heterojunctions have demonstrated great promising for solar cells and photodetectors. For example, we have successfully synthesized nearly lattice-matched all wurtzite CdSe/ZnTe core-shell nanowires on silicon substrates using a two-step method combining thermal evaporation and pulsed laser deposition [105]. The small lattice mismatch of ~0.08% between CdSe and ZnTe leads to a sharp, core-shell interface, indicating that the core is acting as a structural template for the shell. Further photoluminescence and Raman spectroscopy characterizations confirm the type-II band alignment and efficient charge separation of photogenerated electron/hole pairs across the CdSe/ZnTe interface. On the other hand, the rational design of the surface and interface geometry can be utilized to engineering the light scattering, transmission, and reflection, thus further improve the light absorption and the device performance. Recently, Hu et al. designed a unique Ω-shaped core/shell photodetector based on electrospun SnO₂ nanofibers, and ALD deposited ZnO [106]. The theoretical simulations by the FDTD method demonstrated the great enhancement of the light-trapping when illuminated from the backside. As a result, the photodetector exhibits a high photo-to-dark current ratio up to 10⁴ at around 280 nm. Additionally, it possesses a significantly improved UV selectivity with a UV-vis rejection ratio of 2.0 × 10³, attributed to light confinement in the Ω-shaped structure. Regarding the 1D nanostructure, a vertically aligned array structure provides additional advantages such as enhanced light collection, more efficient carrier collection, and possible cost reduction. Our group reported a vertically aligned CdSe/CdTe core/shell nanowire arrays photodetector [107]. By designing a type-II heterojunction structure, the detection range of the device has been successfully extended to the near-infrared range. Furthermore, the vertically aligned structure allows the further improvement of the device performance by applying the piezo-phototronic effect, leading to 4 orders of magnitude improvement of photoresponsivity.

Furthermore, the 1D structure provides an important platform to be integrated with other dimensional nanomaterials [108,109]. One typical example is the QD-sensitized solar cell, in which light is absorbed by QDs and the excited electrons are injected into the transparent metal oxides like TiO₂ or ZnO. In comparison to the nanoparticle in which the disordered inner connection may hinder the efficient charge transportation, it is well believed that the 1D structure can facilitate the photogenerated carrier transfer and thus decrease the recombination loss [110]. However, the potential of 1D structured QD-sensitized solar cell is yet to be fully explored, mainly because of the low QD-loading amount [111]. To further push the performance of solar cells to the limit, it is of great importance to gain a fundamental understanding of the optoelectronic processes at the nanoscale interface. In this content, Sun and co-workers have established a “nanolab” platform in the TEM for in situ photoelectrical studies [112]. In order to perform the in-situ investigation, the authors designed a state-of-the-art TEM holder by incorporating a light source within the holder. As shown in Fig. 7, a TiO₂ nanowire/CdSe QDs solar cell was used as an example with a typical J–V curve. The influence of the defect on the solar cell performance was systematically investigated by in-situ controlling the position of the Pt electrode. Interestingly, a clear decrease of the photocurrent density was observed as the interface area increases,

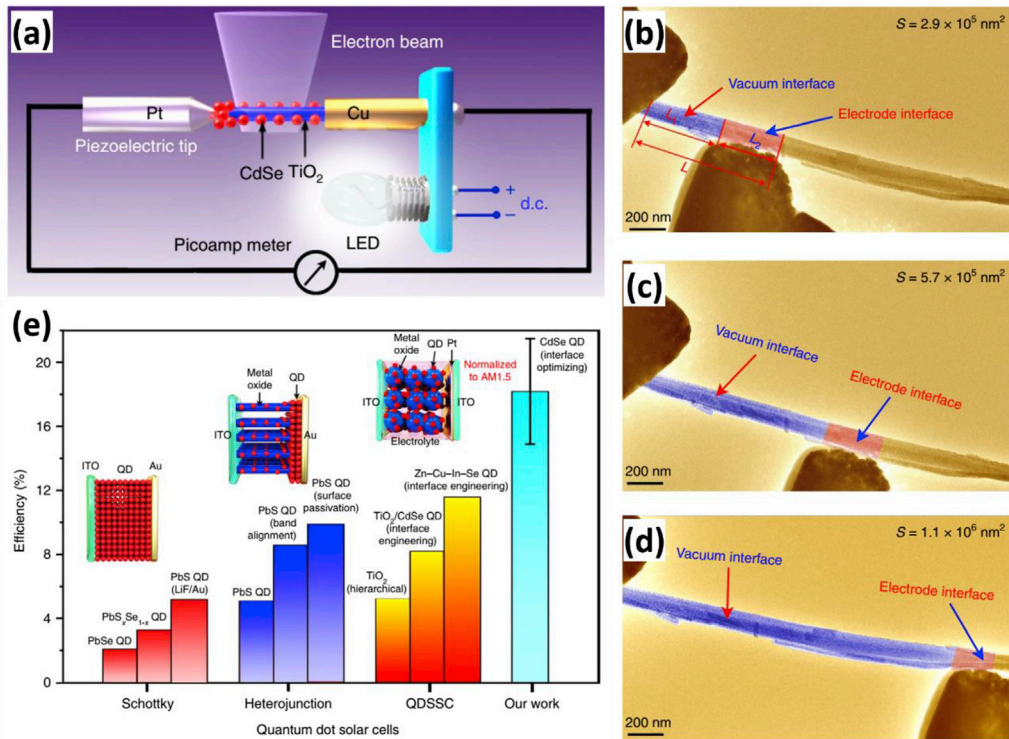


Fig. 7. a) Schematic diagram of the in situ fabrication of an individual TiO_2 nanowire/CdSe QDs heterojunction solar cell. b–d) TEM images of the heterojunction solar cell devices with the different interface areas (the interface is highlighted using false color). e) Comparison of the efficiency of different QD-based solar cells. Reproduced with permission [112]. Copyright © 2019 Springer Nature Limited.

confirming the interface associated defects as the major limitation to the performance of the solar cell.

2.5.3. 2D structure

Heterojunctions based on 2D material have attracted tremendous research interests due to their unique structures and excellent electronic and optoelectronic properties. In contrast to traditional heterostructures in which different materials are epitaxially grown, arbitrary combinations of 2D layer materials can be stacked mechanically with the help of the weak van der Waals interlayer interactions to form the vertical heterojunctions without the strict lattice match limitation. Therefore, it offers tremendous possibilities in construction heterojunctions with diverse functions that are not possible elsewhere [18,113].

Because of the atomic thickness layer structure, the Van der Waals heterojunctions exhibit many intriguing optoelectronic properties. Among different 2D materials, transition metal dichalcogenides (TMDs) have received tremendous interests owing to their unique electronic and optical properties, such as high carrier mobility, strong light–matter interaction. In addition, the van der Waals heterojunctions provide perfect platforms to probe the optoelectronics process and the underlying physics mechanism at the atomic scale. By using the femtosecond pump-probe spectroscopy, Hong et al. investigated the dynamical charge transfer in atomically thin MoS_2/WS_2 heterostructures [114]. Using femtosecond pump-probe spectroscopy, an ultra-fast transfer rate of the photo-generated holes from the MoS_2 layer to the WS_2 layer within 50 fs was observed. A similar dynamic was observed in $\text{MoS}_2/\text{MoSe}_2$ heterojunction, where the electrons transfer from MoSe_2 to MoS_2 and the holes in the opposite direction on the same sub-picosecond time scale [115]. Additionally, spatially indirect excitons with longer recombination lifetimes were formed by the electrons and holes

after transfer. On the other hand, Rivera et al. measured the long-lived interlayer excitons in monolayer $\text{MoSe}_2-\text{WSe}_2$ heterojunctions of ~1.8 ns lifetime, an order of magnitude longer than intralayer excitons in individual monolayers due to the type-II band alignment [116]. Furthermore, Kozawa et al. observed the interlayer energy transfer between strongly bound in-plane excitonic dipoles [117]. Overall, the ultrafast charge transfer and long electron/hole recombination times suggest that Van der Waals heterojunctions should be promising candidates for various optoelectronic applications [118].

Besides the van der Waals stacked heterojunctions, it is feasible to create a lateral heterojunction by forming an in-plane line interface between 2D materials. Compared to the Van der Waals heterojunctions, it is challenging to grow lateral heterojunctions because of the strong in-plane covalent bonds, but often provides unique band alignment and strong built-in field. In most cases, realizing the lateral heterojunctions is achieved by the edge epitaxy method, which relies on the growth of one TMD on the active edge of a dissimilar TMD [119]. For example, Li et al. reported the synthesis of a lateral $\text{WSe}_2-\text{MoS}_2$ heterojunction via a two-step epitaxial growth [120]. The WSe_2 layer was first grown on the sapphire substrate, followed by the edge epitaxy of MoS_2 along the W growth front. Despite the large lattice mismatch, an atomically sharp interface was observed by the high-resolution scanning transmission electron microscopy. Furthermore, the $\text{WSe}_2/\text{MoS}_2$ heterojunction device exhibits excellent electronic and optoelectronic properties, such as a good rectification character and an obvious photovoltaic effect.

2.5.4. Mixed-dimensional structure

Although each class of low-dimensional structures possesses advantageous optical and electronic properties, there are some

intrinsic limitations. For example, the 0D materials may potentially have high light emission quantum yields, as the carrier localization tends to suppress nonradiative recombination loss; however, films of 0D materials generally have low carrier mobilities due to large tunneling barriers. 1D systems, especially those with array structures, typically have relatively large sizes in the range of 100 nm, thus exhibit less profound quantum confinement effect. 2D materials, in particular those a-few-monolayer structures, have small active volume, thus usually cannot offer adequate optical absorption for detection related applications; and are more sensitive to structural defects, thus tend to yield low light emission quantum yields. By combining the nanomaterials of differing dimensionalities, mixed-dimensional heterojunctions present some unique properties and thus provide an alternative to bypass the intrinsic limitations. One typical example of the mixed-dimensional heterojunctions is the 0D–1D QD-sensitized solar cells as we mentioned before. Here, we would like to discuss the emergent mixed-dimensional van der Waals heterojunctions. As we know, the van der Waals interactions are the key to form the vertical 2D heterojunctions. However, the van der Waals interactions are not limited to the 2D layered materials. Since the surface of most low-dimensional materials is dangling-bond-free, they are ready to interact with each other by the van der Waals forces, resulting in 2D–0D, 2D–1D, and 2D–3D van der Waals heterojunctions [121,122]. For instance, benefited from the strong and size-tunable light absorption of PbS QDs and the high carrier mobility of the MoS₂ monolayer, a hybrid 2D–0D MoS₂–PbS QD photodetector exhibits excellent responsivity of up to 10^6 A W^{-1} (Fig. 8a) [123]. A self-powered UV/Vis photodetector based on

2D–1D heterojunction photodiode consisting of Se nanotubes and InSe nanosheet demonstrated a high responsivity of the 110 A W^{-1} and a fast response speed of 30 ms (Fig. 8b) [124].

Besides straightforward layer-by-layer integration of the materials with different dimensions, more complicated mixed-dimensional heterojunctions have been developed by design. Sutter group reported the spontaneous formation of a unique wrap-around SnS/SnS₂ core/shell heterostructure via a one-pot vapor transport synthesis [125]. As shown in Fig. 8c, the SnS form a typical layer-by-layer geometry but enclosed in a wrap-around SnS₂ shell. During the growth, the structural mismatch with SnS and sulfur-rich tin chalcogenides forces the formation of a phase-separated, layered SnS₂ shell. Importantly, SnS and SnS₂ create two distinct interfaces, namely parallel and perpendicular, due to the different geometries, resulting in interesting anisotropic electron transfer behaviors. For the parallel interface, carriers have a low transmission probability since they have to traverse the Van der Waals gaps in the layered SnS core. On the other hand, the perpendicular interface possesses a higher transmission probability as the carriers flow along with the individual SnS sheets. In addition, the type-II band alignment provides extended light absorption and reaches into the NIR, making it promising for optoelectronics applications.

For 2D heterojunctions, we can use metals or semimetals like graphene as the electrode and insulators like 2D h-BN as the dielectric layer. Therefore, it is possible to not only construct mixed-dimensional heterojunctions but also to design mixed-dimensional contact at the device level and achieve some unique performance. For many electronic and optoelectronic applications, the channel thickness and gate length are of vital importance. However, for

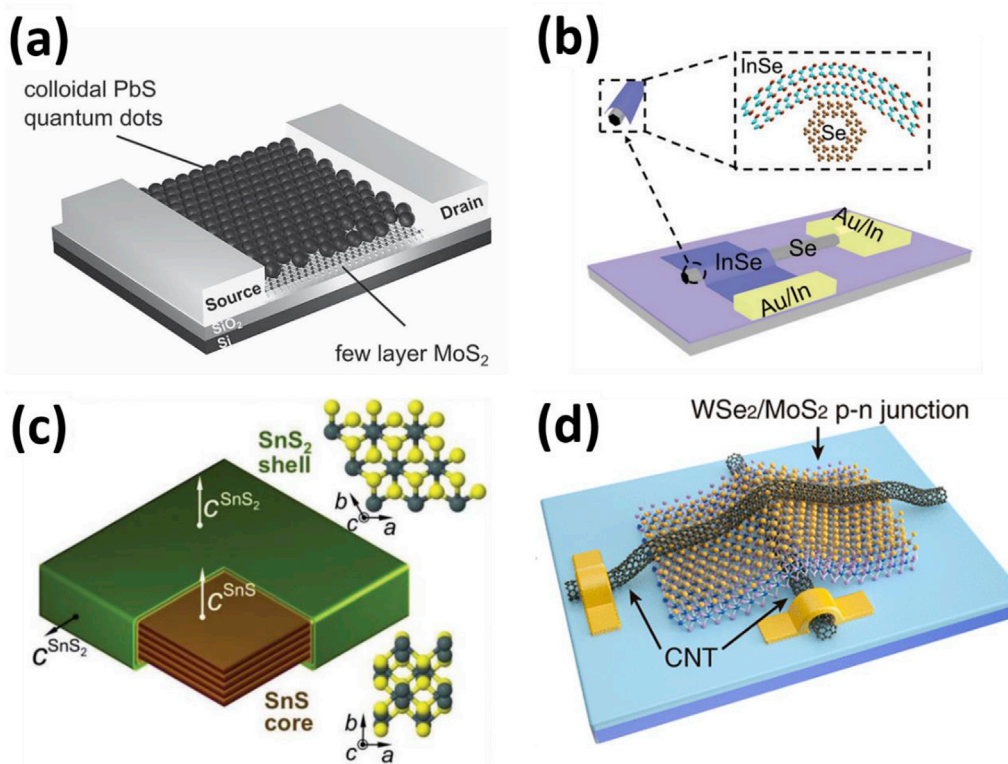


Fig. 8. a) Device schematics of the 2D–0D MoS₂–PbS QD photodetector, which consists of a few-layer MoS₂ nanosheet on top of the Si/SiO₂ substrate with Ti/Au source and drain. The colloidal PbS quantum dot film is overcoating the whole device architecture. Reproduced with permission [123]. Copyright © 2014 WILEY-VCH Verlag GmbH & Co. KGaA, Weinheim. b) Schematic diagram of the Se/InSe p–n heterojunction device. Inset: The atomic structure for the cross-section of the heterojunction. Reproduced with permission [124]. Copyright © 2020 The Royal Society of Chemistry. c) Schematic showing the core/shell structure consisting of a layered SnS core enclosed by a few-layer SnS₂ shell. Insets: Structure models and unit vectors of the hexagonal (SnS₂) and orthorhombic (SnS) lattices. Reproduced with permission [125]. Copyright © 2019 WILEY-VCH Verlag GmbH & Co. KGaA, Weinheim. d) Schematic illustration of the vertical point WSe₂/MoS₂ p–n heterojunction. Reproduced with permission [127]. Copyright © 2020 American Chemical Society.

vertically stacked Van der Waals heterostructures, it remains a challenge to construct nanoscale contact since the in-plane sizes are usually in microscale [126]. To solve this issue, a vertical point junction was designed, in which a 2D WSe₂/MoS₂ type-II heterojunction was sandwiched between two cross-stacked carbon nanotubes, as shown in Fig. 8d [127]. Importantly, the optoelectronic properties can be modulated by the gate voltage, resulting in three different photodetecting modes, mainly attributed to the gate modulated built-in potential in the type-II heterojunction and the Schottky barrier between CNT and WSe₂/MoS₂. Furthermore, the heterostructure exhibits outstanding photovoltaic properties with the photoresponsivity and the external quantum efficiency of 179 mA/W and 42.7%, respectively.

2.6. External fields

Externally applied fields, such as pressure, temperature, electric and magnetic fields, can have great influences on the properties of type-II heterojunction. Given this, many novel optoelectronic devices have been developed to explore the possibility of utilizing the external fields as effective tools to modulate the charge carrier generation, separation, transport, and recombination behaviors.

2.6.1. Stress

As we mentioned in 2.4, the strain engineering is crucial in designing type-II heterojunctions. Yet, the strain at the heterojunction interface is mainly determined by the intrinsic lattice mismatch of the forming semiconductor materials. On the other hand, applying an external stress provides additional modifications on the optoelectronic properties of the type-II heterojunctions. For example, the piezo-phototronic effect, which coupling the semiconducting, optical, and piezoelectric properties, has drawn tremendous interest recently [128–133]. The basic concept of the piezo-phototronic effect relies on the piezopotential at the semiconductor interface introduced by the external stress in piezoelectric semiconductors (such as wurtzite ZnO, GaN, CdS, and transition metal dichalcogenide MoS₂). The piezopotential acts as a “gate” voltage for the modulating the interface band structure and controlling the transport of the charge carriers, hence, optimizes the optoelectronic properties effectively [134,135]. After first demonstrated in the single ZnO nanowire, the piezo-phototronic effect has been soon explored in various heterojunction structures [136–139]. The photodetector is one of the most widely studied applications of type-II heterojunctions employing the piezo-phototronic effect [140–143]. By taking advantage of the piezo-phototronic effect and type-II band configuration, we have developed a UV/visible photodetector based on a fully wide-bandgap ZnO/ZnS core/shell nanowires (Fig. 9a and b) [144]. The broadening of the detection range was attributed to the intra-band transition between the ZnS valence band and the ZnO conduction band, and the enhancement of the photoresponse was due to the band structure modulation caused by the piezopotential under applied stress. Similar to the photodetectors, solar cell efficiency can also be enhanced through the piezo-phototronic effect [145,146]. A simple Si/ZnO heterojunction was fabricated by direct growth of the ZnO nanowire arrays on a serious silicon substrate (Fig. 8c and d). The efficiency was improved significantly due to the beneficial light absorption owing to the nanowire array configuration and the improvement of the charge carrier transport due to the strain-induced piezoelectric polarization [147]. In addition, the piezo-phototronic effect has been applied to developing high-performance LEDs (Fig. 9e and f) [148–152]. More importantly, the unique properties of the piezo-phototronic provide potential approaches for next-generation optoelectronic devices, such as tactile sensor matrix and electronic skins [153].

On the other hand, externally applied pressure can alter the optoelectronic properties of materials by means of tuning their lattice parameters. A unique pressure-induced positive to negative photoconductivity transition was observed in a recent study [154]. The photoconductivity of a WO₃/CuO heterostructure evolves from positive photocurrent (PPC, where the electrical conductivity increases with irradiation), to PPC with PrPPC (positive persistent photoconductivity), and finally to IPC (inverse photoconductivity, where the electrical conductivity decreases with irradiation) with PrIPC (persistent inverse photocurrent), as the external hydrostatic pressure increases. Such a unique feature was mainly attributed to the reduction of the WO₃ bandgap resulted from the WO₆ octahedral distortion under pressure. The p-type WO₃ and n-type CuO formed a heterojunction with a large energy barrier, electron/hole pairs are generated predominantly in CuO under illumination and recombine after laser being switched off. Under the higher pressure, the formation of reduced W^{(6-x)+} color centers started to occur and decreases the energy barrier between CuO and WO₃, making the transformation of electrons and holes possible. In addition, the oxygen vacancies formed at the interface causes the electron trapping and the recombination more difficult, thus, the PrPPC arise with the excess of holes. The bandgap can be further reduced to 0.7–1.0 eV upon further increased pressure, in such case, the transfer of electrons will only occur from CuO to WO₃, causing the inverted photocurrent.

2.6.2. Electric field

For the type-II heterojunction, an external electric field can modulate the polarization of the charge carriers. One of the well-established methods is via the applied gate voltage. For example, MoS₂/WSe₂ van der Waals heterojunctions exhibit gate-tunable rectification characteristics [155]. Due to the absence of lateral transport, the underlying mechanism can be described by Shockley–Read–Hall (SRH) recombination mediated by inelastic tunneling of majority carriers into trap states in the gap and/or Langevin recombination by Coulomb interaction, which is different to those of a conventional p–n junction diode. Additionally, bipolar behavior was observed in the same system (Fig. 10a) [156]. Due to the ambipolar behavior of WSe₂, the heterojunction has either resistive n–n behavior at a positive voltage or p–n junction diode-like rectification behavior at the negative voltage. The device operated under p–n regime demonstrated promising photovoltaics performance.

Interestingly, sometimes it is not necessary to provide an external electric field, the light itself can act as the gate voltage as photogating. If the photo-generated carriers are trapped in the localized states, usually located at defects or the surface of the semiconducting material, they can serve as the gate voltage by producing an additional electric field. This photogating mechanism is of particular importance for nanostructured materials, where the carrier lifetime is greatly prolonged due to the surface-to-volume ratio and reduced screening. Recently, photodetectors based on photogating have gained increasing interest owing to their high responsivity, which is attributed to high photoconductive gain [157]. Tan et al. reported a graphene-contacted WS₂/MoS₂ monolayer heterojunction with a photoresponsivity of up to 2340 A W⁻¹ and an internal photoconductive gain of over 3.7×10^4 [158]. The type-II band alignment ensures the spatial separation of the photoexcited carriers, resulting in the accumulation of electrons in MoS₂ layer and holes in WS₂ layer. Under light illumination and applied bias, the photogenerated electrons and holes drift toward the opposite direction. The electrons were being collected and contributes to the photocurrent, while the holes tend to accumulate due to the trap states. Thus, the holes are acting as a positive gate and lower the Schottky barrier between WS₂ and the graphene

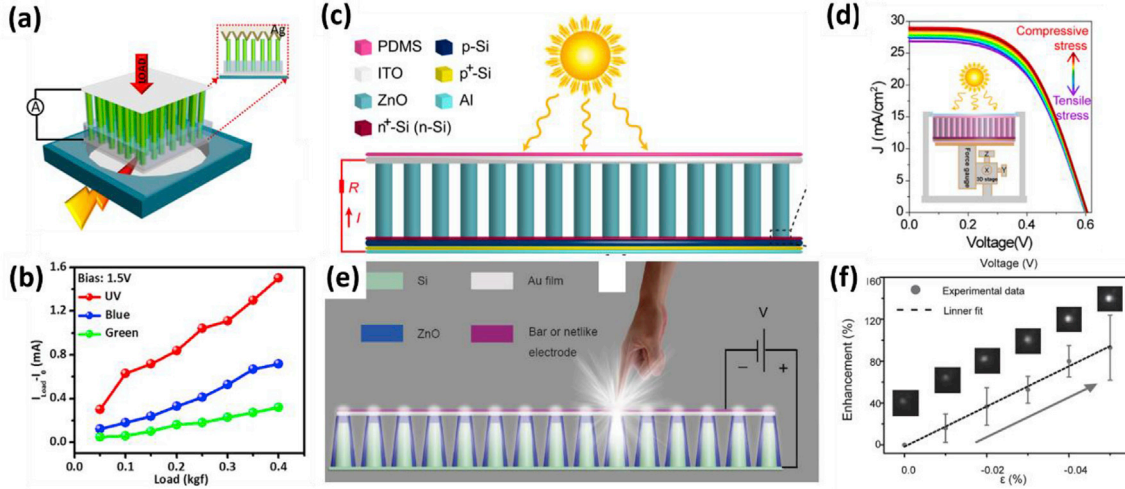


Fig. 9. a) Schematic illustration of the ZnO/ZnS core/shell nanowire photodetector. Inserted is the silver-coated polyester zigzag top electrode. b) Photocurrent response with respect to compressive loads. Reproduced with permission [144]. Copyright © 2015 American Chemical Society. c) Schematic of the ZnO/Si solar cell. d) Vertical pressure dependence of the J–V characteristics. Reproduced with permission [147]. Copyright © 2017 American Chemical Society. e) Schematic demonstration of piezo-phototronic effect enhanced light emissions of ZnO-nanofilm/Si-micropillar heterostructure LED arrays under strain. f) Enhancement factor E of the LED intensity versus strains ϵ , together with the corresponding images of light emissions. Reproduced with permission [148]. Copyright © 2015 WILEY-VCH Verlag GmbH & Co. KGaA, Weinheim.

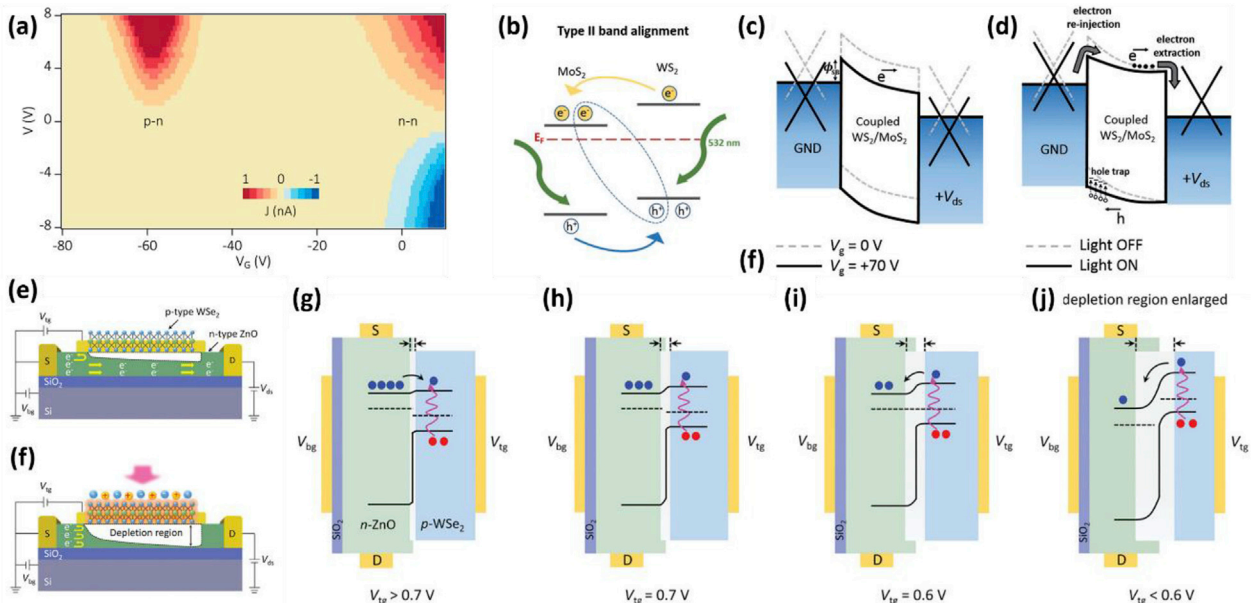


Fig. 10. a) Current map of MoS₂/WSe₂ heterojunction. At $V_G > -10 \text{ V}$, both flakes are n-type and the device shows resistive behavior. In the range of $-71 \text{ V} < V_G < -47 \text{ V}$, the electrical characteristic exhibits a p–n diode-like behavior. Reproduced with permission [156]. Copyright © 2014 American Chemical Society. b–d) Band schematic of a vertically stacked WS₂/MoS₂ heterostructure without potential and light irradiation while applying positive back-gate potential, under light irradiation, respectively. Reproduced with permission [158]. Copyright © 2017 WILEY-VCH Verlag GmbH & Co. KGaA, Weinheim. e,f) Schematics of the cross-section of the light-driven WSe₂/ZnO junction field-effect transistor without and with light illumination, respectively. g–j) The energy band diagrams at the junction with illumination at different top-gate voltage. The blue and red dots represent the electrons and holes, respectively. Reproduced with permission [161]. Copyright © 2019 WILEY-VCH Verlag GmbH & Co. KGaA, Weinheim.

electrode. The lowered Schottky barrier, in turn, facilitates the re-injection of electrons, leading to the significantly large photoconductive gain (Fig. 10b–d). Different from the hole trapping mechanism, Tsai et al. designed a “hole puddle” strategy to improve the response time [159]. In their design, the WSe₂ nanodots were embedded in the WS₂ matrix via sequential oxidation and CVD regrowth, creating massive WSe₂/WS₂ heterojunctions. In turn, the charge separation is achieved by the fast interlayer electron transfer and excitonic dynamics, which offers a significantly faster temporal response than the aforementioned result, in which the long-lived

trap state dominates the process of electron/hole recombination.

Though great efforts have been devoted to improving the optical gain, the common problem of the trap-assisted gain mechanism is the slow response time because both key parameters are closely involved with the carrier lifetime [160]. In order to solve this issue, Guo et al. designed a light-driven WSe₂/ZnO junction field-effect transistor in aim to break inherent gain–response time tradeoff [161]. In their design, a distinct gain mechanism from photogating is proposed. In the dark, the high resistance of WSe₂ weakens the effect of top-gate voltage and creates a depletion region within the

ZnO channel (Fig. 10e,h). Under light illumination, the photocarriers excited in WSe₂ will reduce the resistance of WSe₂ and generate an effective conductive path for the top-gate voltage to control the depletion region in ZnO. If a negative gate voltage is applied, the conductive path will result in the enlarged depletion region and a dramatic increase in the channel resistance. On the other hand, a positive gate voltage will cause the channel resistance decreasing as the depletion region shrinks. Overall, in this unique architecture, WSe₂ is acting as a light-driven switch to control the extent of the field-effect modulation on ZnO channel conductance. Therefore, the gain and response time have been successfully decoupled, as the gain is modulated by the field effect, and the response time is determined by the switching speed of the switch layer WSe₂. In addition, the device exhibits photocurrent polarity due to the type-II band alignment (Fig. 10g–i). As a result, this device has demonstrated excellent performance, such as a high responsivity of $4.83 \times 10^3 \text{ A W}^{-1}$ with a gain of $\approx 10^4$ and a rapid response time of $\approx 10 \mu\text{s}$ simultaneously.

With the appealing property of spontaneous electric polarization, ferroelectric materials have been widely used in electronic and optoelectronic devices [162–165]. The key advantage of coupling ferroelectric materials with type-II heterojunction is the remnant built-in potential created by the external electric field, which can be utilized as a means to tune the carrier transport properties at the interface. For example, Li et al. reported a ferroelectric V-doped ZnO nanosheets/p-Si heterojunction photodetector [166]. The interface energy band along with the generation, separation, and transportation of the photogenerated electron/hole pairs can be effectively modulated, resulting in a large enhancement in photoresponse in contrast with the non-ferroelectric ZnO/Si PD (Fig. 11a).

2.6.3. Magnetic fields

The magnetic fields can also affect heterojunction performance. Our group has investigated the coupling effect of magnetic fields on piezotronic and piezophototronic properties of ZnO and ZnO/Co₃O₄ core/shell nanowire arrays [167]. With the existence of the external magnetic fields, a portion of electrons migrated to the surface of nanowire due to the Lorentz force, which has a negative effect on the conductivity of nanowire. On the other hand, the magnetic field facilitates the separation and mitigates the recombination of photoinduced electron/hole pairs, which offer a positive effect. The trade-off of those two effects results in the opposite response of the photocurrent with and without magnetic fields applied (Fig. 11b).

2.6.4. Temperature

Temperature is another important factor which affects the properties of the heterojunctions. In this regard, the pyroelectric effect, which results from the temperature-induced spontaneous polarization in certain anisotropic materials, has been demonstrated as an efficient strategy to modulate the carrier transfer behaviors [168]. A novel concept, pyro-phototronic, which combines the pyroelectric effect, photonic excitations, and semiconductor properties, has drawn tremendous interest recently [169–173]. For example, the performance of a P3HT/ZnO nanowire array solar cells has been largely enhanced by applying an external cooling temperature variation [174]. Alternatively, by utilizing the light-self-induced pyro-phototronic effect, both response time and responsivity have been improved dramatically for a UV photodetector based on p-Si/n-ZnO type-II heterojunction without external heating or cooling source [175]. Interestingly, by combining the pyroelectric characteristic of ZnO and the thermoelectric characteristic of SnS, a unique light wavelength-induced photocurrent polarity was observed in the ZnO/SnS heterojunctions [176]. The deposited SnS layer is partially transparent to visible light

illumination but opaque to UV light illumination. Therefore, under visible light illumination, the temperature gradient inside ZnO creates a distribution of polarization charges with localized positive charges at the heterojunction interface and negative charges at the Ag electrode side. In this case, the electrons would flow in the external circuit from the Ag electrode to the ITO electrode. When the light illumination is turned off, the photovoltaic current rapidly disappears and the gradually decreased temperature causes a negative pyroelectric current. On the other hand, the UV light illumination only causes the temperature gradient inside the SnS. The inner thermo-potential of SnS suppressed the transport of holes toward the ITO electrode, thus resulting in resulting in electron flow in the external circuit from the ITO electrode to the Ag electrode (Fig. 11c–f). In addition, differently from conventional devices, which exhibit inferior performance under low temperatures, the temperature-dependence nature of the pyro-phototronic effect provides a promising approach for many cryogenic environment applications [177,178]. Alternatively, Zhang et al. designed another type of temperature enhanced solar cell by combining the photovoltaic and thermoelectric effects [179]. The thermophototronic effect enhanced solar cell was fabricated based on InP/ZnO nanorod heterojunction. In their design, an inner thermopotential was generated by applying a cooling operation on the InP, leading to the facilitated hole transport in the InP, as well as the modulation of the band alignment at the interface, which helps the release of trapped electrons (Fig. 11g and h). As a result, the output current and voltage under light illumination were enhanced by 27.3% and 76%, respectively.

3. Synthetic strategies for Type-II nano-heterojunction

Obtain a high-quality interface is a prerequisite in order to efficiently engineer the distinguished interface effect of type-II nano-heterojunction and enhance the device performance. Over the last decades, numerous methods have been developed to fabricate nano-heterojunctions. Instead of listing each synthesis technique, we delineate the generic methodologies for the fabrication of type-II nano-heterojunction in this section. Therefore, we here summarized and classified the fabrication methods into several categories based on the strategical perspective. While our emphasis is on type-II nano-heterojunction, some other nanoscale junctions will also be reviewed and discussed to have a broader view. We hope this can provide a cognitive framework and effectively help future research to improve existing production methods or develop new methods.

3.1. Solution-phase growth

Besides the one-step direct synthesis method, which is not feasible for the fabrication of some complex structures, the multi-step synthesis method is being exploited. One of the most extensively explored approaches is to combine the initial growth of one semiconductor and the secondary growth of another with the former essentially served as the substrate for the latter. Therefore, a much wider range of material combinations and structures can be achieved. Similar to the direct synthesis approach, secondary growth can be achieved by both solution-phase and vapor-phase methods.

For 0D nanocrystals, the solution-phase methods are often to be used for the construction of epitaxial heterostructures. For the synthesis of the shell materials, several approaches have been reported such as hot-injection, successive ion layer adsorption and reaction (SILAR), and solvothermal/hydrothermal method. In a typical route, the existing nanoparticles are serving as the “seeds” and providing nucleation sites for the second material to be grown.

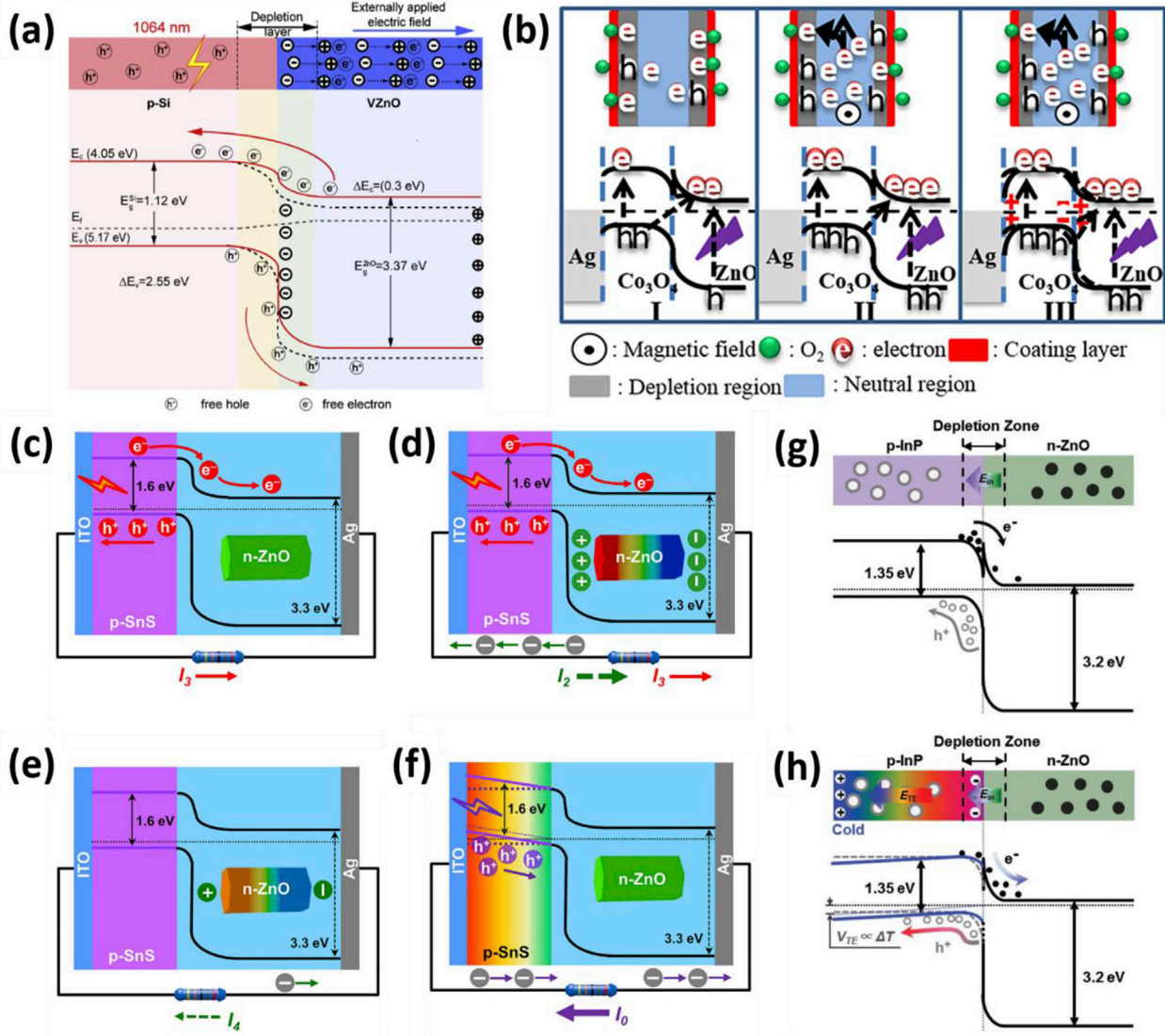


Fig. 11. a) V-doped ZnO nanosheets/p-Si heterojunction photodetector. The red line is under a forward bias of +1 V, and the black dotted line is under 0 bias. Reproduced with permission [166]. Copyright © 2019 Elsevier Ltd. b) Schematics of energy bands alignment and electron movement of ZnO/Co₃O₄ heterojunction under magnetic field directed perpendicularly out of the paper. Reproduced with permission [167]. Copyright © 2018 American Chemical Society. c-f) Energy-band diagram of the ZnO/SnS heterojunction with light illumination, upon visible light illumination, when turning off the visible light illumination, and upon UV illumination, respectively. Reprinted under the CC BY-NC-ND 4.0 license [176]. Copyright © 2018 Bangsen Ouyang et al. g,h) Energy band diagram of the InP/ZnO heterojunction solar cell in absence of temperature gradient, and after applying a temperature gradient, respectively. Reproduced with permission [179]. Copyright © 2017 WILEY-VCH Verlag GmbH & Co. KGaA, Weinheim.

The energy required for heteronucleation is considerably lower than that for homonucleation, resulting in the favorable suppressing of the homogeneous nucleation during the shell growth process [180]. Besides the reaction temperature, precursor and ligand concentrations, lattice mismatch is another important parameter to be taken into account since the interfacial strain plays a crucial role in determining the nucleation energy as well [14].

The solution-phase method has shown promising in the synthesis of other heterojunctions as well due to its low-cost, easy operability, and high yield. For example, a dense and uniform CdTe shell with a zinc-blende phase was deposited on the wurtzite ZnO nanorod core by an electrochemical deposition method [181]. The shell thickness can be tuned by adjusting the total charge quantity. On the other hand, the layer-by-layer precise control of the shell thickness can be achieved using the SILAR method, where the cationic and anionic precursors are injected alternatively, thus only half of a monolayer was deposited at a time. Using this method, a

3D-branched ZnO/CdS nanowire arrays were fabricated and demonstrated promising performance for solar water splitting [182].

3.2. Vapor-phase growth

As compared with the solution-phase methods, vapor-phase methods generally offer higher crystalline quality and better epitaxial growth at the interface [183]. Among different vapor-phase methods, the chemical vapor deposition (CVD) has been extensively explored for creating nano-heterojunction materials. It should be noted that in nanomaterial fabrication, the CVD reaction was routinely carried out in the tube furnace setup, which shares a lot of similarities with the thermal evaporation method in terms of the experimental procedures. Therefore, in this review, we do not distinguish CVD and thermal evaporation methods, or a broad concept of vapor transport/growth, which are often used

interchangeably in different publications. Taking the well-studied II–VI semiconductor as the example, Myvng et al. reported the synthesis of wurtzite/wurtzite ZnO/CdS_xSe_{1-x} core/shell nanowire arrays with full range tunable shell composition by adjusting the $CdS/CdSe$ precursor ratio and the controllable thickness over deposition temperature or time [184]. Whilst a completely different nanotree-like morphology was reported by slightly adjusting the reaction parameters [185]. Moreover, changing the precursor into $ZnSe/CdSe$ mixed powder resulting in the forming of wurtzite/zinc-blende $ZnO/Zn_xCd_{1-x}Se$ heterojunctions [186]. The polytypic structure, namely double-shell structure, superlattice structure, and twinned superlattice structures can be created by tuning the composition of the mixed precursor. The same structure can also be archived by using Zn, Cd, and Se mixed powder instead [187]. On the contrary, a wurtzite/amorphous ZnO/ZnS_xSe_{1-x} core/shell nanowire arrays were reported by another group [188]. Using the same method, More complex compositions and structures, such as $ZnO/Zn_xCd_{1-x}Se_yTe_{1-y}$ core/shell and $ZnO/ZnS_xSe_{1-x}/ZnSe$ double-shelled heterostructures can be easily obtained [189,190]. Those reports clearly indicated rich variability of deposition parameters and the great controllability on the composition, morphology, and crystallinity of the CVD method. It is challenging for the one-step synthesis of nanoscale heterojunction by the vapor-phase methods. Nevertheless, such an issue can be addressed by changing the growth condition during the growth progress [191]. For example, Pan group developed a simple and effective source switchable vapor growth strategy. By using a step motor to precisely control the position of the source materials, 1D axial heterojunctions, such as CdS/CdS_xSe_{1-x} and $CdS/CdSSe/CdS$ have been successfully synthesized [192,193].

For many applications, it is desirable to assemble the heterojunction building block horizontally for better integration into the mainstream planar architecture [194]. In most cases, it is realized by the several post-growth processes, involving the collection, transformation, and rearrangement of the pre-synthesized materials [195–197]. Alternatively, guided growth of horizontally aligned nanowires provides advantages by combining synthesis and assembly in a single step, thus, allowing precise control of the location, orientation, and layout [198]. Via a vapor–liquid–solid (VLS) growth, the guided growth of horizontally aligned heterojunctions, such as $ZnSe@ZnTe$ core/shell nanowires and $CdS/CdSe$ core/shell nanowalls [199,200], were demonstrated. Interestingly, giving the formation of the shell was largely determined by the core behavior, the crystal phase, either wurtzite or zinc blende, and crystallographic orientations of both can be well controlled by the substrate selections and the growth conditions.

The advantages of compositional control and large-scale synthesis have made the metalorganic chemical vapor deposition (MOCVD) an emerging technique for the fabrication of semiconductor materials and heterojunctions for electronic and optoelectronic applications [201,202]. Based on the mature commercial use of MOCVD technology for the production of compound semiconductors, a variety of heterojunctions have been synthesized so far, such as CdS/ZnS [203,204], $ZnSe/ZnCdSe$ [205], $ZnO/Cu₂O$ [206], ZnO/ZnS [207], $ZnO/ZnSe$ [208], and SnS/MoS_2 [209]. As a variant of CVD, it is more commonly adopting the name to be metalorganic vapor phase epitaxy (MOVPE), which emphasizes its high-quality epitaxial nature [210]. In comparison to conventional CVD, MOCVD provides improved control over nucleation and uniform growth by using vapor-phase precursors [211]. In addition, the continuous development of the MOCVD precursors chemistry has made great progress in reducing the thermal budget needed for integration in optoelectronics [212].

After first developed in the early 1970s, atomic layer deposition (ALD) has gained recognition as one of the sophisticated in precise

control of material deposition at the atomic level [213,214]. It distinguishes from CVD with the characteristic feature of alternate supply of precursors in a cyclic manner, leading to a layer-by-layer growth and accurate thickness control [215]. The saturative surface reaction in each cycle allows the deposition to be self-limiting, ensuring excellent conformality on high aspect structures [216,217]. Compared to other deposition methods, ALD has demonstrated a particular advantage in creating uniform coatings on certain complex structures, for instance, anodic aluminum oxide (AAO) template and 3D opal template [218–225]. Besides the coating of the active materials, another distinct characteristic of ALD in constructing high-performance heterojunction is its capability to deposit uniform and sub-nanometer-thickness interfacial layer. To prevent the excess charge recombination origins from large surface area and poor-quality interface caused inefficient charge carrier separation, it is sometimes necessary to introduce an extra ultrathin interfacial inorganic layer, such as Al_2O_3 [226,227], TiO_2 [228–231], and ZnS [232], which acting as passivation of surface defect sites, or as a tunneling barrier for electron/hole recombination, or to build a surface dipole and modulate the distribution of charge across the interface [233,234].

Compared to CVD, physical vapor deposition (PVD), which rely on the vaporization, either thermodynamically (evaporation and ablation), or by the bombardment with energetic ions (sputtering), and later deposition of the precursor materials, provides a straightforward alternative with large-scale fabrication capability and has been widely used in creating functional interfaces for microelectronic and optoelectronic applications [235–237]. However, it often suffers from the inferior interface properties due to the amorphous or polycrystalline nature of the deposited materials [238]. In addition, as a so-called line-of-sight deposition technology, the shadowing effects of PVD, especially the sputtering method, often cause an inherent poor coverage of the deposited material. Therefore, it is more suitable for the planar thin-film configuration [239–242]. Nevertheless, a few attempts have been made to adapt conventional PVD methods in constructing nanoscale heterostructures, it usually requires multiple steps combining several other techniques. For example, Guo et al. developed a MoS_2 nanoflakes/ TiO_2 nanocavity arrays heterostructure by a combined PVD and CVD strategy [243].

The pulsed laser deposition (PLD) method is yet another promising approach in the synthesis of heterostructures. As a physical vapor deposition method, PLD holds many advantages for nanoscale heterojunction synthesis: (1) with the energy source being outside the vacuum chamber, it provides a much greater degree of flexibility in materials use and geometrical arrangements; (2) the growth rate can be well controlled giving by the pulsed nature of the energy source; (3) the precise stoichiometry transfer can be archived by deliberately controlling the growth conditions [244–246]. Because of those distinct advantages, many pioneer works focused on the growth of axial nanowire heterojunctions using the PLD method by periodically changing the reactants [247,248]. Alternatively, the core/shell construction can form in a two-step reaction by using the pre-synthesized nanostructures as the templates [249–252]. Over the last years, our group has developed various group II–VI core/shell nanowire heterojunctions including $ZnO/ZnSe$, ZnO/ZnS , $CdSe/ZnTe$, and $CdSe/CdTe$ [12,105,107,144,253–255]. This typically involves a two-step technique combining thermal evaporation or CVD for the synthesis of the core, followed by the PLD that gives rise to the formation of the shell material. One particular advantage of PLD is its capability in forming an epitaxial interface between highly lattice-mismatched semiconductor combinations, thus, offers more electronic structure tunability and better material stability. For instance, the large lattice mismatch of 8.8% between wurtzite ZnO and zinc blende

ZnSe, and an even larger one of 25% between wurtzite ZnO and wurtzite ZnSe usually results in inferior interface quality. Nevertheless, epitaxial growth of ZnSe from the ZnO core is confirmed by the abrupt interface with no transitional layer, as shown in the TEM images in Fig. 12a–d and the epitaxial relationship has been identified as $[0001]_{\text{ZnO}}/\!/ [001]_{\text{ZnSe}}$ and $(\bar{2}\bar{1}10)_{\text{ZnO}}/\!/ (011)_{\text{ZnSe}}$ [12]. Interestingly, the lattice mismatch extent plays a crucial role in determining the crystal structure of the shell being deposited. Only the zinc blende phase can be growth in ZnO/ZnSe and ZnO/ZnS combinations. On the contrary, in the case of CdSe/ZnTe, even ZnTe is thermodynamically stable in a cubic zinc blende structure, a wurtzite CdSe and wurtzite ZnTe interface were formed, mainly attributed to the small lattice mismatch of $\sim 0.08\%$ (Fig. 12e and f). Since the crystalline structure is crucially important to modulate the electronic and optoelectronic properties, it provides another feasible approach to engineering the bandgap structure. Using the same method, several other combinations, such as ZnO/CdS and ZnO/ZnTe, have also been demonstrated [256,257]. PLD technique has also shown great promising in the fabrication of 2D-based heterojunctions. Lu et al. reported a unique vertical n–n heterojunction structure based on 2D MoTe₂ and 3D Si [258]. Highly uniform few-layer MoTe₂ were deposited on Si substrate by the PLD method, which in situ forming a MoTe₂/Si heterojunction.

3.3. Ion exchange

Up to now, significant achievements have been attained in

producing various types of nanoscale heterojunctions by either the direct synthesis or the secondary growth approaches. However, the strict requirements on the lattice mismatch and the overgrowth layer thickness of the deposited materials and the pre-existing materials exceedingly limited the viable methods for the epitaxy growth of high-quality nano-heterojunctions [259]. As an alternative to the conventional synthesis method, the chemical transformation of existing nanostructures into another provides another efficient approach for the synthesis of nanostructured materials with precise control over the chemical compositions, structures, and morphologies [260]. In this section, we will focus on the ion exchange method (cation exchange and anion exchange). Instead of direct deposition or growth of the targeted materials on the pre-existing materials, the ion exchange replies on the replacement of the pristine ions with guest ions, resulting in the chemical conversion of one material into another. In comparison with the conventional epitaxy growth method with outward growth direction, the ion exchange process can be less regulated by the lattice parameters of the seed substrate due to its unique inward growth mechanism. One distinct advantage of the ion exchange method concerned in this review is its capability to create interfaces or heterojunctions within the nanostructured materials via the partial transformation [261]. In addition, unlike the conventional synthesis method, which usually leads to the thermodynamically stable states, the ion exchange strategy enables the forming of metastable or nonequilibrium nanostructures by thermodynamics and kinetical control [262].

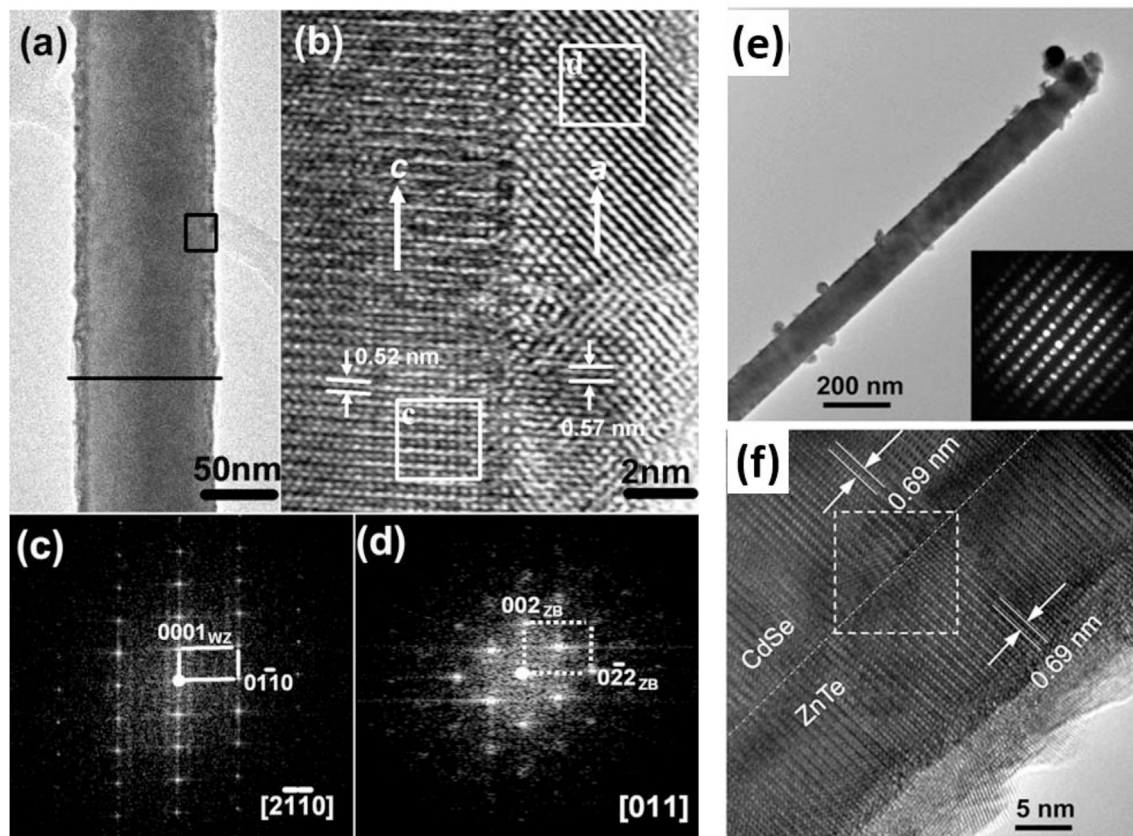


Fig. 12. a) Low-magnification TEM image of a ZnO/ZnSe core/shell nanowire. A thin layer of ZnSe was coated on the ZnO nanowire. b) High-resolution TEM image of the interface of the core/shell heterostructure, enlarged from the rectangular area outlined in (a), showing the epitaxial growth relationship of the ZnO WZ core and ZnSe ZB shell. c,d) FFT patterns of the rectangular areas outlined in (b). Reproduced with permission [12]. Copyright © 2008 WILEY-VCH Verlag GmbH & Co. KGaA, Weinheim. (e) A representative TEM image of an individual CdSe/ZnTe core/shell nanowire. Inset: the corresponding CBED pattern. (f) HRTEM images of the core/shell interface that display the interplanar spacing and epitaxial growth of the WZ ZnTe shell on the WZ CdSe core. Reproduced with permission [105]. Copyright © 2014 The Royal Society of Chemistry.

For most semiconductor materials, the anions are serving as the structural frame and the cations are relatively mobile in the crystal lattice. Therefore, the chemical transformation through cation exchange is relatively easy to achieve. During a cation exchange, the overall morphology of the nanostructure can be well preserved since the anion network distortion is generally negligible. The rapid development of cation exchange has largely expanded the synthetic versatility for creating the nano-heterojunctions which is otherwise difficult or impossible to be realized. For example, using sequential cation exchange reactions guided by the interfacial reactivity and crystal structure relations, an incredible synthetical strategy for heterostructured nanorod has been developed, providing feasible pathways to synthesize as many as 65,520 distinct multicomponent metal sulfide nanorods [263]. The ability of the cation exchange method to synthesize type-II heterojunction for optoelectronic devices has been demonstrated as early as 1954 in a Cu₂S/CdS thin-film solar cell [264]. Over the last years, many

type-II nano-heterojunctions have been developed using the cation exchange method, mainly encompassing the II–VI, IV–VI semiconductors. Among them, cadmium chalcogenide/copper chalcogenide is the most studied binary system for optoelectronics [265–270]. For example, Yang group developed a facile cation exchange method and fabricated core/shell CdS/Cu₂S solar cells based on single nanowire and nanorod arrays, as shown in Fig. 13a–c [266,267]. Importantly, the overall architecture and composition distribution of the heterostructures are determined by the lattice mismatch and the associated strain at the interface. For instance, Xiong et al. investigated the CdS/Cu₂S nanowire system and observed an interesting transformation from a core/shell structure into superlattice by simply increasing the reaction time (Fig. 13d) [268]. In addition, ligands play a crucial role in the cation exchange process. Dogen et al. developed an efficient technique to synthesize well-defined lateral epitaxial CdSe/Cu₂Se heterojunctions in single nanowires by using the electron-beam as the mask (Fig. 13e–i)

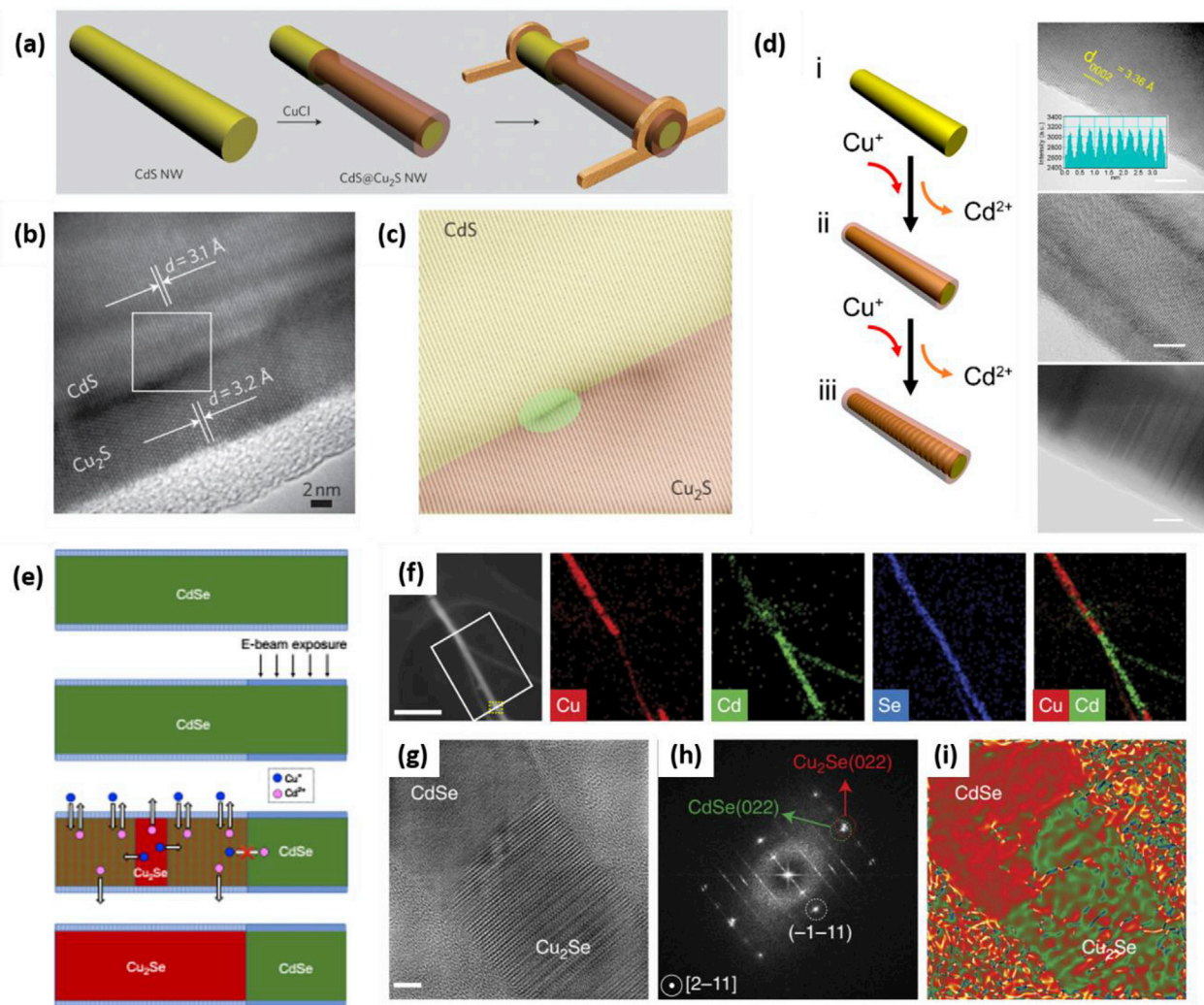


Fig. 13. a) Schematic of the CdS/Cu₂S core/shell nanowire solar cell fabrication process by cation exchange. From left to right, a CdS (yellow) nanowire (NW) is partially converted in CuCl solution to form a layer of Cu₂S (brown) shell, then metal contacts were deposited on the CdS core and Cu₂S shell. b) High-resolution TEM image of a CdS/Cu₂S nanowire at the heterojunction. c) Constructed inverse FFT image along the growth direction for the area marked in b. The green area shows the typical lattice fringe distortion at the core/shell interface. Reproduced with permission [266]. Copyright © 2011 Macmillan Publishers Limited. d) Schematic diagram and the corresponding TEM images of phase evolution from pristine CdS nanowire to CdS/Cu₂S core/shell nanowire, and eventually to CdS/Cu₂S superlattice nanowire. Inset: transmitted electron intensity profile along the periodic spacing denoted by the yellow line, which is consistent with the lattice distance (~3.36 Å) of the wurtzite phase CdS (0002) plane. Reproduced with permission [268]. Copyright © 2017 American Chemical Society. e) Illustration of the masked cation exchange process in single CdSe nanowires. f) HAADF-STEM image, and the corresponding STEM-EDS elemental maps, of a heterojunction CdSe/Cu₂Se nanowire. The white box indicates the region that was exposed to e-beam irradiation. g,h) HRTEM image and corresponding FFT of the CdSe/Cu₂Se interface, showing the epitaxial relationship between CdSe and Cu₂Se. i) Mean dilation map calculated from the GPA analysis of the HRTEM image. Reprinted under the CC-BY-NC-ND 4.0 license [269]. Copyright © 2018 Sedat Dogan et al.

[269]. Prior to the reaction, a part of the CdSe nanowire was exposed with an electron-beam lithography system, resulting in the cross-linked molecules on the surface of the nanowire. Therefore, the cation exchange between Cd^{2+} and Cu^+ would only occur on the section of the nanowire without being exposed.

To date, the vast majority of the cation exchange studies have been focused on the solution-phase process for nanocrystals/nanorods with a low aspect ratio. However, the extremely fast reaction rates, along with the direction limitation for the lattice stress release, makes the precise control over phases, morphologies, and compositions for nanowires with high aspect ratio difficult [260,271]. To solve this issue, a gas-phase cation exchange process has been developed and utilized for the synthesis of several II–VI semiconductor heterojunctions, such as $\text{ZnCdTe}/\text{CdTe}$ and CdS/ZnCdS [271–273].

On the other hand, due to the low mobility and large ion, the anion exchange reaction is considerably more challenging than the cation exchange reaction. In addition, the materials often suffer morphological changes due to the transformation of the crystal frame [274]. Most of the reported anion exchange is based on the sulfurization or selenidation of oxides, which forces the sulfides or selenides to adopt the wurtzite structure from the pre-existent oxides [275]. Moreover, it is suggested to perform anion exchange reaction under the gas-phase condition at high temperature to provide sufficient thermal energy, especially for larger nanostructures [276]. Similar to the cation exchange, the core/shell heterojunction can be accomplished using partially anion exchange as well [277,278]. In some cases, the cation and anion exchange methods can be used in sequence for better control over the chemical compositions. Xu et al. reported a two-step anion-cation exchange method to fabricate the $\text{ZnO}/\text{Zn}_x\text{Cd}_{1-x}\text{Se}$ nanocables [279]. In this method, the more stable ZnSe layer was first formed by the anion exchange from ZnO nanowires and further converted into CdSe by the cation exchange.

4. Emerging applications

Owing to their unique properties and advanced synthesis methods, type-II nano-heterojunctions have been extensively studied in various optoelectronics applications. Aiming to construction high-performance optoelectronic devices, type-II heterojunction possesses two major advantages. Firstly, the staggered band alignment facilitates carrier separation and confinement in different spatial domains, making it especially suitable for photovoltaics and photodetection applications. Secondly, the interband transitions between two semiconductor materials can occur at a tunable bandgap lower than either of them, thus greatly expand the operational wavelengths. There have been considerable reviews dedicated to the specific applications of nano-heterojunctions in solar cells, photodetectors, and LEDs [16,87,280–283]. Herein, we focus on some novel optoelectronic applications of type-II nano-heterojunctions.

4.1. Photonic memory

The exponential growth in the demand for data storage and processing in the modern big-data era has urged the development of high-performance storage technologies. However, the traditional scaling down strategy for electric-driven memories will soon hit its limits of the von Neumann bottleneck and the ending of Moore's law [284]. To this end, the search for next-generation memory techniques is highly needed. The emerging photonic memories offer great opportunities for optical sensing, image capturing, and photonic neuromorphic computing, owing to the merits of fast access speed, low energy consumption, on-chip integration, large variation margin, and multilevel data storage [285]. Utilizing the

heterojunction structure, the intra-band and inter-band absorption can be induced by different optical wavelength, thus, the information can be converted from light into electrical signals directly. Hu et al. designed a phosphorene/ZnO nanoparticles based type-II heterojunction photonic resistive random access memory (RRAM), as shown in Fig. 14a–c [286]. The broadband response from UV to near-infrared, as well as the light-tunable SET voltage based on both intensity and wavelength, were demonstrated. Upon light illumination, the internal build-in electrical field of the type-II heterojunctions helps the fast electron/hole separation generated by the photovoltaic effect. Subsequently, the trapped carriers can effectively manipulate the formation/destruction process of oxygen vacancy filament by the photogating effect. In addition, the heterojunctions exhibit excellent stability by steadily pinning of the spontaneously delocalized lone-pair electrons to ZnO via the favorable band offset and prevent the phosphorene from being oxidized with ambient oxygen and water molecules.

Generally, resistive switching behavior can be divided into two modes: nonvolatile memory switching, in which the resistive states can be maintained after removing the external voltage, and volatile threshold switching, where the switch from a low resistive state to a high resistive state occurs with applied voltage below a certain value [287]. Due to its unique characteristic, the latter mode has shown great potential in versatile applications such as selectors, steep subthreshold slope transistors, true random number generator, and artificial synapses [288]. It has been reported that those two mechanisms can exist in a single device and convert between each other with appropriate external stimulations. Wang et al. reported a light modulation strategy achieving such conversion for the first time [289]. The memristor device is constructed by sandwiching InP/ZnS QDs between Ag and ITO crossbar array architecture. In this configuration, the switching between high resistance state (HRS) and low resistance state (LRS) is determined by the formation/annihilation process of Ag filament. In dark conditions, the LRS can be maintained since the formed Ag conducting filaments is considered robust. However, under UV illumination, the quasi-type-II band alignment of core/shell InP/ZnS QDs ensures the localizing of photogenerated electrons in InP core and holes in the ZnS shell. The accumulated holes tend to transfer easily between Ag and QDs, resulting in a faster Ag filament dissolution process, corresponding to volatile threshold switching characteristics. Furthermore, a reconfigurable 9×9 visual data storage arrays were constructed and demonstrated the potential in simulation visual neuronal behaviors such as threshold spike, strength modulated spike frequency property, and all-or-nothing spiking.

4.2. Photonic synapses

Recently, driven by the rapidly increasing demand for artificial intelligence, neuromorphic computing has emerged as an exciting research area. To this end, simulation of the synapses, the basic unit of the brain, is of great significance. In particular, photonic synapses, where the synapses were modulated by optical signals, holds additional advantages compared to electrical-modulated conventional synapses, such as ultrahigh propagation speed, high bandwidth, low crosstalk, as well as a noncontact writing method [290]. However, it remains challenging to develop a synapses system with energy efficiency, space efficiency, and the connectivity of a biological brain. In this regard, the heterojunction provides a broadband absorption ranging from the UV to infrared band, thus allowing a broadband phototunable synaptic plasticity. Kumar et al. demonstrated a highly transparent photonic artificial synapse based on $\text{In}_2\text{O}_3/\text{ZnO}$ heterojunction [291]. The device exhibits the typical synaptic characteristics such as short-term plasticity (STP), long-term plasticity (LTP), and paired-pulse facilitation (PPF)

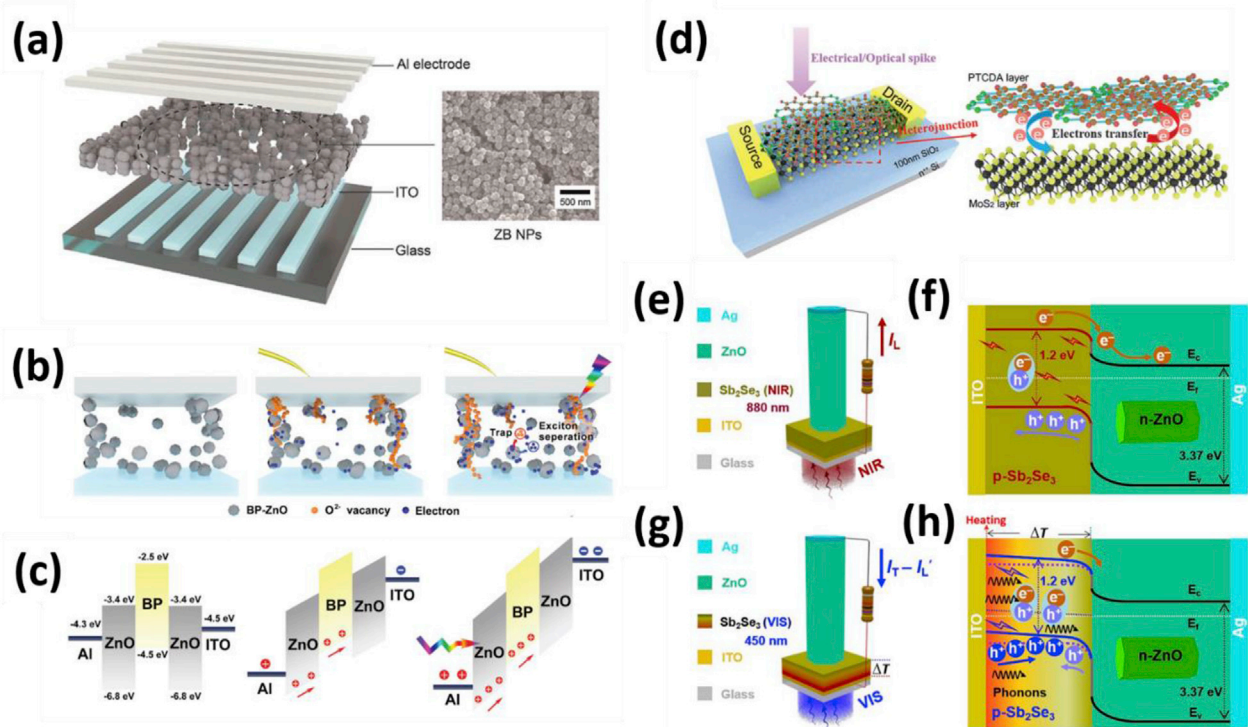


Fig. 14. a) Schematic of Phosphorene/ZnO heterojunction broadband photonic nonvolatile memory. The inset image is a top-viewed SEM image of Phosphorene/ZnO nanoparticle film. b) Illustration of resistive switching at initial state SET process for dark, and SET process under illumination, respectively. c) Band alignment of the device at the initial state, with an application of external bias for dark, and with an application of external bias for illumination, respectively. Reproduced with permission [286]. Copyright © 2018 WILEY-VCH Verlag GmbH & Co. KGaA, Weinheim. d) Schematic of the MoS₂/PTCDA hybrid heterojunction modulated by electrical or optical spike, the right corresponds to a partially enlarged view of the hybrid heterojunction in the red frame, in which the upper is the PTCDA layer and the lower is the MoS₂ layer. Electron transfer at the interface of MoS₂/PTCDA hybrid heterojunction leads to corresponding STP and LTP synaptic behaviors. Reproduced with permission [292]. Copyright © 2018 WILEY-VCH Verlag GmbH & Co. KGaA, Weinheim. e,g) Schematic working state and f,h) Energy band diagram of ZnO/Sb₂Se₃ heterojunction photodetector under 880 and 450 nm light illumination, respectively. Reproduced with permission [295]. Copyright © 2019 Elsevier Ltd.

attributed to the type-II band alignment between ZnO and In₂O₃. Under light illumination and applied electric field, the photo-generated electrons drift toward In₂O₃ and holes towards ZnO. After the UV is switched off, electrons and holes were still being trapped near ZnO and In₂O₃ layer, respectively, resulting in a lower current compared to the initial value. These trapped charges can be enhanced by higher light intensity and erased by a negative bias, known as the photonic potentiation and electric habituation effect. Wang et al. developed a MoS₂/perylene-3,4,9,10-tetracarboxylic dianhydride (PTCDA) heterojunction synapse, realizing electric and optical dual modulation (Fig. 14d) [292]. In the case of optical modulation, the photo-generated electrons transfer from PTCDA to MoS₂ and gradually return to PTCDA after the light being removed. This process results in an excitatory postsynaptic current (EPSC) behavior, meaning that the synaptic weight is strengthened. The synapse plasticity can be controlled by the gate voltage. A relatively positive voltage suppresses the returning process of electrons from MoS₂ to PTCDA is suppressed, resulting in a longer recovery relaxation time and finally LTP formation.

4.3. Optical communication

Over recent years, massive advances have been made in visible light communication (VLC) for supplementing conventional radio frequency communication as the radio spectral resources have become increasingly scarce [293]. Among different modulation schemes, the Color Shift Modulation (CSK) holds great potential, particularly for high data-rate applications [294]. In CSK modulation systems, the signals are modulated using the intensity of LED lights with different color wavelengths. It normally requires more than

one photodetector with different detection range, which greatly complicate the system. Thus, it is highly desirable to develop photodetectors with selective photoresponse for multi-wavelength. To this end, Ouyang et al. reported a ZnO/Sb₂Se₃ heterojunction photodetector with a dual-polarity response (Fig. 14e–h) [295]. The polarity of the output signal is determined by the wavelength of the incident light, where the current signals are negative in the visible range and positive in the near-infrared range. According to the band diagram, two effects are governing the optoelectronic process, namely photovoltaic and photothermoelectric. For the photovoltaic effect, the photogenerated electrons in the Sb₂Se₃ window layer drift towards ZnO and holes in the opposite direction due to the build-in field at the type-II interface, resulting in the output current flow from ITO electrode to Ag electrode in the external circuit. On the other hand, the photothermoelectric effect of the Sb₂Se₃ creates a thermopotential, repelling the holes in Sb₂Se₃ away from the ITO electrode, thus the direction of output current in the external circuit is from Ag electrode to ITO electrode. Therefore, the dual-polarity response can be attributed to the competition between photovoltaic and photothermoelectrics. Furthermore, the dual-polarity photodetector exhibits a great application potential in VLC system as demonstrated in the unipolar and bipolar transmission, a maximum transmission rate of 18 bps, and the accurate indoor positioning by a 4 × 4 photodetector array.

5. Summary and perspective

In this review, we discussed the recent development of type-II nano-heterojunctions for optoelectronics with a focus on rational material, structural, and synthetic design. The key to designing

type-II nano-heterojunctions for high-performance optoelectronics is to efficiently modulate the carrier transfer at the interface in a controlled manner. To this end, many strategies have been developed. Foremost, the band alignment at the interface is of great importance. Favorable band alignment has to be able to balance the carrier separation, confinement, as well as recombination, from an application-oriented point of view. With the rapid advances of synthesis techniques, the precise chemical composition tuning such as alloying and doping provides a powerful tool in the control of the desired band alignment. Additionally, the types of type-II heterojunction, namely isotype or anisotype, have to be taken into account, as they determine the majority carrier type at the interface, thus greatly impact the device performance. Furthermore, the crystal structure engineering not only was utilized to modify the intrinsic electronic and optoelectronic properties of the semiconductor materials which forming the heterojunction but also leads to intriguing concepts such as phase heterojunction and facet heterojunction. Moreover, the interface strain and the associated defect are inevitable in the case of most heterojunctions. Indeed, understanding the strain distribution and its effect on the quality of the materials and the properties of the heterojunction, and thus avoiding any unfavorable side effects is required for growth process optimization and ultimate device fabrication. On the other hand, by taking advantage of the strain effect, the strain engineering paves an alternative efficient route in tuning the heterojunction properties. Attention should be paid to the structural modification as well, as each class of the type-II nano-heterojunctions has characteristically advantageous electronic and optoelectronic properties. Lastly, it is worth emphasizing the external effect on the performance of type-II nano-heterojunctions. We believe this provides a bright opportunity for bridging the day-to-day life activities and next-generation optoelectronic devices, which is much required in the area of the Internet of Things.

Although tremendous progress has been achieved, substantial opportunities remain for future research. Firstly, many of the current research is still in the lab at the early stage of research and development. Thus, intensive work has to be done in terms of large-scale material production, reliable device fabrication, material safety, and long-term stability. Secondly, many fundamental issues have to be better understood. For example, in comparison to 0D and 2D heterojunctions, 1D heterojunction, especially those with array structure, normally has a relatively large size in the range of 100 nm. As a result, it exhibits less profound quantum confinement effect. Unlike 0D and 2D heterojunctions with a simple interface, the complicated structure obstacles the probe of the underlying photophysics process. Thirdly, the increasing demands of the transparent, flexible, stretchable, wearable, or implantable optoelectronic device, as well as emergent applications such as optical computing, neuromorphic computing, and biomimetic sensory systems have pushed the optoelectronic to a new frontier. Overall, by combining advances from multiple disciplines including physics, chemistry, material science, and engineering, it is anticipated that more exciting achievements of type-II nano-heterojunctions will be attained in optoelectronics in the foreseeable future.

Declaration of competing interest

The authors declare that they have no known competing financial interests or personal relationships that could have appeared to influence the work reported in this paper.

Acknowledgment

This study was supported financially by the DARPA grant no. HR0011-07-1-0032 and Louisiana Board of Regents

contract No. LEQSF(2011–13)-RD-B-08. Xiaotao Zu acknowledges the funding support (U1830204) from National Science Foundation of China.

References

- [1] H. Kroemer, Nobel Lecture: quasielectric fields and band offsets: teaching electrons new tricks, *Rev Mod Phys* 73 (2001) 783–793, <https://doi.org/10.1103/RevModPhys.73.783>.
- [2] J. Mannhart, D.G. Schlom, Oxide Interfaces-An opportunity for electronics, *Science* 327 (80) (2010) 1607–1611, <https://doi.org/10.1126/science.1181862>.
- [3] H. Zheng, Y. Li, H. Liu, X. Yin, Y. Li, Construction of heterostructure materials toward functionality, *Chem Soc Rev* 40 (2011) 4506, <https://doi.org/10.1039/c0cs00222d>.
- [4] Y. Zhang, Type II heterostructures in wide band gap semiconductor nanowires for optical devices: the particular case of GaN and ZnO, in: V. Consonni, G. Guy Feuillet (Eds.), *Wide Band Gap Semicond. Nanowires 2 Heterostruct. Optoelectron. Devices*, Wiley-ISTE, 2014.
- [5] F. Capasso, Band-gap engineering: from physics and materials to new semiconductor devices, *Science* 235 (80) (1987) 172–176, <https://doi.org/10.1126/science.235.4785.172>.
- [6] F. Capasso, Bandgap and interface engineering for advanced electronic and photonic devices, *MRS Bull* 16 (1991) 23–29, <https://doi.org/10.1557/S0883769400056700>.
- [7] H. Kum, D. Lee, W. Kong, H. Kim, Y. Park, Y. Kim, Y. Baek, S.-H. Bae, K. Lee, J. Kim, Epitaxial growth and layer-transfer techniques for heterogeneous integration of materials for electronic and photonic devices, *Nat Electron* 2 (2019) 439–450, <https://doi.org/10.1038/s41928-019-0314-2>.
- [8] W. Lu, C.M. Lieber, Nanoelectronics from the bottom up, *Nat Mater* 6 (2007) 841–850, <https://doi.org/10.1038/nmat2028>.
- [9] C. Jia, Z. Lin, Y. Huang, X. Duan, Nanowire electronics: from nanoscale to macroscale, *Chem Rev* (2019), <https://doi.org/10.1021/acs.chemrev.9b00164>.
- [10] C.-Z. Ning, L. Dou, P. Yang, Bandgap engineering in semiconductor alloy nanomaterials with widely tunable compositions, *Nat Rev Mater* 2 (2017) 17070, <https://doi.org/10.1038/natrevmats.2017.70>.
- [11] Y. Zhang, L.W. Wang, A. Mascarenhas, “Quantum coaxial cables” for solar energy harvesting, *Nano Lett* 7 (2007) 1264–1269, <https://doi.org/10.1021/nl070174f>.
- [12] K. Wang, J. Chen, W. Zhou, Y. Zhang, Y. Yan, J. Pern, A. Mascarenhas, Direct growth of highly mismatched type II ZnO/ZnSe core/shell nanowire arrays on transparent conducting oxide substrates for solar cell applications, *Adv Mater* 20 (2008) 3248–3253, <https://doi.org/10.1002/adma.200800145>.
- [13] Z. Wu, Y. Zhang, J. Zheng, X. Lin, X. Chen, B. Huang, H. Wang, K. Huang, S. Li, J. Kang, An all-inorganic type-II heterojunction array with nearly full solar spectral response based on ZnO/ZnSe core/shell nanowires, *J Mater Chem* 21 (2011) 6020–6026, <https://doi.org/10.1039/c0jm03971c>.
- [14] S.S. Lo, T. Mirkovic, C.-H. Chuang, C. Burda, G.D. Scholes, Emergent properties resulting from type-II band Alignment in semiconductor nano-heterostructures, *Adv Mater* 23 (2011) 180–197, <https://doi.org/10.1002/adma.201002290>.
- [15] Y. Wang, Q. Wang, X. Zhan, F. Wang, M. Safdar, J. He, Visible light driven type II heterostructures and their enhanced photocatalysis properties: a review, *Nanoscale* 5 (2013) 8326, <https://doi.org/10.1039/c3nr01577g>.
- [16] J. Chen, W. Ouyang, W. Yang, J. He, X. Fang, Recent progress of heterojunction ultraviolet photodetectors: materials, integrations, and applications, *Adv Funct Mater* 30 (2020) 1909909, <https://doi.org/10.1002/adfm.201909909>.
- [17] K. Afroz, M. Moniruddin, N. Bakranov, S. Kudaibergenov, N. Nuraje, A heterojunction strategy to improve the visible light sensitive water splitting performance of photocatalytic materials, *J Mater Chem A* 6 (2018) 21696–21718, <https://doi.org/10.1039/C8TA04165B>.
- [18] S. Liang, B. Cheng, X. Cui, F. Miao, Van der Waals heterostructures for high-performance device applications: challenges and opportunities, *Adv Mater* (2019): 1903800, <https://doi.org/10.1002/adma.201903800>.
- [19] O. Voznyy, B.R. Sutherland, A.H. Ip, D. Zhitomirsky, E.H. Sargent, Engineering charge transport by heterostructuring solution-processed semiconductors, *Nat Rev Mater* 2 (2017) 17026, <https://doi.org/10.1038/natrevmats.2017.26>.
- [20] H. Kroemer, G. Griffiths, Staggered-lineup heterojunctions as sources of tunable below-gap radiation: operating principle and semiconductor selection, *IEEE Electron Device Lett* 4 (1983) 20–22, <https://doi.org/10.1109/EDL.1983.25631>.
- [21] Q. Ou, X. Bao, Y. Zhang, H. Shao, G. Xing, X. Li, L. Shao, Q. Bao, Band structure engineering in metal halide perovskite nanostructures for optoelectronic applications, *Nano Mater Sci* 1 (2019) 268–287, <https://doi.org/10.1016/j.namoms.2019.10.004>.
- [22] S. Siol, J.C. Hellmann, S.D. Tilley, M. Graetzel, J. Morasch, J. Deuermeier, W. Jaegermann, A. Klein, Band Alignment engineering at Cu₂O/ZnO heterointerfaces, *ACS Appl Mater Interfaces* 8 (2016) 21824–21831, <https://doi.org/10.1021/acsami.6b07325>.
- [23] B. Zheng, C. Ma, D. Li, J. Lan, Z. Zhang, X. Sun, W. Zheng, T. Yang, C. Zhu, G. Ouyang, G. Xu, X. Zhu, X. Wang, A. Pan, Band Alignment engineering in two-dimensional lateral heterostructures, *J Am Chem Soc* 140 (2018)

- 11193–11197, <https://doi.org/10.1021/jacs.8b07401>.
- [24] L. Li, W. Zheng, C. Ma, H. Zhao, F. Jiang, Y. Ouyang, B. Zheng, X. Fu, P. Fan, M. Zheng, Y. Li, Y. Xiao, W. Cao, Y. Jiang, X. Zhu, X. Zhuang, A. Pan, Wave-length-tunable interlayer exciton emission at the near-infrared region in van der Waals semiconductor heterostructures, *Nano Lett* 20 (2020) 3361–3368, <https://doi.org/10.1021/acs.nanolett0c00258>.
- [25] R. Wick-Joliat, T. Musso, R.R. Prabhakar, J. Lückinger, S. Siol, W. Cui, L. Sévery, T. Moehl, J. Suh, J. Hutter, M. Iannuzzi, S.D. Tilley, Stable and tunable phosphonic acid dipole layer for band edge engineering of photoelectrochemical and photovoltaic heterojunction devices, *Energy Environ Sci* 12 (2019) 1901–1909, <https://doi.org/10.1039/C9EE00748B>.
- [26] S. Wozny, K. Wang, W. Zhou, Cu₂ZnSnS₄ nanoplate arrays synthesized by pulsed laser deposition with high catalytic activity as counter electrodes for dye-sensitized solar cell applications, *J Mater Chem A* 1 (2013) 15517–15523, <https://doi.org/10.1039/C3ta13358c>.
- [27] A. Crovetto, O. Hansen, What is the band alignment of Cu₂ZnSn(S,Se)₄ solar cells? *Sol Energy Mater Sol Cells* 169 (2017) 177–194, <https://doi.org/10.1016/j.solmat.2017.05.008>.
- [28] T.J. Huang, X. Yin, G. Qi, H. Gong, CZTS-based materials and interfaces and their effects on the performance of thin film solar cells, *Phys Status Solidi Rapid Res Lett* 8 (2014) 735–762, <https://doi.org/10.1002/pssr.201409219>.
- [29] Y. Liu, J. Zhu, G. Cen, J. Zheng, D. Xie, Z. Zhao, C. Zhao, W. Mai, Valence-state controllable fabrication of Cu_{2-x}O/Si type-II heterojunction for high-performance photodetectors, *ACS Appl Mater Interfaces* 11 (2019) 43376–43382, <https://doi.org/10.1021/acsmami.9b15727>.
- [30] Z. Pan, W. Peng, F. Li, Y. He, Piezo-phototronic effect on performance enhancement of anisotype and isotype heterojunction photodiodes, *Adv Funct Mater* 28 (2018): 1706897, <https://doi.org/10.1002/adfm.201706897>.
- [31] Y. Dai, X. Wang, W. Peng, C. Wu, Y. Ding, K. Dong, Z.L. Wang, Enhanced performances of Si/CdS heterojunction near-infrared photodetector by the piezo-phototronic effect, *Nano Energy* 44 (2018) 311–318, <https://doi.org/10.1016/j.nanoen.2017.11.076>.
- [32] W.G. Oldham, A.G. Milnes, n-n Semiconductor heterojunctions, *Solid State Electron* 6 (1963) 121–132, [https://doi.org/10.1016/0038-1101\(63\)90005-4](https://doi.org/10.1016/0038-1101(63)90005-4).
- [33] J. Lee, S. Pak, P. Giraud, Y.-W. Lee, Y. Cho, J. Hong, A.-R. Jang, H.-S. Chung, W.-K. Hong, H.Y. Jeong, H.S. Shin, L.G. Occhipinti, S.M. Morris, S. Cha, J.I. Sohn, J.M. Kim, Thermodynamically stable synthesis of large-scale and highly crystalline transition metal dichalcogenide monolayers and their unipolar n-n heterojunction devices, *Adv Mater* 29 (2017): 1702206, <https://doi.org/10.1002/adma.201702206>.
- [34] S. Jeong, M.W. Kim, Y.-R. Jo, T.-Y. Kim, Y.-C. Leem, S.-W. Kim, B.-J. Kim, S.-J. Park, Crystal-structure-dependent piezotronic and piezo-phototronic effects of ZnO/ZnS core/shell nanowires for enhanced electrical transport and photosensing performance, *ACS Appl Mater Interfaces* 10 (2018) 28736–28744, <https://doi.org/10.1021/acsami.8b06192>.
- [35] Y. Fu, F. Cao, F. Wu, Z. Diao, J. Chen, S. Shen, L. Li, Phase-modulated band Alignment in CdS nanorod/SnS_x nanosheet hierarchical heterojunctions toward efficient water splitting, *Adv Funct Mater* 28 (2018): 1706785, <https://doi.org/10.1002/adfm.201706785>.
- [36] S. Bai, C. Gao, J. Low, Y. Xiong, Crystal phase engineering on photocatalytic materials for energy and environmental applications, *Nano Res* 12 (2019) 2031–2054, <https://doi.org/10.1007/s12274-018-2267-6>.
- [37] X. Wang, C. Li, Roles of phase junction in photocatalysis and photoelectrocatalysis, *J Phys Chem C* 122 (2018) 21083–21096, <https://doi.org/10.1021/acs.jpcc.8b06039>.
- [38] T. Kawahara, Y. Konishi, H. Tada, N. Tohge, J. Nishii, S. Ito, A patterned TiO₂(anatase)/TiO₂(rutile) bilayer-type photocatalyst: effect of the anatase/rutile junction on the photocatalytic activity, *Angew Chem Int Ed* 41 (2002) 2811–2813, [https://doi.org/10.1002/1521-3773\(20020802\)41:15<2811::AID-ANIE2811>3.0.CO;2-#](https://doi.org/10.1002/1521-3773(20020802)41:15<2811::AID-ANIE2811>3.0.CO;2-#).
- [39] D.O. Scanlon, C.W. Dunnill, J. Buckeridge, S.A. Shevlin, A.J. Logsdail, S.M. Woodley, C.R.A. Catlow, M.J. Powell, R.G. Palgrave, I.P. Parkin, G.W. Watson, T.W. Keal, P. Sherwood, A. Walsh, A.A. Sokol, Band alignment of rutile and anatase TiO₂, *Nat Mater* 12 (2013) 798–801, <https://doi.org/10.1038/nmat3697>.
- [40] F. Cao, J. Xiong, F. Wu, Q. Liu, Z. Shi, Y. Yu, X. Wang, L. Li, Enhanced photoelectrochemical performance from rationally designed anatase/rutile TiO₂ heterostructures, *ACS Appl Mater Interfaces* 8 (2016) 12239–12245, <https://doi.org/10.1021/acsami.6b03842>.
- [41] A. Li, Z. Wang, H. Yin, S. Wang, P. Yan, B. Huang, X. Wang, R. Li, X. Zong, H. Han, C. Li, Understanding the anatase-rutile phase junction in charge separation and transfer in a TiO₂ electrode for photoelectrochemical water splitting, *Chem Sci* 7 (2016) 6076–6082, <https://doi.org/10.1039/c6sc01611a>.
- [42] W. Zhang, H. He, Y. Tian, K. Lan, Q. Liu, C. Wang, Y. Liu, A. Elzatahy, R. Che, W. Li, D. Zhao, Synthesis of uniform ordered mesoporous TiO₂ microspheres with controllable phase junctions for efficient solar water splitting, *Chem Sci* 10 (2019) 1664–1670, <https://doi.org/10.1039/c8sc04155e>.
- [43] Y. Wang, Y. Shi, C. Zhao, Q. Zheng, J. Zhao, Photogenerated carrier dynamics at the anatase/rutile TiO₂ interface, *Phys Rev B* 99 (2019): 165309, <https://doi.org/10.1103/PhysRevB.99.165309>.
- [44] T. Tian, D. Wang, K. Bu, J. Lin, S. Zhang, W. Zhao, P. Qin, F. Huang, Highly conductive cable-like bicomponent titania photoanode approaching limitation of electron and hole collection, *Adv Funct Mater* 28 (2018): 1803328, <https://doi.org/10.1002/adfm.201803328>.
- [45] Q. Tay, X. Liu, Y. Tang, Z. Jiang, T.C. Sum, Z. Chen, Enhanced photocatalytic hydrogen production with synergistic two-phase anatase/brookite TiO₂ nanostructures, *J Phys Chem C* 117 (2013) 14973–14982, <https://doi.org/10.1021/jp4040979>.
- [46] S.M. El-Sheikh, T.M. Khedr, G. Zhang, V. Vogiazi, A.A. Ismail, K. O'Shea, D.D. Dionysiou, Tailored synthesis of anatase–brookite heterojunction photocatalysts for degradation of cylindrospermopsin under UV–Vis light, *Chem Eng J* 310 (2017) 428–436, <https://doi.org/10.1016/j.cej.2016.05.007>.
- [47] X. Wang, Q. Xu, M. Li, S. Shen, X. Wang, Y. Wang, Z. Feng, J. Shi, H. Han, C. Li, Photocatalytic overall water splitting promoted by an α - β phase junction on Ga₂O₃, *Angew Chem Int Ed* 51 (2012) 13089–13092, <https://doi.org/10.1002/anie.201207554>.
- [48] S. Jin, X. Wang, X. Wang, M. Ju, S. Shen, W. Liang, Y. Zhao, Z. Feng, H.Y. Playford, R.I. Walton, C. Li, Effect of phase junction structure on the photocatalytic performance in overall water splitting: Ga₂O₃ photocatalyst as an example, *J Phys Chem C* 119 (2015) 18221–18228, <https://doi.org/10.1021/acs.jpcc.5b04092>.
- [49] Y. Sun, W. Wang, L. Zhang, Z. Zhang, Design and controllable synthesis of α - γ -Bi₂O₃ homojunction with synergistic effect on photocatalytic activity, *Chem Eng J* 211–212 (2012) 161–167, <https://doi.org/10.1016/j.cej.2012.09.084>.
- [50] J. Hou, C. Yang, Z. Wang, W. Zhou, S. Jiao, H. Zhu, In situ synthesis of α - β phase heterojunction on Bi₂O₃ nanowires with exceptional visible-light photocatalytic performance, *Appl Catal B Environ.* 142–143 (2013) 504–511, <https://doi.org/10.1016/j.apcatb.2013.05.050>.
- [51] P. Wang, P. Chen, A. Kostka, R. Marschall, M. Wark, Control of phase coexistence in calcium tantalate composite photocatalysts for highly efficient hydrogen production, *Chem Mater* 25 (2013) 4739–4745, <https://doi.org/10.1021/cm402708h>.
- [52] J. Cheng, J. Feng, W. Pan, Enhanced photocatalytic activity in electrospun bismuth vanadate nanofibers with phase junction, *ACS Appl Mater Interfaces* 7 (2015) 9638–9644, <https://doi.org/10.1021/acsami.5b01305>.
- [53] O.F. Lopes, K.T.G. Carvalho, A.E. Nogueira, W. Avansi, C. Ribeiro, Controlled synthesis of BiVO₄ photocatalysts: evidence of the role of heterojunctions in their catalytic performance driven by visible-light, *Appl Catal B Environ.* 188 (2016) 87–97, <https://doi.org/10.1016/j.apcatb.2016.01.065>.
- [54] Z. Ai, G. Zhao, Y. Zhong, Y. Shao, B. Huang, Y. Wu, X. Hao, Phase junction CdS: high efficient and stable photocatalyst for hydrogen generation, *Appl Catal B Environ.* 221 (2018) 179–186, <https://doi.org/10.1016/j.apcatb.2017.09.002>.
- [55] Y. Chai, J. Lu, L. Li, D. Li, M. Li, J. Liang, TEOA-induced in situ formation of wurtzite and zinc-blende CdS heterostructures as a highly active and long-lasting photocatalyst for converting CO₂ into solar fuel, *Catal Sci Technol* 8 (2018) 2697–2706, <https://doi.org/10.1039/C8CY00274F>.
- [56] K. Li, M. Han, R. Chen, S.-L. Li, S.-L. Xie, C. Mao, X. Bu, X.-L. Cao, L.-Z. Dong, P. Feng, Y.-Q. Lan, Hexagonal@Cubic CdS Core@Shell nanorod photocatalyst for highly active production of H₂ with unprecedented stability, *Adv Mater* 28 (2016) 8906–8911, <https://doi.org/10.1002/adma.201601047>.
- [57] Z. Ren, J. Wu, N. Wang, X. Li, An Er-doped TiO₂ phase junction as an electron transport layer for efficient perovskite solar cells fabricated in air, *J Mater Chem A* 6 (2018) 15348–15358, <https://doi.org/10.1039/c8ta04444a>.
- [58] C. Wu, C. He, D. Guo, F. Zhang, P. Li, S. Wang, A. Liu, F. Wu, W. Tang, Vertical α / β -Ga₂O₃ phase junction nanorods array with graphene-silver nanowire hybrid conductive electrode for high-performance self-powered solar-blind photodetectors, *Mater Today Phys* 12 (2020): 100193, <https://doi.org/10.1016/j.mtphys.2020.100193>.
- [59] D.Y. Guo, K. Chen, S.L. Wang, F.M. Wu, A.P. Liu, C.R. Li, P.G. Li, C.K. Tan, W.H. Tang, Self-powered solar-blind photodetectors based on α / β phase junction of Ga₂O₃, *Phys Rev Appl* 13 (2020): 024051, <https://doi.org/10.1103/PhysRevApplied.13.024051>.
- [60] F. Ma, J. Li, W. Li, N. Lin, L. Wang, J. Qiao, Stable α / δ phase junction of formamidinium lead iodide perovskites for enhanced near-infrared emission, *Chem Sci* 8 (2016) 800–805, <https://doi.org/10.1039/c6sc03542f>.
- [61] P. Yan, X. Wang, X. Zheng, R. Li, J. Han, J. Shi, A. Li, Y. Gan, C. Li, Photovoltaic device based on TiO₂ rutile/anatase phase junctions fabricated in coaxial nanorod arrays, *Nano Energy* 15 (2015) 406–412, <https://doi.org/10.1016/j.nanoen.2015.05.005>.
- [62] Y. Zhu, K. Deng, H. Sun, B. Gu, H. Lu, F. Cao, J. Xiong, L. Li, TiO₂ phase junction electron transport layer boosts efficiency of planar perovskite solar cells, *Adv Sci* 5 (2018): 1700614, <https://doi.org/10.1002/advs.201700614>.
- [63] X. Yu, Z. Zhao, J. Zhang, W. Guo, J. Qiu, D. Li, Z. Li, X. Mou, L. Li, A. Li, H. Liu, Rutile nanorod/anatase nanowire junction array as both sensor and power supplier for high-performance, self-powered, wireless UV photodetector, *Small* 12 (2016) 2759–2767, <https://doi.org/10.1002/small.201503388>.
- [64] A. Panepinto, M. Michiels, M.T. Dürrschnabel, L. Molina-Luna, C. Bittencourt, P.A. Cormier, R. Snyder, Synthesis of anatase (Core)/Rutile (shell) nanostructured TiO₂ thin films by magnetron sputtering methods for dye-sensitized solar cell applications, *ACS Appl Energy Mater* 3 (2020) 759–767, <https://doi.org/10.1021/acsaelm.9b01910>.
- [65] M. Shahiduzzaman, S. Visal, M. Kuniyoshi, T. Kaneko, S. Umezawa, T. Katsumata, S. Iwamori, M. Kakihana, T. Taima, M. Isomura, K. Tomita, Low-temperature-processed brookite-based TiO₂ heterophase junction enhances performance of planar perovskite solar cells, *Nano Lett* 19 (2019) 598–604, <https://doi.org/10.1021/acs.nanolett.9b04744>.
- [66] S. Wang, G. Liu, L. Wang, Crystal facet engineering of photoelectrodes for

- photoelectrochemical water splitting, *Chem Rev* 119 (2019) 5192–5247, <https://doi.org/10.1021/acs.chemrev.8b00584>.
- [67] Y. Zhang, A. Mascarenhas, Orientational superlattices formed by CuPt-ordered zinc-blende semiconductor alloys, *Phys Rev B Condens Matter* 55 (1997) 13100–13110, <https://doi.org/10.1103/PhysRevB.55.13100>.
- [68] Y. Zhang, B. Fluegel, A. Mascarenhas, Total negative refraction in real crystals for ballistic electrons and light, *Phys Rev Lett* 91 (2003) 157404, <https://doi.org/10.1103/PhysRevLett.91.157404>.
- [69] J. Yu, J. Low, W. Xiao, P. Zhou, M. Jaroniec, Enhanced photocatalytic CO₂-reduction activity of anatase TiO₂ by coexposed {001} and {101} facets, *J Am Chem Soc* 136 (2014) 8839–8842, <https://doi.org/10.1021/ja5044787>.
- [70] A.Y. Zhang, W.Y. Wang, J.J. Chen, C. Liu, Q.X. Li, X. Zhang, W.W. Li, Y. Si, H.Q. Yu, Epitaxial facet junctions on TiO₂ single crystals for efficient photocatalytic water splitting, *Energy Environ Sci* 11 (2018) 1444–1448, <https://doi.org/10.1039/c7ee03482b>.
- [71] P. Li, Y. Zhou, Z. Zhao, Q. Xu, X. Wang, M. Xiao, Z. Zou, Hexahedron prism-anchored octahedral CeO₂: crystal facet-based homojunction promoting efficient solar fuel synthesis, *J Am Chem Soc* 137 (2015) 9547–9550, <https://doi.org/10.1021/jacs.5b05926>.
- [72] R. Li, F. Zhang, D. Wang, J. Yang, M. Li, J. Zhu, X. Zhou, H. Han, C. Li, Spatial separation of photogenerated electrons and holes among {010} and {110} crystal facets of BiVO₄, *Nat Commun* 4 (2013) 1–7, <https://doi.org/10.1038/ncomms2401>.
- [73] F. Chen, H. Huang, L. Ye, T. Zhang, Y. Zhang, X. Han, T. Ma, Thickness-dependent facet junction control of layered BiO_{1-x}O_x single crystals for highly efficient CO₂ photoreduction, *Adv Funct Mater* 28 (2018) 1804284, <https://doi.org/10.1002/adfm.201804284>.
- [74] C. Gao, T. Wei, Y. Zhang, X. Song, Y. Huan, H. Liu, M. Zhao, J. Yu, X. Chen, A photoresponsive rutile TiO₂ heterojunction with enhanced electron-hole separation for high-performance hydrogen evolution, *Adv Mater* 31 (2019): 1806596, <https://doi.org/10.1002/adma.201806596>.
- [75] W. Ouyang, F. Teng, X. Fang, High performance BiOCl nanosheets/TiO₂ nanotube Arrays heterojunction UV photodetector: the influences of self-induced inner electric fields in the BiOCl nanosheets, *Adv Funct Mater* 28 (2018): 1707178, <https://doi.org/10.1002/adfm.201707178>.
- [76] S. Sivakumar Rashmi, R.G.S. Pala, Coherency and lattice misfit strain critically constrains electron–hole separation in isomaterial and heteromaterial type-II heterostructures, *J Phys Chem C* 123 (2019) 28620–28630, <https://doi.org/10.1021/acs.jpcc.9b08451>.
- [77] B. Liu, Q. Liao, X. Zhang, J. Du, Y. Ou, J. Xiao, Z. Kang, Z. Zhang, Y. Zhang, Strain-Engineered van der Waals interfaces of mixed-dimensional heterostructure arrays, *ACS Nano* 13 (2019) 9057–9066, <https://doi.org/10.1021/acsnano.9b03239>.
- [78] C. Zhang, M.-Y. Li, J. Tersoff, Y. Han, Y. Su, L.-J. Li, D.A. Muller, C.-K. Shih, Strain distributions and their influence on electronic structures of WSe₂–MoS₂ laterally strained heterojunctions, *Nat Nanotechnol* 13 (2018) 152–158, <https://doi.org/10.1038/s41565-017-0022-x>.
- [79] G.S. Selopal, H. Zhao, Z.M. Wang, F. Rosei, Core/shell quantum dots solar cells, *Adv Funct Mater* 30 (2020): 1908762, <https://doi.org/10.1002/adfm.201908762>.
- [80] S. Kim, B. Fisher, H.-J. Eisler, M. Bawendi, Type-II quantum dots: CdTe/CdSe(Core/Shell) and CdSe/ZnTe(Core/Shell) heterostructures, *J Am Chem Soc* 125 (2003) 11466–11467, <https://doi.org/10.1021/ja0361749>.
- [81] J.B. Sambur, T. Novet, B.A. Parkinson, Multiple exciton collection in a sensitized photovoltaic system, *Science* 330 (80) (2010) 63–66, <https://doi.org/10.1126/science.1191462>.
- [82] N. Siemons, A. Serafini, Multiple exciton generation in nanostructures for advanced photovoltaic cells, *J Nanotechnol* 2018 (2018) 1–12, <https://doi.org/10.1155/2018/728543>.
- [83] C.M. Cirloganu, L.A. Padilha, Q. Lin, N.S. Makarov, K.A. Velizhanin, H. Luo, I. Robel, J.M. Pietryga, V.I. Klimov, Enhanced carrier multiplication in engineered quasi-type-II quantum dots, *Nat Commun* 5 (2014) 4148, <https://doi.org/10.1038/ncomms5148>.
- [84] H. Eshet, R. Baer, D. Neuhauser, E. Rabani, Theory of highly efficient multi-exciton generation in type-II nanorods, *Nat Commun* 7 (2016) 13178, <https://doi.org/10.1038/ncomms13178>.
- [85] F. Chen, Z. Guan, A. Tang, Nanostructure and device architecture engineering for high-performance quantum-dot light-emitting diodes, *J Mater Chem C* 6 (2018) 10958–10981, <https://doi.org/10.1039/C8TC04028A>.
- [86] S. Nakamura, Background story of the invention of efficient InGaN blue-light-emitting diodes (Nobel lecture), *Angew Chem Int Ed* 54 (2015) 7770–7788, <https://doi.org/10.1002/anie.201500591>.
- [87] Y. Jiang, S.Y. Cho, M. Shim, Light-emitting diodes of colloidal quantum dots and nanorod heterostructures for future emissive displays, *J Mater Chem C* 6 (2018) 2618–2634, <https://doi.org/10.1039/c7tc05972h>.
- [88] D. Oron, M. Kazes, Y. Banin, Multiexcitons in type-II colloidal semiconductor quantum dots, *Phys Rev B Condens Matter* 75 (2007): 035330, <https://doi.org/10.1103/PhysRevB.75.035330>.
- [89] W.K. Bae, L.A. Padilha, Y.S. Park, H. McDaniel, I. Robel, J.M. Pietryga, V.I. Klimov, Controlled alloying of the core-shell interface in CdSe/CdS quantum dots for suppression of auger recombination, *ACS Nano* 7 (2013) 3411–3419, <https://doi.org/10.1021/nn4002825>.
- [90] V.I. Klimov, S.A. Ivanov, J. Nanda, M. Achermann, I. Bezel, J.A. McGuire, A. Piryatinski, Single-exciton optical gain in semiconductor nanocrystals, *Nature* 447 (2007) 441–446, <https://doi.org/10.1038/nature05839>.
- [91] S.A. Ivanov, A. Piryatinski, J. Nanda, S. Tretiak, K.R. Zavadil, W.O. Wallace, D. Werder, V.I. Klimov, Type-II core/shell CdS/ZnSe nanocrystals: synthesis, electronic structures, and spectroscopic properties, *J Am Chem Soc* 129 (2007) 11708–11719, <https://doi.org/10.1021/ja068351m>.
- [92] Z. Yang, M. Gao, W. Wu, X. Yang, X.W. Sun, J. Zhang, H.C. Wang, R.S. Liu, C.Y. Han, H. Yang, W. Li, Recent advances in quantum dot-based light-emitting devices: challenges and possible solutions, *Mater Today* 24 (2019) 69–93, <https://doi.org/10.1016/j.mattod.2018.09.002>.
- [93] C.M. Tyarakowski, A. Shamirian, C.E. Rowland, H. Shen, A. Das, R.D. Schaller, P.T. Snee, Bright type II quantum dots, *Chem Mater* 27 (2015) 7276–7281, <https://doi.org/10.1021/acs.chemmater.5b02040>.
- [94] N. Oh, S. Nam, Y. Zhai, K. Deshpande, P. Trefonas, M. Shim, Double-heterojunction nanorods, *Nat Commun* 5 (2014) 1–8, <https://doi.org/10.1038/ncomms4642>.
- [95] E.C. Garnett, M.L. Brongersma, Y. Cui, M.D. McGehee, Nanowire solar cells, *Annu Rev Mater Res* 41 (2011) 269–295, <https://doi.org/10.1146/annurev-matsci-062910-100434>.
- [96] W. Ouyang, F. Teng, J.-H. He, X. Fang, Enhancing the photoelectric performance of photodetectors based on metal oxide semiconductors by charge-carrier engineering, *Adv Funct Mater* (2019): 1807672, <https://doi.org/10.1002/adfm.201807672>.
- [97] R. Yan, D. Gargas, P. Yang, Nanowire photonics, *Nat Photon* 3 (2009) 569–576, <https://doi.org/10.1038/nphoton.2009.184>.
- [98] F. Glas, Critical dimensions for the plastic relaxation of strained axial heterostructures in free-standing nanowires, *Phys Rev B Condens Matter* 74 (2006): 121302, <https://doi.org/10.1103/PhysRevB.74.121302>.
- [99] G. Otnes, M.T. Borgström, Towards high efficiency nanowire solar cells, *Nano Today* 12 (2017) 31–45, <https://doi.org/10.1016/j.nantod.2016.10.007>.
- [100] B. Cao, J. Chen, R. Huang, Y.H. Ikuhara, T. Hirayama, W. Zhou, Axial growth of Zn₂GeO₄/ZnO nanowire heterojunction using chemical vapor deposition, *J Cryst Growth* 316 (2011) 46–50, <https://doi.org/10.1016/j.jcrysgro.2010.12.060>.
- [101] M.-Y. Lu, J. Song, M.-P. Lu, C.-Y. Lee, L.-J. Chen, Z.L. Wang, ZnO–ZnS heterojunction and ZnS nanowire arrays for electricity generation, *ACS Nano* 3 (2009) 357–362, <https://doi.org/10.1021/nm08004r>.
- [102] M. De La Mata, R.R. Zamani, S. Martí-Sánchez, M. Eickhoff, Q. Xiong, A. Fontcuberta Morral, P. Caroff, J. Arbiol, The role of polarity in nonplanar semiconductor nanostructures, *Nano Lett* 19 (2019) 3396–3408, <https://doi.org/10.1021/acs.nanolett.9b00459>.
- [103] F. Schuster, B. Laumer, R.R. Zamani, C. Magén, J.R. Morante, J. Arbiol, M. Stutzmann, p-GaN/n-ZnO heterojunction nanowires: optoelectronic properties and the role of interface polarity, *ACS Nano* 8 (2014) 4376–4384, <https://doi.org/10.1021/nm406134e>.
- [104] J.D. Christesen, X. Zhang, C.W. Pinion, T.A. Celano, C.J. Flynn, J.F. Cahoon, Design principles for photovoltaic devices based on Si nanowires with axial or radial p-n junctions, *Nano Lett* 12 (2012) 6024–6029, <https://doi.org/10.1021/nl303610m>.
- [105] K. Wang, S.C. Rai, J. Marmon, J. Chen, K. Yao, S. Wozny, B. Cao, Y. Yan, Y. Zhang, W. Zhou, Nearly lattice matched all wurtzite CdSe/ZnTe type II core–shell nanowires with epitaxial interfaces for photovoltaics, *Nanoscale* 6 (2014) 3679–3685, <https://doi.org/10.1039/C3NR06137>.
- [106] M. Hu, F. Teng, H. Chen, M. Jiang, Y. Gu, H. Lu, L. Hu, X. Fang, Novel Ω-shaped core-shell photodetector with high ultraviolet selectivity and enhanced responsivity, *Adv Funct Mater* 27 (2017): 1704477, <https://doi.org/10.1002/adfm.201704477>.
- [107] J. Luo, Z. Zheng, S. Yan, M. Morgan, X. Zu, X. Xiang, W. Zhou, Photocurrent enhanced in UV-vis-NIR photodetector based on CdSe/CdTe core/shell nanowire arrays by piezo-phototronic effect, *ACS Photonics* 7 (2020) 1461–1467, <https://doi.org/10.1021/acsphotonics.0c00122>.
- [108] T. Cossuet, J. Resende, L. Rapenne, O. Chaix-Pluchery, C. Jiménez, G. Renou, A.J. Pearson, R.L.Z. Hoye, D. Blanc-Pelissier, N.D. Nguyen, E. Appert, D. Muñoz-Rojas, V. Consonni, J.-L. Deschanvres, ZnO/CuCrO₂ core-shell nanowire heterostructures for self-powered UV photodetectors with fast response, *Adv Funct Mater* 28 (2018): 1803142, <https://doi.org/10.1002/adfm.201803142>.
- [109] V. Consonni, J. Briscoe, E. Kärber, X. Li, T. Cossuet, ZnO nanowires for solar cells: a comprehensive review, *Nanotechnology* 30 (2019): 362001, <https://doi.org/10.1088/1361-6528/AB1F2E>.
- [110] A. Konkanand, K. Tvrđík, K. Takechi, M. Kuno, P.V. Kamat, Quantum dot solar cells. Tuning photoresponse through size and shape control of CdSe-TiO₂ architecture, *J Am Chem Soc* 130 (2008) 4007–4015, <https://doi.org/10.1021/ja0782706>.
- [111] Z. Pan, H. Rao, I. Mora-Seró, J. Bisquert, X. Zhong, Quantum dot-sensitized solar cells, *Chem Soc Rev* 47 (2018) 7659–7702, <https://doi.org/10.1039/c8cs00431e>.
- [112] H. Dong, F. Xu, Z. Sun, X. Wu, Q. Zhang, Y. Zhai, X.D. Tan, L. He, T. Xu, Z. Zhang, X. Duan, L. Sun, In situ interface engineering for probing the limit of quantum dot photovoltaic devices, *Nat Nanotechnol* 14 (2019) 950–956, <https://doi.org/10.1038/s41565-019-0526-7>.
- [113] Y. Liu, N.O. Weiss, X. Duan, H.C. Cheng, Y. Huang, X. Duan, Van der Waals heterostructures and devices, *Nat Rev Mater* 1 (2016) 1–17, <https://doi.org/10.1038/natrevmat.2016.42>.
- [114] X. Hong, J. Kim, S.-F. Shi, Y. Zhang, C. Jin, Y. Sun, S. Tongay, J. Wu, Y. Zhang, F. Wang, Ultrafast charge transfer in atomically thin MoS₂/WS₂ heterostructures, *Nat Nanotechnol* 9 (2014) 682–686, <https://doi.org/10.1038/nano.2014.167>.

- [115] F. Ceballos, M.Z. Bellus, H.Y. Chiu, H. Zhao, Ultrafast charge separation and indirect exciton formation in a MoS₂-MoSe₂ van der waals heterostructure, ACS Nano 8 (2014) 12717–12724, <https://doi.org/10.1021/nm505736z>.
- [116] P. Rivera, J.R. Schaibley, A.M. Jones, J.S. Ross, S. Wu, G. Aivazian, P. Klement, K. Seyler, G. Clark, N.J. Ghimire, J. Yan, D.G. Mandrus, W. Yao, X. Xu, Observation of long-lived interlayer excitons in monolayer MoSe₂-WSe₂ heterostructures, Nat Commun 6 (2015) 1–6, <https://doi.org/10.1038/ncomms7242>.
- [117] D. Kozawa, A. Carvalho, I. Verzhbitskiy, F. Giustiniano, Y. Miyauchi, S. Moura, A.H. Castro Neto, K. Matsuda, G. Eda, Evidence for fast interlayer energy transfer in MoSe₂/WSe₂ heterostructures, Nano Lett 16 (2016) 4087–4093, <https://doi.org/10.1021/acs.nanolett6b00801>.
- [118] Q. Zeng, Z. Liu, Novel optoelectronic devices: transition-metal-dichalcogenide-based 2D heterostructures, Adv Electron Mater 4 (2018) 1700335, <https://doi.org/10.1002/aem.201700335>.
- [119] H. Taghinejad, A.A. Eftekhari, A. Adibi, Lateral and vertical heterostructures in two-dimensional transition-metal dichalcogenides [Invited], Opt Mater Express 9 (2019) 1590, <https://doi.org/10.1364/ome.9.001590>.
- [120] M.Y. Li, Y. Shi, C.C. Cheng, L.S. Lu, Y.C. Lin, H.L. Tang, M.L. Tsai, C.W. Chu, K.H. Wei, J.H. He, W.H. Chang, K. Suenaga, L.J. Li, Epitaxial growth of a monolayer WSe₂-MoS₂ lateral p-n junction with an atomically sharp interface, Science 349 (80) (2015) 524–528, <https://doi.org/10.1126/science.aab4097>.
- [121] D. Jariwala, T.J. Marks, M.C. Hersam, Mixed-dimensional van der Waals heterostructures, Nat Mater 16 (2017) 170–181, <https://doi.org/10.1038/nmat4703>.
- [122] S. Padgaonkar, J.N. Olding, L.J. Lauhon, M.C. Hersam, E.A. Weiss, Emergent optoelectronic properties of mixed-dimensional heterojunctions, Acc Chem Res 53 (2020) 763–772, <https://doi.org/10.1021/acs.accounts.9b00581>.
- [123] D. Kufer, I. Nikitskiy, T. Lasanta, G. Navickaitė, F.H.L. Koppens, G. Konstantatos, Hybrid 2D-OD MoS₂-PbS quantum dot photodetectors, Adv Mater 27 (2015) 176–180, <https://doi.org/10.1002/adma.201402471>.
- [124] H. Shang, H. Chen, M. Dai, Y. Hu, F. Gao, H. Yang, B. Xu, S. Zhang, B. Tan, X. Zhang, P. Hu, A mixed-dimensional 1D Se–2D InSe van der Waals heterojunction for high responsivity self-powered photodetectors, Nanoscale Horizons 5 (2020) 564–572, <https://doi.org/10.1039/C9NH00705A>.
- [125] P. Sutter, J. Wang, E. Sutter, Wrap-around core–shell heterostructures of layered crystals, Adv Mater 31 (2019) 1902166, <https://doi.org/10.1002/adma.201902166>.
- [126] S.B. Desai, S.R. Madhvapathy, A.B. Sachid, J.P. Llinas, Q. Wang, G.H. Ahn, G. Pitner, M.J. Kim, J. Bokor, C. Hu, H.-S.S.P.P. Wong, A. Javey, MoS₂ transistors with 1-nanometer gate lengths, Science 354 (80) (2016), <https://doi.org/10.1126/science.aaa4698>, 99 LP – 102.
- [127] J. Zhang, L. Cong, K. Zhang, X. Jin, X. Li, Y. Wei, Q. Li, K. Jiang, Y. Luo, S. Fan, Mixed-dimensional vertical point p–n junctions, ACS Nano 14 (2020) 3181–3189, <https://doi.org/10.1021/acsnano.9b08367>.
- [128] Z.L. Wang, W. Wu, Piezotronics and piezo-photronics: fundamentals and applications, Natl Sci Rev 1 (2014) 62–90, <https://doi.org/10.1093/nsr/nwt002>.
- [129] L. Zhu, Z.L. Wang, Recent progress in piezo-phototronic effect enhanced solar cells, Adv Funct Mater 29 (2019): 1808214, <https://doi.org/10.1002/adfm.201808214>.
- [130] Y. Zhang, J. Zhai, Z.L. Wang, Piezo-phototronic matrix via a nanowire array, Small 13 (2017): 1702377, <https://doi.org/10.1002/smll.201702377>.
- [131] Y. Peng, M. Que, J. Tao, X. Wang, J. Lu, G. Hu, B. Wan, Q. Xu, C. Pan, Progress in piezotronic and piezo-phototronic effect of 2D materials, 2D Mater 5 (2018): 042003, <https://doi.org/10.1088/2053-1583/aaabb>.
- [132] C. Pan, J. Zhai, Z.L. Wang, Piezotronics and piezo-photronics of third generation semiconductor nanowires, Chem Rev 119 (2019) 9303–9359, <https://doi.org/10.1021/acs.chemrev.8b00599>.
- [133] C. Pan, M. Chen, R. Yu, Q. Yang, Y. Hu, Y. Zhang, Z.L. Wang, Progress in piezo-phototronic-effect-enhanced light-emitting diodes and pressure imaging, Adv Mater 28 (2016) 1535–1552, <https://doi.org/10.1002/adma.201503500>.
- [134] W. Wu, Z.L. Wang, Piezotronics and piezo-photronics for adaptive electronics and optoelectronics, Natl Rev Mater 1 (2016) 16031, <https://doi.org/10.1038/natrevmats.2016.31>.
- [135] Y. Liu, Y. Zhang, Q. Yang, S. Niu, Z.L. Wang, Fundamental theories of piezotronics and piezo-phototonics, Nano Energy 14 (2015) 257–275.
- [136] Q. Yang, X. Guo, W. Wang, Y. Zhang, S. Xu, D.H. Lien, Z.L. Wang, Enhancing sensitivity of a single ZnO micro-/nanowire photodetector by piezo-phototronic effect, ACS Nano 4 (2010) 6285–6291, <https://doi.org/10.1021/nn1022878>.
- [137] F. Zhang, Y. Ding, Y. Zhang, X. Zhang, Z.L. Wang, Piezo-phototronic effect enhanced visible and ultraviolet photodetection using a ZnO–CdS core–shell micro/nanowire, ACS Nano 6 (2012) 9229–9236, <https://doi.org/10.1021/nn3035765>.
- [138] C. Pan, S. Niu, Y. Ding, L. Dong, R. Yu, Y. Liu, G. Zhu, Z.L. Wang, Enhanced Cu₂S/CdS coaxial nanowire solar cells by piezo-phototronic effect, Nano Lett 12 (2012) 3302–3307, <https://doi.org/10.1021/nl3014082>.
- [139] F. Zhang, S. Niu, W. Guo, G. Zhu, Y. Liu, X. Zhang, Z.L. Wang, Piezo-phototronic effect enhanced visible/UV photodetector of a carbon-fiber/ZnO-CdS double-shell microwire, ACS Nano 7 (2013) 4537–4544, <https://doi.org/10.1021/nn401232k>.
- [140] X. Han, W. Du, R. Yu, C. Pan, Z.L. Wang, Piezo-phototronic enhanced UV sensing based on a nanowire photodetector array, Adv Mater 27 (2015) 7963–7969, <https://doi.org/10.1002/adma.201502579>.
- [141] W. Wu, X. Wang, X. Han, Z. Yang, G. Gao, Y. Zhang, J. Hu, Y. Tan, A. Pan, C. Pan, Flexible photodetector arrays based on patterned CH₃NH₂PbI_{3-x}Cl_x perovskite film for real-time photosensing and imaging, Adv Mater 31 (2019): 1805913, <https://doi.org/10.1002/adma.201805913>.
- [142] F. Xue, L. Chen, J. Chen, J. Liu, L. Wang, M. Chen, Y. Pang, X. Yang, G. Gao, J. Zhai, Z.L. Wang, p-Type MoS₂ and n-type ZnO diode and its performance enhancement by the piezophototronic effect, Adv Mater 28 (2016) 3391–3398, <https://doi.org/10.1002/adma.201506472>.
- [143] S. Jeong, M.W. Kim, Y.R. Jo, Y.C. Leem, W.K. Hong, B.J. Kim, S.J. Park, High-performance photoresponsivity and electrical transport of laterally-grown ZnO/ZnS core/shell nanowires by the piezotronic and piezo-phototronic effect, Nano Energy 30 (2016) 208–216, <https://doi.org/10.1016/j.nanoen.2016.09.046>.
- [144] S.C. Rai, K. Wang, Y. Ding, J.K. Marmon, M. Bhatt, Y. Zhang, W. Zhou, Z.L. Wang, Piezo-phototronic effect enhanced UV/visible photodetector based on fully wide band gap type-II ZnO/ZnS core/shell nanowire array, ACS Nano 9 (2015) 6419–6427, <https://doi.org/10.1021/acsnano.5b02081>.
- [145] G. Hu, W. Guo, R. Yu, X. Yang, R. Zhou, C. Pan, Z.L. Wang, Enhanced performances of flexible ZnO/perovskite solar cells by piezo-phototronic effect, Nano Energy 23 (2016) 27–33, <https://doi.org/10.1016/j.nanoen.2016.02.057>.
- [146] L. Zhu, L. Wang, F. Xue, L. Chen, J. Fu, X. Feng, T. Li, Z.L. Wang, Piezo-phototronic effect enhanced flexible solar cells based on n-ZnO/p-SnS core-shell nanowire array, Adv Sci 4 (2017): 1600185, <https://doi.org/10.1002/advs.201600185>.
- [147] L. Zhu, L. Wang, C. Pan, L. Chen, F. Xue, B. Chen, L. Yang, L. Su, Z.L. Wang, Enhancing the efficiency of silicon-based solar cells by the piezo-phototronic effect, ACS Nano 11 (2017) 1894–1900, <https://doi.org/10.1021/acsnano.6b07960>.
- [148] X. Li, M. Chen, R. Yu, T. Zhang, D. Song, R. Liang, Q. Zhang, S. Cheng, L. Dong, A. Pan, Z.L. Wang, J. Zhu, C. Pan, Enhancing light emission of ZnO-nanofilm/Si-micropillar heterostructure arrays by piezo-phototronic effect, Adv Mater 27 (2015) 4447–4453, <https://doi.org/10.1002/adma.201501121>.
- [149] Y. Peng, M. Que, H.E. Lee, R. Bao, X. Wang, J. Lu, Z. Yuan, X. Li, J. Tao, J. Sun, J. Zhai, K.J. Lee, C. Pan, Achieving high-resolution pressure mapping via flexible GaN/ZnO nanowire LEDs array by piezo-phototronic effect, Nano Energy 58 (2019) 633–640, <https://doi.org/10.1016/j.nanoen.2019.01.076>.
- [150] R. Bao, C. Wang, L. Dong, R. Yu, K. Zhao, Z.L. Wang, C. Pan, Flexible and controllable piezo-phototronic pressure mapping sensor matrix by ZnO NW/p-Polymer LED array, Adv Funct Mater 25 (2015) 2884–2891, <https://doi.org/10.1002/adfm.201500801>.
- [151] X. Li, R. Liang, J. Tao, Z. Peng, Q. Xu, X. Han, X. Wang, C. Wang, J. Zhu, C. Pan, Z.L. Wang, Flexible light emission diode arrays made of transferred Si microwires-ZnO nanofilm with piezo-phototronic effect enhanced lighting, ACS Nano 11 (2017) 3883–3889, <https://doi.org/10.1021/acsnano.7b00272>.
- [152] M. Chen, C. Pan, T. Zhang, X. Li, R. Liang, Z.L. Wang, Tuning light emission of a pressure-sensitive silicon/ZnO nanowires heterostructure matrix through piezo-phototronic effects, ACS Nano 10 (2016) 6074–6079, <https://doi.org/10.1021/acsnano.6b01666>.
- [153] C. Pan, L. Dong, G. Zhu, S. Niu, R. Yu, Q. Yang, Y. Liu, Z.L. Wang, High-resolution electroluminescent imaging of pressure distribution using a piezo-electron nanowire LED array, Nat Photon 7 (2013) 752–758, <https://doi.org/10.1038/nphoton.2013.191>.
- [154] S. Rahman, S. Samanta, A. Kuzmin, D. Errandonea, H. Saqib, D.L. Brewe, J. Kim, J. Lu, L. Wang, Tuning the photoresponse of nano-heterojunction: pressure-induced inverse photoconductance in functionalized WO₃ nano-cuboids, Adv Sci 6 (2019): 1901132, <https://doi.org/10.1002/advs.201901132>.
- [155] C.-H. Lee, G.-H. Lee, A.M. van der Zande, W. Chen, Y. Li, M. Han, X. Cui, G. Arefe, C. Nuckolls, T.F. Heinz, J. Guo, J. Hone, P. Kim, Atomically thin p–n junctions with van der Waals heterointerfaces, Nat Nanotechnol 9 (2014) 676–681, <https://doi.org/10.1038/nnano.2014.150>.
- [156] M.M. Furchi, A. Pospischil, F. Libisch, J. Burgdörfer, T. Mueller, Photovoltaic effect in an electrically tunable Van der Waals heterojunction, Nano Lett 14 (2014) 4785–4791, <https://doi.org/10.1021/nl501962c>.
- [157] H. Fang, W. Hu, Photogating in low dimensional photodetectors, Adv Sci 4 (2017): 1700323, <https://doi.org/10.1002/advs.201700323>.
- [158] H. Tan, W. Xu, Y. Sheng, C.S. Lau, Y. Fan, Q. Chen, M. Tweedie, X. Wang, Y. Zhou, J.H. Warner, Lateral graphene-contacted vertically stacked WS₂/MoS₂ hybrid photodetectors with large gain, Adv Mater 29 (2017): 1702917, <https://doi.org/10.1002/adma.201702917>.
- [159] T.-H. Tsai, Z.-Y. Liang, Y.-C. Lin, C.-C. Wang, K.-L. Lin, K. Suenaga, P.-W. Chiu, Photogating WS₂ photodetectors using embedded WSe₂ charge puddles, ACS Nano 14 (2020) 4559–4566, <https://doi.org/10.1021/acsnano.0c00098>.
- [160] D. Kufer, G. Konstantatos, Photo-FETs: phototransistors enabled by 2D and 0D nanomaterials, ACS Photonics 3 (2016) 2197–2210, <https://doi.org/10.1021/acspophotonics.6b00391>.
- [161] N. Guo, L. Xiao, F. Gong, M. Luo, F. Wang, Y. Jia, H. Chang, J. Liu, Q. Li, Y. Wu, Y. Wang, C. Shan, Y. Xu, P. Zhou, W. Hu, Light-driven WSe₂-ZnO junction field-effect transistors for high-performance photodetection, Adv Sci 7 (2020): 1901637, <https://doi.org/10.1002/advs.201901637>.
- [162] P. Lopez-Varo, L. Bertoluzzi, J. Bisquert, M. Alexe, M. Coll, J. Huang, J.A. Jimenez-Tejada, T. Kirchartz, R. Nechache, F. Rosei, Y. Yuan, Physical aspects of ferroelectric semiconductors for photovoltaic solar energy conversion, Phys Rep 653 (2016) 1–40, <https://doi.org/10.1016/j.physrep.2016.07.006>.

- [163] J. Wang, H. Fang, X. Wang, X. Chen, W. Lu, W. Hu, Recent progress on localized field enhanced two-dimensional material photodetectors from ultraviolet-visible to infrared, *Small* 13 (2017): 1700894, <https://doi.org/10.1002/smll.201700894>.
- [164] Y. Bai, H. Jantunen, J. Jutti, Ferroelectric oxides for solar energy conversion, multi-source energy harvesting/sensing, and opto-ferroelectric applications, *ChemSusChem* 12 (2019) 2540–2549, <https://doi.org/10.1002/csc.201900671>.
- [165] D. Sando, Y. Yang, C. Paillard, B. Dkhil, L. Bellaiche, V. Nagarajan, Epitaxial ferroelectric oxide thin films for optical applications, *Appl Phys Rev* 5 (2018): 041108, <https://doi.org/10.1063/1.5046559>.
- [166] L. Li, Y. Zhang, R. Wang, J. Sun, Y. Si, H. Wang, C. Pan, Y. Dai, Ferroelectricity-induced performance enhancement of V-doped ZnO/Si photodetector by direct energy band modulation, *Nano Energy* 65 (2019): 104046, <https://doi.org/10.1016/j.nanoen.2019.104046>.
- [167] S. Yan, Z. Zheng, S. Rai, M.A. Retana, M. Bhatt, L. Malkinski, W. Zhou, Coupling effect of magnetic fields on piezotronic and piezophototronic properties of ZnO and ZnO/Co₃O₄ core/shell nanowire arrays, *ACS Appl Nano Mater* 1 (2018) 6897–6903, <https://doi.org/10.1021/acsnano.8b01707>.
- [168] J. Liu, S.T. Pantelides, Mechanisms of pyroelectricity in three- and two-dimensional materials, *Phys Rev Lett* 120 (2018) 207602, <https://doi.org/10.1103/PhysRevLett.120.207602>.
- [169] Z.L.Z. Wang, R. Yu, C. Pan, Z. Li, J. Yang, F. Yi, Z.L.Z. Wang, Light-induced pyroelectric effect as an effective approach for ultrafast ultraviolet nanosensing, *Nat Commun* 6 (2015), <https://doi.org/10.1038/ncomms9401>.
- [170] W. Peng, X. Wang, R. Yu, Y. Dai, H. Zou, A.C. Wang, Y. He, Z.L. Wang, Enhanced performance of a self-powered organic/inorganic photodetector by pyro-phototronic and piezo-phototronic effects, *Adv Mater* 29 (2017): 1606698, <https://doi.org/10.1002/adma.201606698>.
- [171] Y. Feng, Y. Zhang, Y. Wang, Z. Wang, Frequency response characteristics of pyroelectric effect in p-n junction UV detectors, *Nano Energy* 54 (2018) 429–436, <https://doi.org/10.1016/j.nanoen.2018.10.022>.
- [172] D. You, C. Xu, W. Zhang, J. Zhao, F. Qin, Z. Shi, Photovoltaic-pyroelectric effect coupled broadband photodetector in self-powered ZnO/ZnTe core/shell nanorod arrays, *Nano Energy* 62 (2019) 310–318, <https://doi.org/10.1016/j.nanoen.2019.05.050>.
- [173] Y. Zhang, M. Hu, Z. Wang, Enhanced performances of p-Si/n-ZnO self-powered photodetector by interface state modification and pyro-phototronic effect, *Nano Energy* 71 (2020): 104630, <https://doi.org/10.1016/j.nanoen.2020.104630>.
- [174] K. Zhang, Z.L. Wang, Y. Yang, Enhanced P3HT/ZnO nanowire array solar cells by pyro-phototronic effect, *ACS Nano* 10 (2016) 10331–10338, <https://doi.org/10.1021/acsnano.6b06049>.
- [175] Z.L.Z. Wang, R. Yu, X. Wang, W. Wu, Z.L.Z. Wang, Ultrafast response p-Si/n-ZnO heterojunction ultraviolet detector based on pyro-phototronic effect, *Adv Mater* 28 (2016) 6880–6886, <https://doi.org/10.1002/adma.201600884>.
- [176] B. Ouyang, K. Zhang, Y. Yang, Photocurrent polarity controlled by light wavelength in self-powered ZnO nanowires/SnS photodetector system, *iScience* 1 (2018) 16–23, <https://doi.org/10.1016/j.isci.2018.01.002>.
- [177] J. Dong, Z. Wang, X. Wang, Z.L. Wang, Temperature dependence of the pyro-phototronic effect in self-powered p-Si/n-ZnO nanowires heterojuncted ultraviolet sensors, *Nano Today* 29 (2019) 100798, <https://doi.org/10.1016/j.nantod.2019.100798>.
- [178] Y. Chang, J. Wang, F. Wu, W. Tian, W. Zhai, Structural design and pyroelectric property of SnS/CdS heterojunctions contrived for low-temperature visible photodetectors, *Adv Funct Mater* (2020): 2001450, <https://doi.org/10.1002/adfm.202001450>.
- [179] K. Zhang, Y. Yang, Thermo-phototronic effect enhanced InP/ZnO nanorod heterojunction solar cells for self-powered wearable electronics, *Adv Funct Mater* 27 (2017): 1703331, <https://doi.org/10.1002/adfm.201703331>.
- [180] J. Chen, Q. Ma, X.-J. Wu, L. Li, J. Liu, H. Zhang, Wet-chemical synthesis and applications of semiconductor nanomaterial-based epitaxial heterostructures, *Nano-Micro Lett* 11 (2019) 86, <https://doi.org/10.1007/s40820-019-0317-6>.
- [181] X. Wang, H. Zhu, Y. Xu, H. Wang, Y. Tao, S. Hark, X. Xiao, Q. Li, Aligned ZnO/CdTe core-shell nanocable arrays on indium tin oxide: synthesis and photoelectrochemical properties, *ACS Nano* 4 (2010) 3302–3308, <https://doi.org/10.1021/nn1001547>.
- [182] Z. Bai, X. Yan, Y. Li, Z. Kang, S. Cao, Y. Zhang, 3D-Branched ZnO/CdS nanowire arrays for solar water splitting and the service safety research, *Adv Energy Mater* 6 (2016), <https://doi.org/10.1002/aenm.201501459>.
- [183] J. Xu, Z. Chen, J.A. Zapien, C.-S. Lee, W. Zhang, Surface engineering of ZnO nanostructures for semiconductor-sensitized solar cells, *Adv Mater* 26 (2014) 5337–5367, <https://doi.org/10.1002/adma.201400403>.
- [184] Y. Myung, D.M. Jang, T.K. Sung, Y.J. Sohn, G.B. Jung, Y.J. Cho, H.S. Kim, J. Park, Composition-tuned ZnO–CdSSe Core–Shell nanowire arrays, *ACS Nano* 4 (2010) 3789–3800, <https://doi.org/10.1021/nn100684q>.
- [185] Z. Li, J. Nieto-Pescador, A.J. Carson, J.C. Blake, L. Gundlach, Efficient Z-scheme charge separation in novel vertically aligned ZnO/CdSSe nanotrees, *Nano-technology* 27 (2016): 135401, <https://doi.org/10.1088/0957-4484/27/13/135401>.
- [186] Y. Myung, J.H. Kang, J.W. Choi, D.M. Jang, J. Park, Polytypic ZnCdSe shell layer on a ZnO nanowire array for enhanced solar cell efficiency, *J Mater Chem* 22 (2012) 2157–2165, <https://doi.org/10.1039/c1jm15003k>.
- [187] W.A. Bhutto, Z. Wu, Y. Cao, W. Wang, J. He, Q. Luo, S. Li, H. Li, J. Kang, Beneficial effect of alloy disorder on the conversion efficiency of ZnO/ZnxCd1-xSe coaxial nanowire solar cells, *J Mater Chem A* 3 (2015) 6360–6365, <https://doi.org/10.1039/c5ta00800j>.
- [188] Z. Wang, X. Zhan, Y. Wang, M. Safdar, M. Niu, J. Zhang, Y. Huang, J. He, ZnO/ZnS_xSe_{1-x} core/shell nanowire arrays as photoelectrodes with efficient visible light absorption, *Appl Phys Lett* 101 (2012): 073105, <https://doi.org/10.1063/1.4745918>.
- [189] Z. Wang, H. Yin, C. Jiang, M. Safdar, J. He, ZnO/ZnS_xSe_{1-x}/ZnSe double-shelled coaxial heterostructure: enhanced photoelectrochemical performance and its optical properties study, *Appl Phys Lett* 101 (2012) 253109, <https://doi.org/10.1063/1.4772943>.
- [190] X. Zhan, Y. Bao, F. Wang, Q. Wang, Z. Cheng, Z. Wang, K. Xu, Z. Fang, J. He, Surface plasmon resonance enhanced light absorption of Au decorated composition-tuned ZnO/Zn_xCd_{1-x}Se_xTe_{1-y} core/shell nanowires for efficient H₂ production, *Appl Phys Lett* 106 (2015): 123904, <https://doi.org/10.1063/1.4916397>.
- [191] H. Li, X. Wang, X. Zhu, X. Duan, A. Pan, Composition modulation in one-dimensional and two-dimensional chalcogenide semiconductor nanostructures, *Chem Soc Rev* 47 (2018) 7504–7521, <https://doi.org/10.1039/C8CS00418H>.
- [192] P. Guo, J. Xu, K. Gong, X. Shen, Y. Lu, Y. Qiu, J. Xu, Z. Zou, C. Wang, H. Yan, Y. Luo, A. Pan, H. Zhang, J.C. Ho, K.M. Yu, On-nanowire axial heterojunction design for high-performance photodetectors, *ACS Nano* 10 (2016) 8474–8481, <https://doi.org/10.1021/acsnano.6b03458>.
- [193] Q. Zhang, H.H. Liu, P. Guo, D. Li, P. Fan, W. Zheng, X. Zhu, Y. Jiang, H. Zhou, W. Hu, X. Zhuang, H.H. Liu, X. Duan, A. Pan, Vapor growth and interfacial carrier dynamics of high-quality CdS-CdSSe-CdS axial nanowire heterostructures, *Nano Energy* 32 (2017) 28–35, <https://doi.org/10.1016/j.nanoen.2016.12.014>.
- [194] Y. Sun, T. Dong, L. Yu, J. Xu, K. Chen, Planar growth, integration, and applications of semiconducting nanowires, *Adv Mater* (2019): 1903945, <https://doi.org/10.1002/adma.201903945>.
- [195] Y. Huang, Directed assembly of one-dimensional nanostructures into functional networks, *Science* 291 (80) (2001) 630–633, <https://doi.org/10.1126/science.291.5504.630>.
- [196] D. Whang, S. Jin, Y. Wu, C.M. Lieber, Large-scale hierarchical organization of nanowire arrays for integrated nanosystems, *Nano Lett* 3 (2003) 1255–1259, <https://doi.org/10.1021/nl0345062>.
- [197] X. Liu, L. Jiang, X. Zou, X. Xiao, S. Guo, C. Jiang, X. Liu, Z. Fan, W. Hu, X. Chen, W. Lu, W. Hu, L. Liao, Scalable integration of indium zinc oxide/photosensitive-nanowire composite thin-film transistors for transparent multicolor photodetectors array, *Adv Mater* 26 (2014) 2919–2924, <https://doi.org/10.1002/adma.201305073>.
- [198] D. Tsivion, M. Schwartzman, R. Popovitz-Biro, P. von Huth, E. Joselevich, Guided growth of millimeter-long horizontal nanowires with controlled orientations, *Science* 333 (80) (2011) 1003–1007, <https://doi.org/10.1126/science.1208455>.
- [199] E. Oksenberg, S. Martí-Sánchez, R. Popovitz-Biro, J. Arbiol, E. Joselevich, Surface-guided core–shell ZnSe@ZnTe nanowires as radial p–n heterojunctions with photovoltaic behavior, *ACS Nano* 11 (2017) 6155–6166, <https://doi.org/10.1021/acsnano.7b02199>.
- [200] J. Xu, K. Rechav, R. Popovitz-Biro, I. Nevo, Y. Feldman, E. Joselevich, High-gain 200 ns photodetectors from self-aligned CdS-CdSe core–shell nanowalls, *Adv Mater* 30 (2018): 1800413, <https://doi.org/10.1002/adma.201800413>.
- [201] R.D. Dupuis, Metalorganic chemical vapor deposition of III-V semiconductors, *Science* 226 (80) (1984) 623–629, <https://doi.org/10.1126/science.226.4675.623>.
- [202] D.H. Lee, Y. Sim, J. Wang, S.Y. Kwon, Metal-organic chemical vapor deposition of 2D van der Waals materials - the challenges and the extensive future opportunities, *Apl Mater* 8 (2020): 030901, <https://doi.org/10.1063/1.5142601>.
- [203] Y.J. Hsu, S.Y. Lu, One-step preparation of coaxial CdS-ZnS nanowires, *Chem Commun* 10 (2004) 2102–2103, <https://doi.org/10.1039/b403932g>.
- [204] Y.-J. Hsu, S.-Y. Lu, Y.-F. Lin, One-step preparation of coaxial CdS-ZnS and Cd_{1-x}Zn_x-ZnS nanowires, *Adv Funct Mater* 15 (2005) 1350–1357, <https://doi.org/10.1002/adfm.200400563>.
- [205] Z. Liu, C.X. Shan, S.K. Hark, L.P. You, J. Chen, Side-by-side ZnSe/ZnCdSe bicrystalline nanoribbons prepared by a two-step process, *J Phys Chem C* 111 (2007) 16181–16183, <https://doi.org/10.1021/jp074789c>.
- [206] P. Chgamgar, F. Rigoni, S. You, I. Dobryden, M.G. Kohan, A.L. Pellegrino, I. Concina, N. Almqvist, G. Malandrino, A. Vomiero, ZnO–Cu₂O core–shell nanowires as stable and fast response photodetectors, *Nano Energy* 51 (2018) 308–316, <https://doi.org/10.1016/j.nanoen.2018.06.058>.
- [207] M.A. Hassan, A. Waseem, M.A. Johar, I.V. Bagal, J.-S. Ha, S.-W. Ryu, Single-step fabrication of 3D hierarchical ZnO/ZnS heterojunction branched nanowires by MOCVD for enhanced photoelectrochemical water splitting, *J Mater Chem* (2020), <https://doi.org/10.1039/c9ta13714a>.
- [208] G. Amiri, A. Souissi, N. Hanèche, C. Vilar, A. Lusson, V. Sallet, P. Galtier, Synthesis and characterization of core–shell ZnO/ZnSe nanowires grown by MOCVD, *Phys Status Solidi* 250 (2013), <https://doi.org/10.1002/pssb.201300011> n/a–n/a.
- [209] J.N. Olding, A. Henning, J.T. Dong, Q. Zhou, M.J. Moody, P.J.M. Smeets, P. Darancet, E.A. Weiss, L.J. Lauhon, Charge separation in epitaxial SnS/MoS₂

- vertical heterojunctions grown by low-temperature pulsed MOCVD, *ACS Appl Mater Interfaces* 11 (2019) 40543–40550, <https://doi.org/10.1021/acsmami.9b14412>.
- [210] S. Irvine, P. Capper (Eds.), *Metalorganic Vapor Phase Epitaxy (MOVPE)*, Wiley, 2019, <https://doi.org/10.1002/9781119313021>.
- [211] H. Kim, D. Ovchinnikov, D. Deiana, D. Unuchek, A. Kis, Suppressing nucleation in metal-organic chemical vapor deposition of MoS₂ monolayers by alkali metal halides, *Nano Lett* 17 (2017) 5056–5063, <https://doi.org/10.1021/acs.nanolett.7b02311>.
- [212] A. Devi, 'Old Chemistries' for new applications: perspectives for development of precursors for MOCVD and ALD applications, *Coord Chem Rev* 257 (2013) 3332–3384, <https://doi.org/10.1016/j.ccr.2013.07.025>.
- [213] R.L. Puurunen, A short history of atomic layer deposition: tuomo suntola's atomic layer epitaxy, *Chem Vap Depos* 20 (2014) 332–344, <https://doi.org/10.1002/cvde.201402012>.
- [214] A.A. Malygin, V.E. Drozd, A.A. Malkov, V.M. Smirnov, From V. B. Aleskovskii's "framework" hypothesis to the method of molecular layering/atomic layer Deposition, *Chem Vap Depos* 21 (2015) 216–240, <https://doi.org/10.1002/cvde.201502013>.
- [215] M. Leskelä, M. Mattinen, M. Ritala, Review Article: atomic layer deposition of optoelectronic materials, *J Vac Sci Technol B* 37 (2019): 030801, <https://doi.org/10.1116/1.5083692>.
- [216] S.M. George, Atomic layer deposition: an overview, *Chem Rev* 110 (2010) 111–131, <https://doi.org/10.1021/cr900056b>.
- [217] M. Leskelä, M. Ritala, Atomic layer deposition chemistry: recent developments and future challenges, *Angew Chem Int Ed* 42 (2003) 5548–5554, <https://doi.org/10.1002/anie.200301652>.
- [218] A. Al-Haddad, Z. Wang, M. Zhou, S. Tarish, R. Vellacheri, Y. Lei, Constructing well-ordered CdTe/TiO₂ core/shell nanowire arrays for solar energy conversion, *Small* 12 (2016) 5538–5542, <https://doi.org/10.1002/smll.201601412>.
- [219] R. Zazpe, M. Knaut, H. Sophia, L. Hromadko, M. Albert, J. Prikryl, V. Gärtnерová, J.W. Bartha, J.M. Macak, Atomic layer deposition for coating of high aspect ratio TiO₂ nanotube layers, *Langmuir* 32 (2016) 10551–10558, <https://doi.org/10.1021/acs.langmuir.6b03119>.
- [220] S. Ng, M. Krbal, R. Zazpe, J. Prikryl, J. Charvot, F. Dvorák, L. Strizik, S. Slang, H. Sophia, Y. Kosto, V. Matolin, F.K. Yam, F. Bures, J.M. Macak, MoSe_xO_y-coated 1D TiO₂ nanotube layers: efficient interface for light-driven applications, *Adv Mater Interfaces* 5 (2018): 1701146, <https://doi.org/10.1002/admi.201701146>.
- [221] R. Zazpe, H. Sophia, J. Prikryl, M. Krbal, J. Mistrik, F. Dvorak, L. Hromadko, J.M. Macak, A 1D conical nanotubular TiO₂/CdS heterostructure with superior photon-to-electron conversion, *Nanoscale* 10 (2018) 16601–16612, <https://doi.org/10.1039/c8nr02418a>.
- [222] M. Krbal, J. Prikryl, R. Zazpe, H. Sophia, J.M. Macak, CdS-coated TiO₂ nanotube layers: downscaling tube diameter towards efficient heterostructured photoelectrochemical conversion, *Nanoscale* 9 (2017) 7755–7759, <https://doi.org/10.1039/c7nr02841e>.
- [223] S.K. Karuturi, J. Luo, C. Cheng, L. Liu, L.T. Su, A.I.Y. Tok, H.J. Fan, A novel photoanode with three-dimensionally, hierarchically ordered nanobushes for highly efficient photoelectrochemical cells, *Adv Mater* 24 (2012) 4157–4162, <https://doi.org/10.1002/adma.201104428>.
- [224] Z. Wang, X. Li, H. Ling, C.K. Tan, L.P. Yeo, A.C. Grimsdale, A.I.Y. Tok, 3D FTO/FTO-Nanocrystal/TiO₂ composite inverse opal photoanode for efficient photoelectrochemical water splitting, *Small* 14 (2018): 1800395, <https://doi.org/10.1002/smll.201800395>.
- [225] P. Labouchere, A.K. Chandiran, T. Moehl, H. Harms, S. Chavhan, R. Tena-Zaera, M.K. Nazeeruddin, M. Graetzel, N. Tetreault, Passivation of ZnO nanowire guests and 3D inverse opal host photoanodes for dye-sensitized solar cells, *Adv Energy Mater* 4 (2014): 1400217, <https://doi.org/10.1002/aejm.201400217>.
- [226] Z. Wang, N. Brodusch, R. Gauvin, G.P. Demopoulos, Nanoengineering of the Cu₂ZnSnS₄/TiO₂ interface: via atomic layer deposition of Al₂O₃ for high sensitivity photodetectors and solid state solar cells, *J Mater Chem A* 6 (2018) 11507–11520, <https://doi.org/10.1039/c8ta02966k>.
- [227] G. Yan, C. Zeng, Y. Yuan, G. Wang, G. Cen, L. Zeng, L. Zhang, Y. Fu, C. Zhao, R. Hong, W. Mai, Significantly enhancing response speed of self-powered Cu₂ZnSn(S,Se)₄ thin film photodetectors by atomic layer deposition of simultaneous electron blocking and electrode protective Al₂O₃ layers, *ACS Appl Mater Interfaces* 11 (2019) 32097–32107, <https://doi.org/10.1021/acsmami.9b08405>.
- [228] K. Park, Q. Zhang, B.B. Garcia, X. Zhou, Y.-H. Jeong, G. Cao, Effect of an ultrathin TiO₂ layer coated on submicrometer-sized ZnO nanocrystallite aggregates by atomic layer deposition on the performance of dye-sensitized solar cells, *Adv Mater* 22 (2010) 2329–2332, <https://doi.org/10.1002/adma.200903219>.
- [229] N. Tétreault, É. Arseneault, L.P. Heiniger, N. Soheilnia, J. Brillet, T. Moehl, S. Zakeeruddin, G.A. Ozin, M. Grätzel, High-efficiency dye-sensitized solar cell with three-dimensional photoanode, *Nano Lett* 11 (2011) 4579–4584, <https://doi.org/10.1021/nl201792r>.
- [230] G. Cen, Y. Liu, C. Zhao, G. Wang, Y. Fu, G. Yan, Y. Yuan, C. Su, Z. Zhao, W. Mai, Atomic-layer deposition-assisted double-side interfacial engineering for high-performance flexible and stable CsPbBr₃ perovskite photodetectors toward visible light communication applications, *Small* 15 (2019) 1902135, <https://doi.org/10.1002/smll.201902135>.
- [231] Z. Li, X. Liang, G. Li, H. Liu, H. Zhang, J. Guo, J. Chen, K. Shen, X. San, W. Yu, R.E.I. Schropp, Y. Mai, 9.2%-efficient core-shell structured antimony selenide nanorod array solar cells, *Nat Commun* 10 (2019) 1–9, <https://doi.org/10.1038/s41467-018-07903-6>.
- [232] P. Büttner, F. Scheler, C. Pointer, D. Döhler, M.K.S. Barr, A. Koroleva, D. Pankin, R. Hatada, S. Flege, A. Manshina, E.R. Young, I. Minguez-Bacho, J. Bachmann, Adjusting interfacial chemistry and electronic properties of photovoltaics based on a highly pure Sb₂S₃ absorber by atomic layer deposition, *ACS Appl Energy Mater* 2 (2019) 8747–8756, <https://doi.org/10.1021/acsami.9b01721>.
- [233] J.R. Bakke, K.L. Pickrahn, T.P. Brennan, S.F. Bent, Nanoengineering and interfacial engineering of photovoltaics by atomic layer deposition, *Nanoscale* 3 (2011) 3482, <https://doi.org/10.1039/c1nr10349k>.
- [234] L. Wen, M. Zhou, C. Wang, Y. Mi, Y. Lei, Nanoengineering energy conversion and storage devices via atomic layer deposition, *Adv Energy Mater* 6 (2016): 1600468, <https://doi.org/10.1002/aenm.201600468>.
- [235] S.M. Rossnagel, Thin film deposition with physical vapor deposition and related technologies, *J Vac Sci Technol A Vacuum, Surfaces, Film* 21 (2003) S74–S87, <https://doi.org/10.1116/1.1600450>.
- [236] J. Chen, K. Wang, R. Huang, T. Saito, Y.H. Ikuhara, T. Hirayama, W. Zhou, Facile route to polycrystalline Pd/SnO₂ nanowires using ZnO-nanowire templates for gas-sensing applications, *IEEE Trans Nanotechnol* 9 (2010) 634–639, <https://doi.org/10.1109/TNANO.2010.2052629>.
- [237] J. Chen, K. Wang, W. Zhou, Vertically aligned ZnO nanorod arrays coated with SnO₂/nmetal nanoparticle for highly sensitive and selective gas detection, *IEEE Trans Nanotechnol* 10 (2011) 968–974, <https://doi.org/10.1109/TNANO.2010.2091423>.
- [238] Y. Liu, Y. Huang, X. Duan, Van der Waals integration before and beyond two-dimensional materials, *Nature* 567 (2019) 323–333, <https://doi.org/10.1038/s41586-019-1013-x>.
- [239] R. Tang, Z.H. Zheng, Z.H. Su, X.J. Li, Y.D. Wei, X.H. Zhang, Y.Q. Fu, J.T. Luo, P. Fan, G.X. Liang, Highly efficient and stable planar heterojunction solar cell based on sputtered and post-selenized Sb₂Se₃ thin film, *Nano Energy* 64 (2019): 103929, <https://doi.org/10.1016/j.nanoen.2019.103929>.
- [240] C. Terashima, R. Hishinuma, N. Roy, Y. Sugiyama, S.S. Latthe, K. Nakata, T. Kondo, M. Yuasa, A. Fujishima, Charge separation in TiO₂/BDD heterojunction thin film for enhanced photoelectrochemical performance, *ACS Appl Mater Interfaces* 8 (2016) 1583–1588, <https://doi.org/10.1021/acsmami.5b010993>.
- [241] L. Cai, W. Wang, L. Jin, Z. Yao, W. Lin, L. Meng, B. Ai, Z. Liang, Y. Huang, F. Zhang, P.P. Altermatt, H. Shen, 12.2% low temperature-processed dopant-free CdS/p-Si heterojunction solar cells, *Adv Mater Interfaces* 6 (2019): 1900367, <https://doi.org/10.1002/admi.201900367>.
- [242] K. Zhang, M. Peng, W. Wu, J. Guo, G. Gao, Y. Liu, J. Kou, R. Wen, Y. Lei, A. Yu, Y. Zhang, J. Zhai, Z.L. Wang, A flexible p-CuO/n-MoS₂ heterojunction photodetector with enhanced photoresponse by the piezo-photoconductive effect, *Mater Horizons* 4 (2017) 274–280, <https://doi.org/10.1039/c6mh00568c>.
- [243] L. Guo, Z. Yang, K. Marcus, Z. Li, B. Luo, L. Zhou, X. Wang, Y. Du, Y. Yang, MoS₂/TiO₂ heterostructures as nonmetal plasmonic photocatalysts for highly efficient hydrogen evolution, *Energy Environ Sci* 11 (2018) 106–114, <https://doi.org/10.1039/C7EE02464A>.
- [244] P.R. Willmott, J.R. Huber, Pulsed laser vaporization and deposition, *Rev Mod Phys* 72 (2000) 315–328, <https://doi.org/10.1103/RevModPhys.72.315>.
- [245] Y.-L. Huang, H.-J. Liu, C.-H. Ma, P. Yu, Y.-H. Chu, J.-C. Yang, Pulsed laser deposition of complex oxide heteroepitaxy, *Chin J Phys* 60 (2019) 481–501, <https://doi.org/10.1016/j.cjph.2019.05.030>.
- [246] I. Ka, B. Gonfa, V. Le Borgne, D. Ma, M.A. El Khakani, Pulsed laser ablation based synthesis of Pb₃S-quantum dots-decorated one-dimensional nanostructures and their direct integration into highly efficient nanohybrid heterojunction-based solar cells, *Adv Funct Mater* 24 (2014) 4042–4050, <https://doi.org/10.1002/adfm.201304191>.
- [247] M.S. Gudiksen, L.J. Lauhon, J. Wang, D.C. Smith, C.M. Lieber, Growth of nanowire superlattice structures for nanoscale photonics and electronics, *Nature* 415 (2002) 617–620, <https://doi.org/10.1038/415617a>.
- [248] Y. Wu, R. Fan, P. Yang, Block-by-Block growth of single-crystalline Si/SiGe superlattice nanowires, *Nano Lett* 2 (2002) 83–86, <https://doi.org/10.1021/nl0156888>.
- [249] O. Hayden, A.B. Greytak, D.C. Bell, Core-shell nanowire light-emitting diodes, *Adv Mater* 17 (2005) 701–704, <https://doi.org/10.1002/adma.200401235>.
- [250] D. Zhang, Z. Liu, S. Han, C. Li, B. Lei, M.P. Stewart, J.M. Tour, C. Zhou, Magnetite (Fe₃O₄) core-shell nanowires: synthesis and magnetoresistance, *Nano Lett* 4 (2004) 2151–2155, <https://doi.org/10.1021/nl048758u>.
- [251] Z. Liu, D. Zhang, S. Han, C. Li, B. Lei, W. Lu, J. Fang, C. Zhou, Single crystalline magnetite nanotubes, *J Am Chem Soc* 127 (2005) 6–7, <https://doi.org/10.1021/ja0445239>.
- [252] S. Han, C. Li, Z. Liu, B. Lei, D. Zhang, W. Jin, X. Liu, T. Tang, C. Zhou, Transition metal oxide core-shell nanowires: generic synthesis and transport studies, *Nano Lett* 4 (2004) 1241–1246, <https://doi.org/10.1021/nl0494670>.
- [253] K. Wang, J.J. Chen, Z.M. Zeng, J. Tarr, W.L. Zhou, Y. Zhang, Y.F. Yan, C.S. Jiang, J. Pern, A. Mascarenhas, Synthesis and photovoltaic effect of vertically aligned ZnO/ZnS core/shell nanowire arrays, *Appl Phys Lett* 96 (2010): 123105, <https://doi.org/10.1063/1.3367706>.
- [254] S.C. Rai, K. Wang, J. Chen, J.K. Marmon, M. Bhatt, S. Wozny, Y. Zhang, W. Zhou, Enhanced broad band photodetection through piezo-photoconductive

- effect in CdSe/ZnTe core/shell nanowire array, *Adv Electron Mater* 1 (2015): 1400050, <https://doi.org/10.1002/aelm.201400050>.
- [255] S. Yan, S.C. Rai, Z. Zheng, F. Alqarni, M. Bhatt, M.A. Retana, W. Zhou, Piezophototronic effect enhanced UV/visible photodetector based on ZnO/ZnSe heterostructure core/shell nanowire array and its self-powered performance, *Adv Electron Mater* 2 (2016): 1600242, <https://doi.org/10.1002/aelm.201600242>.
- [256] Q. Yang, Y. Li, Z. Hu, Z. Duan, P. Liang, J. Sun, N. Xu, J. Wu, Extended photo-response of ZnO/CdS core/shell nanorods fabricated by hydrothermal reaction and pulsed laser deposition, *Optic Express* 22 (2014) 8617, <https://doi.org/10.1364/oe.22.008617>.
- [257] X. Yang, Q. Yang, Z. Hu, W. Zhang, H. Li, L. Li, Y. Qiu, N. Xu, J. Wu, J. Sun, Multi-band luminescent ZnO/ZnSe core/shell nanorods and their temperature-dependent photoluminescence, *RSC Adv* 6 (2016) 98413–98421, <https://doi.org/10.1039/c6ra21186k>.
- [258] Z. Lu, Y. Xu, Y. Yu, K. Xu, J. Mao, G. Xu, Y. Ma, D. Wu, J. Jie, Ultrahigh speed and broadband few-layer MoTe₂/Si 2D–3D heterojunction-based photodiodes fabricated by pulsed laser deposition, *Adv Funct Mater* 30 (2020): 1907951, <https://doi.org/10.1002/adfm.201907951>.
- [259] J. Liu, J. Zhang, Nanointerface chemistry: lattice-mismatch-directed synthesis and application of hybrid nanocrystals, *Chem Rev* 120 (2020) 2123–2170, <https://doi.org/10.1021/acs.chemrev.9b00443>.
- [260] G.D. Moon, S. Ko, Y. Min, J. Zeng, Y. Xia, U. Jeong, Chemical transformations of nanostructured materials, *Nano Today* 6 (2011) 186–203.
- [261] J.L. Fenton, B.C. Steimle, R.E. Schaak, Tunable intraparticle frameworks for creating complex heterostructured nanoparticle libraries, *Science* 360 (80) (2018) 513–517, <https://doi.org/10.1126/science.aar5597>.
- [262] X. Li, M. Ji, H. Li, H. Wang, M. Xu, H. Rong, J. Wei, J. Liu, J. Liu, W. Chen, C. Zhu, J. Wang, J. Zhang, Cation/anion exchange reactions toward the syntheses of upgraded nanostructures: principles and applications, *Matter* 2 (2020) 554–586, <https://doi.org/10.1016/j.matt.2019.12.024>.
- [263] B.C. Steimle, J.L. Fenton, R.E. Schaak, Rational construction of a scalable heterostructured nanorod megalibrary, *Science* 367 (80) (2020) 418–424, <https://doi.org/10.1126/science.aaz1172>.
- [264] D.C. Reynolds, G. Leies, L.L. Antes, R.E. Marburger, Photovoltaic effect in cadmium sulfide, *Phys Rev* 96 (1954) 533–534, <https://doi.org/10.1103/PhysRev.96.533>.
- [265] J.B. Rivest, S.L. Swisher, L.K. Fong, H. Zheng, A. Paul Alivisatos, Assembled monolayer nanorod heterojunctions, *ACS Nano* 5 (2011) 3811–3816, <https://doi.org/10.1021/nn2001454>.
- [266] J. Tang, Z. Huo, S. Britzman, H. Gao, P. Yang, Solution-processed core–shell nanowires for efficient photovoltaic cells, *Nat Nanotechnol* 6 (2011) 568–572, <https://doi.org/10.1038/nnano.2011.139>.
- [267] A.B. Wong, S. Britzman, Y. Yu, N.P. Dasgupta, P. Yang, Core–shell CdS–Cu₂S nanorod array solar cells, *Nano Lett* 15 (2015) 4096–4101, <https://doi.org/10.1021/acs.nanolett.5b01203>.
- [268] Z. Xiong, Y. Cai, X. Ren, B. Cao, J. Liu, Z. Huo, J. Tang, Solution-processed CdS/Cu₂S superlattice nanowire with enhanced thermoelectric property, *ACS Appl Mater Interfaces* 9 (2017) 32424–32429, <https://doi.org/10.1021/acsami.7b09346>.
- [269] S. Dogan, S. Kudera, Z. Dang, F. Palazon, U. Petralanda, S. Artyukhin, L. De Trizio, L. Manna, R. Krahne, Lateral epitaxial heterojunctions in single nanowires fabricated by masked cation exchange, *Nat Commun* 9 (2018) 1–8, <https://doi.org/10.1038/s41467-018-02878-w>.
- [270] I. Kriegel, A. Wisnet, A.R. Srimath Kandala, F. Scotognella, F. Tassone, C. Scheu, H. Zhang, A.O. Govorov, J. Rodríguez-Fernández, J. Feldmann, Cation exchange synthesis and optoelectronic properties of type II CdTe–Cu_{2-x}Te nano-heterostructures, *J Mater Chem C* 2 (2014) 3189–3198, <https://doi.org/10.1039/c3tc32049a>.
- [271] B. Zhang, Y. Jung, H.-S. Chung, L. Van Vugt, R. Agarwal, Nanowire transformation by size-dependent cation exchange reactions, *Nano Lett* 10 (2010) 149–155, <https://doi.org/10.1021/nl903059c>.
- [272] J.Y. Lee, D.S. Kim, J. Park, Chemical conversion reaction between CdS nanobelts and ZnS nanobelts by vapor transport, *Chem Mater* 19 (2007) 4663–4669, <https://doi.org/10.1021/cm070814f>.
- [273] W. Il Park, H.S. Kim, S.Y. Jang, J. Park, S.Y. Bae, M. Jung, H. Lee, J. Kim, Transformation of ZnTe nanowires to CdTe nanowires through the formation of ZnCdTe–CdTe core–shell structure by vapor transport, *J Mater Chem* 18 (2008) 875, <https://doi.org/10.1039/b717966a>.
- [274] B.D. Anderson, J.B. Tracy, Nanoparticle conversion chemistry: kirkendall effect, galvanic exchange, and anion exchange, *Nanoscale* 6 (2014) 12195–12216, <https://doi.org/10.1039/C4NR02025A>.
- [275] S. Gupta, S.V. Kershaw, A.L. Rogach, 25th anniversary article: ion exchange in colloidal nanocrystals, *Adv Mater* 25 (2013) 6923–6944, <https://doi.org/10.1002/adma.201302400>.
- [276] R. Agarwal, N.M. Krook, M.-L. Ren, L.Z. Tan, W. Liu, A.M. Rappe, R. Agarwal, Anion exchange in II–VI semiconducting nanostructures via atomic templating, *Nano Lett* 18 (2018) 1620–1627, <https://doi.org/10.1021/acs.nanolett.7b04424>.
- [277] S.K. Panda, A. Dev, S. Chaudhuri, Fabrication and luminescent properties of c-Axis oriented ZnO-ZnS core-shell and ZnS nanorod arrays by sulfidation of aligned ZnO nanorod arrays, *J Phys Chem C* 111 (2007) 5039–5043, <https://doi.org/10.1021/jp068391c>.
- [278] Y. Wang, M.X. Liu, T. Ling, C.C. Tang, C.Y. Zhi, X.W. Du, Gas-phase anion exchange towards ZnO/ZnSe heterostructures with intensive visible light emission, *J Mater Chem C* 2 (2014) 2793–2798, <https://doi.org/10.1039/c3tc32312a>.
- [279] J. Xu, X. Yang, H. Wang, X. Chen, C. Luan, Z. Xu, Z. Lu, V.A.L. Roy, W. Zhang, C.-S. Lee, Arrays of ZnO/Zn_xCd_{1-x}Se nanocables: band gap engineering and photovoltaic applications, *Nano Lett* 11 (2011) 4138–4143, <https://doi.org/10.1021/nl201934k>.
- [280] R. Mastria, A. Rizzo, Mastering heterostructured colloidal nanocrystal properties for light-emitting diodes and solar cells, *J Mater Chem C* 4 (2016) 6430–6446, <https://doi.org/10.1039/C6TC01334A>.
- [281] D.G. Moon, S. Rehan, D.H. Yeon, S.M. Lee, S.J. Park, S.J. Ahn, Y.S. Cho, A review on binary metal sulfide heterojunction solar cells, *Sol Energy Mater Sol Cells* 200 (2019): 109963, <https://doi.org/10.1016/j.solmat.2019.109963>.
- [282] C. Li, Q. Cao, F. Wang, Y. Xiao, Y. Li, J.J. Delaunay, H. Zhu, Engineering graphene and TMDs based van der Waals heterostructures for photovoltaic and photoelectrochemical solar energy conversion, *Chem Soc Rev* 47 (2018) 4981–5037, <https://doi.org/10.1039/c8cs0067k>.
- [283] M. Shim, Colloidal nanorod heterostructures for photovoltaics and optoelectronics, *J Phys D Appl Phys* 50 (2017): 173002, <https://doi.org/10.1088/1361-6463/aa65a5>.
- [284] F. Zhou, J. Chen, X. Tao, X. Wang, Y. Chai, 2D Materials Based Optoelectronic Memory: Convergence of Electronic Memory and Optical Sensor, *Research* 2019, 2019, p. 9490413, <https://doi.org/10.34133/2019/9490413>.
- [285] Z. Lv, Y. Wang, J. Chen, J. Wang, Y. Zhou, S.-T. Han, Semiconductor quantum dots for memories and neuromorphic computing systems, *Chem Rev* 120 (2020) 3941–4006, <https://doi.org/10.1021/acs.chemrev.9b00730>.
- [286] L. Hu, J. Yuan, Y. Ren, Y. Wang, J.-Q. Yang, Y. Zhou, Y.-J. Zeng, S.-T. Han, S. Ruan, Phosphorene/ZnO nano-heterojunctions for broadband photonic nonvolatile memory applications, *Adv Mater* 30 (2018): 1801232, <https://doi.org/10.1002/adma.201801232>.
- [287] Y. Li, S. Long, Q. Liu, H. Lv, M. Liu, Resistive switching performance improvement via modulating nanoscale conductive filament, involving the application of two-dimensional layered materials, *Small* 13 (2017): 1604306, <https://doi.org/10.1002/smll.201604306>.
- [288] Z. Wang, M. Rao, R. Midya, S. Joshi, H. Jiang, P. Lin, W. Song, S. Asapu, Y. Zhuo, C. Li, H. Wu, Q. Xia, J.J. Yang, Threshold switching of Ag or Cu in dielectrics: materials, mechanism, and applications, *Adv Funct Mater* 28 (2018): 1704862, <https://doi.org/10.1002/adfm.201704862>.
- [289] J. Wang, Z. Lv, X. Xing, X. Li, Y. Wang, M. Chen, G. Pang, F. Qian, Y. Zhou, S. Han, Optically modulated threshold switching in core–shell quantum dot based memristive device, *Adv Funct Mater* 30 (2020): 1909114, <https://doi.org/10.1002/adfm.201909114>.
- [290] J. Zhang, S. Dai, Y. Zhao, J. Zhang, J. Huang, Recent progress in photonic synapses for neuromorphic systems, *Adv Intell Syst* 2 (2020): 1900136, <https://doi.org/10.1002/aisy.201900136>.
- [291] M. Kumar, S. Abbas, J. Kim, All-oxide-based highly transparent photonic synapse for neuromorphic computing, *ACS Appl Mater Interfaces* 10 (2018) 34370–34376, <https://doi.org/10.1021/acsami.8b10870>.
- [292] S. Wang, C. Chen, Z. Yu, Y. He, X. Chen, Q. Wan, Y. Shi, D.W. Zhang, H. Zhou, X. Wang, P. Zhou, A MoS₂/PTCDA hybrid heterojunction synapse with efficient photoelectric dual modulation and versatility, *Adv Mater* 31 (2019): 1806227, <https://doi.org/10.1002/adma.201806227>.
- [293] A. Jovicic, J. Li, T. Richardson, Visible light communication: opportunities, challenges and the path to market, *IEEE Commun Mag* 51 (2013) 26–32, <https://doi.org/10.1109/MCOM.2013.6685754>.
- [294] P.H. Pathak, X. Feng, P. Hu, P. Mohapatra, Visible light communication, networking, and sensing: a survey, potential and challenges, *IEEE Commun Surv Tutorials* 17 (2015) 2047–2077, <https://doi.org/10.1109/COMST.2015.2476474>.
- [295] B. Ouyang, H. Zhao, Z.L. Wang, Y. Yang, Dual-polarity response in self-powered ZnO NWs/Sb₂Se₃ film heterojunction photodetector array for optical communication, *Nano Energy* 68 (2020): 104312, <https://doi.org/10.1016/j.nanoen.2019.104312>.